Modeling of the mechanical cutting effect on local magnetic properties of electric steels and implementation in a finite element computation code

Nabil M'Zali

École doctorale régionale Sciences Pour l'Ingénieur Lille Nord-de-France
Université de Lille : Sciences et Technologies

Modeling of the mechanical cutting effect on local magnetic properties of electric steels and implementation in a finite element computation code

Modélisation de l'effet de la découpe sur les propriétés magnétiques locales des aciers électriques et implémentation dans un code éléments finis

Thèse pour obtenir le grade de

Docteur de l'Université de Lille

Spécialité : Génie électrique

par

Nabil M'ZALI

Soutenue le 08 Juin 2021 devant le jury composé de :

Stéphane DUCHESNE	Président, Examinateur	Professeur, Université d'Artois
Juliette SOULARD	Rapporteuse	Professeur assoc., University of Warwick, (UK)
Denis NETTER	Rapporteur	Professeur, Université de Lorraine
Guillaume KREBS	Examinateur	Maître de conférence HDR, Université de Paris Sud
Abdelkader BENABOU	Directeur	Maître de conférence HDR, Université de Lille
Anouar BELAHCEN	Co-Directeur	Professeur, Aalto University, (Finlande)
Thomas HENNERON	Encadrant	Maître de conférence, Université de Lille
Floran MARTIN	Encadrant	Docteur, Aalto University, (Finlande)

Preface

This work was supported by University of Lille in France and Aalto University in Finland. It was performed between November 2017 and April 2021 at L2EP laboratory (Laboratoire d'Electotechnique et d'Electronique de Puissance), France, and Research Group of Electromechanics, School of Electrical Engineering, Finland.

Acknowledgements

I am grateful for my supervisors, Associate Professor Hab. Abdelkader BENABOU and Professor Anouar BELAHCEN and instructors Associate Professor Thomas HENNERON and Dr. Floran MARTIN for their supervision and guidance during the course of this research.

I would like to thank Stéphane DUCHESNE, Professor at University of Artois for agreeing to chair the jury and for examining my work. I would like to thank Juliette SOULARD Associate Professor at University of Warwick, Denis NETTER Professor at University of Lorraine and Guillaume KREBS Associate Professor Hab. at University of Paris Sud for taking the time to review and examine this thesis.

Big acknowledgment goes to my awesome colleagues in the L2EP laboratory in France and the Research Group of Electromechanics in Finland who created a great and rewarding working atmosphere.

I express my deepest gratitude to my parents for their support in everything, they are the greatest gift I have ever been given. This thesis is yours! Obviously, I am grateful for my sisters and brothers for their support in so many ways. I am also grateful for my in-laws parents for their support during this thesis.

I am grateful for my 'second family' in France Catherine and Benjamin FARIA for their support especially when I was preparing my Master degree in University of Lorraine. A special thanks to Marie Christine MULLER and SAIDJ Safia for their support to my wife during my long stays in Finland.

I would like to thank Professor Michel VILASI and Professor Hervé RINNART who indirectly contributed to the achievement of this thesis by giving me the opportunity to prepare the Master degree SPIM PCM at the University of Lorraine. I would also like to thank Mathieu STOFFEL Associate Professor, Brigitte VIGOLO and Alexandre DESFORGES CNRS researchers for supervision my Master internships and especially for their support and their human qualities.

Finally, I wish to thank my wife, Lamia for her support, patience and trust during these years, especially when I was in Finland where she faced the family responsibilities alone. I dedicate this thesis to my son Aris.

... Le Bus

Contents

Abstract

This thesis focuses on the effects of mechanical punching process on magnetic properties of electrical steels and on electrical machine performance. The scalar Sablik model with some improvements has been considered to account for the degraded magnetic properties. It allows to describe both magneto-elastic and magneto-plastic coupling. The identification process is carried out using measured magnetization curves under different elastic stresses and plastic strains. Since the model accounts directly for the plastic strain, a mechanical punching process simulation has been performed using the software ABAQUS.
A finite element simulation of a synchronous machine including the effect of punching process shown the degradation of the magnetic flux density at the punching edges and an increase of the iron losses by about 38%. Finally, the results obtained from the magneto-mechanical simulation have been investigated in terms of the method used to implement the plastic strain distribution in the finite element computation. Two examples have been investigated: a steel sheet and a tooth of an electrical machine. It has been shown that the degradation profile defined by the average value of the strain at each position from the edge does not reflect the real plastic strain distribution. An adjustment has been proposed.

Résumé

Cette thèse porte sur l'impact du processus de poinçonnage mécanique sur les propriétés magnétiques des matériaux qui composent les machines électriques. Le modèle anhystérétique de Sablik qui est basé sur une approche scalaire du couplage magnéto-mécanique a été considéré avec certaines modifications. Le modèle permet de décrire à la fois le couplage magnéto-élastique et magnéto-plastique. Le processus d'identification est réalisé à l'aide de courbes d'aimantations mesurées sous différentes contraintes élastiques et déformations plastiques. Le modèle prenant directement en compte la déformation plastique, une simulation de processus de poinçonnage mécanique a été réalisée à l'aide du logiciel ABAQUS pour définir la distribution de la déformation plastique sur le bord de coupe. Une simulation éléments finis d'une machine électrique synchrone incluant l'effet du poinçonnage a montré la dégradation de l'induction magnétique au niveau des bords de coupe et une augmentation des pertes fer d'environ 38%. Enfin, les résultats obtenus à partir de la simulation magnéto-mécanique ont été étudiés en termes de méthodes utilisées pour considérer la distribution de la déformation plastique dans le calcul numérique. Deux exemples ont été étudiés : une tôle d'acier et une dent d'une machine électrique. Il a été montré que le profil de dégradation défini par la valeur moyenne de la déformation en fonction de la distance au bord de coupe ne reflète pas la distribution réelle de la déformation plastique. Un ajustement de la méthode de calcul a été proposé.

List of publications

[1] **N. M'zali**, F. Martin, U. Aydin, A. Belahcen, A. Benabou, and T. Henneron, "Determination of stress dependent magnetostriction from a macroscopic magneto-mechanical model and experimental magnetization curves," *Journal of Magnetism and Magnetic Materials*, vol. 500, p. 166299, Apr. 2020.

[2] **N. M'zali**, F. Martin, R. Sundaria, T. Henneron, A. Benabou, and A. Belahcen, "Finite-Element Modeling of Magnetic Properties Degradation Due to Plastic Deformation," *IEEE Transactions on Magnetics*, vol. 56, no. 2, pp. 1–4, Feb. 2020.

[3] **N. M'zali**, T. Henneron, A. Benabou, F. Martin, and A. Belahcen, "Finite Element Analysis of the Magneto-mechanical Coupling Due to Punching Process in Electrical Steel Sheet," *IEEE Transactions on Magnetics*, pp. 1–1, 2021, doi: 10.1109/TMAG.2021.3058310.

List of Symbols and Abbreviations

1. Greek symbols

α	mean field parameter
$\alpha_1, \alpha_2, \alpha_3$	direction cosines of the strain with respect to the crystallographic axes
$\beta_1, \ldots, \beta_5$	parameters of the magnetostriction model
θ_α	orientation angle of the easy magnetization direction
δ_{FS}, δ_{DP}	increase of the magnetic energy when the full strain (FS) distribution is considered and when the degradation profile (DP) is considered
$\boldsymbol{\varepsilon}$	strain tensor
$\boldsymbol{\varepsilon}_\lambda$	magnetostrictive strain tensor
ε	plastic strain
$\dot{\varepsilon_0}, \dot{\varepsilon}$	initial strain rate, and strain rate
ε_f	failure strain
$\lambda_{100}, \lambda_{111}$	saturation magnetostriction in the ⟨100⟩ and ⟨111⟩ directions, respectively
λ	magnetostriction along the magnetization direction
μ	permeability
μ_0	permeability of vacuum
υ	Poisson's ratio
ν	magnetic reluctivity
$\nu_{(B,\varepsilon)}$	magnetic reluctivity function magnetic flux density B and the plastic strain ε
$\nu_{(H,\varepsilon)}$	magnetic reluctivity function magnetic field H and the plastic strain ε
ϑ_p	punching tool velocity
ξ_d	dislocation density
ξ_{d0}	initial dislocation density (prior to the plastic deformation)
$\boldsymbol{\sigma}$	stress tensor
σ	stress
σ_m	ultimate stress
σ_y	yielding stress
σ_F	hardening stress
σ_0, τ	magnetostriction model parameters
σ_{eq}	equivalent stress
$\sigma_{xx}, \ldots, \sigma_{zz}$	components of stress tensor in XYZ-coordinate
σ_{xx}	stress aligned with the magnetic field
ϕ	magnetic flux
ψ	weighting function
ξ, η, ς	reference coordinate Gauss points of a tetrahedron element
χ	magnetic susceptibility

2. Latin symbols

a	anhysteretic scaling parameter (Langevin function)
$a_{(\varepsilon)}$	anhysteretic scaling parameter function of the plastic strain ε
a_1, a_2	anhysteretic scaling parameters (double Langevin or modified Brillouin functions)
$\boldsymbol{A}$	magnetic vector potential
$\boldsymbol{b}$	Burgers vector
$\boldsymbol{B}, B$	magnetic flux density vector, magnetic flux density magnitude
$B_{(H,\varepsilon)}$	magnetic flux density function of the magnetic field H and the plastic strain ε
c	punch-die clearance
C_1, C_2	parameters of the magnetostriction model
c_r	reversibility coefficient
d	grain size
E_d, E_0	magnetic energy with and without considering the punching effect, respectively
f	frequency
F	force
G	shear modulus
$\boldsymbol{H}, H$	magnetic field vector, magnetic field magnitude
$H_{(B,\varepsilon)}$	magnetic field function of the magnetic flux density B and the plastic strain ε
H_c	coercive field
H_D	demagnetizing field
H_e	effective field
H_v	hardness
HV	Viker hardness
H_σ	magneto-mechanical field
J_s	source current density
k	wall pinning parameter
K_0, K_1, K_2	anisotropy coefficients
M	magnetization
M_{an}	anhysteretic magnetization
M_{irr}	irreversible magnetization
M_{rev}	reversible magnetization
M_s	saturation magnetization (Langevin function)
M_{s_1}, M_{s_2}	saturation magnetizations (double Langevin and modified Brillouin functions)
$\boldsymbol{m_o}$	orbital magnetic moment
$\boldsymbol{m_s}$	spin magnetic moment
N_D	demagnetizing factor
$\boldsymbol{N}_\phi$	vector considered to impose the magnetic flux ϕ
r_p, r_d	punching tool radius and die radius

t	sheet thickness
Y	Young modulus
$w_{n,a,f,v}$	interpolation functions (node, edge, facet, and volume)
W_{ech}	exchange energy
W_{an}	anisotropic energy
W_{mag}	magneto-static energy
W_{σ}	magneto-elastic energy
W_{α}	domain free energy

3. Abbreviation

1D	one dimensional
2D	two dimensional
3D	three dimensional
BH	magnetic flux density vs magnetic field (curve)
DAZ	degradation affected zone
D-H	Daniel Hubert (equivalent stress)
DP	degradation profile
FEM	finite element method
Fe-Si	silicon iron alloy
ISO	international organization for standardization
MOKE	Magneto-Optical Kerr Effect (microscope)
JAS	Jiles-Atherton-Sablik (model)
RD	rolling direction
SST	single sheet tester

4. Common Operators

coth	hyperbolic cotangent
$\boldsymbol{div}$	divergence
$\boldsymbol{grad}$	gradient
$\mathfrak{L}$	Langevin operator
$\boldsymbol{curl}$	rotational
tanh	hyperbolic tangent

Introduction

Introduction

1. Background and aims of the thesis

The most important industrial challenge of nowadays is certainly environmental. In fact, the increase of global energy consumption strongly impacts on global warming. It has been reported that rotating electrical machines consume more than 40% of the total global electricity consumption [1].

Thus, to reduce the global carbon footprint, the International Electrotechnical Commission imposed efficiency standards for electrical motors (IEC:60034-34, 2014). Consequently, to improve the performances of electric machines, while maintaining optimum efficiency, efficient numerical models are required for the design process. These models must include accurate representation of the physical phenomena underlying the energy conversion process as well as the accurate representation of materials that constitute the electrical machines. Also, the design process, and consequently the employed models, must take into account the various influencing parameters during the operation and manufacture of electrical machines.

In this context, the work proposed in this thesis deals with the impact of manufacturing processes on the properties of the magnetic materials that make up electrical machines. Indeed, the ferromagnetic cores of electrical machines undergo different shaping and assembly processes to which the properties of the materials are very sensitive, therefore, the performance of machines and their energy efficiency. It has been shown that the manufacturing processes may generate significant plastic strain as well as thermal stresses that lead to the degradation of the magnetic properties of the magnetic cores. For example, it has been measured about 28% increase of iron losses in an electrical machine due to the cutting process [2].

This degradation of magnetic performances must be integrated in the design process of electrical machines in order to allow, on one hand to determine the real performances of the machine and on the other hand to anticipate and to act upstream on the manufacturing process parameters. Different industrials are interested on this problem, especially the automotive supplier, where the effect of manufacturing processes occupies an ever more prominent place. Indeed, these aspects become crucial in modern electrical machines, such as electrical mobility, for which the design must be realized as precisely as possible according to the application requirements.

The work of this thesis aims to develop a methodology and its associated tools to simulate the impact of the mechanical punching process on magnetic properties of electrical steels that compose electrical machines. This cutting process represents the most used technique for large series production of electrical machines. It is characterized by the concentration of plastic strain near the punching edges. Thus, the modeling chain from the mechanical punching process till its effect on the magnetic properties requires to estimate the mechanical state of the punched material at the cutting edge. In the proposed work, a mechanical simulation of the cutting process has been carried out to obtain the plastic strain distribution. Then, based on the literature, the scalar Sablik model

with some improvements has been considered to account for the degraded magnetic properties at the edges of electrical steels. This model allows to describe phenomenologically the physics of the magneto-mechanical coupling at the macroscopic scale. Finally, a numerical tool based on the finite element method (FEM) has been developed to interface both physics, magnetic behavior, and plastic strain. The effect of the punching process on academic examples as well as on the performances of an electrical machine has been investigated.

2. Scientific contribution

The main scientific contributions of the thesis can be summarized as follows:

- In the magneto-elastic regime, the original Sablik model considers only the effect of uniaxial stress. Thus, to account for the multiaxial stress an equivalent stress has been added. Biaxial measurements have been used for the validation.
- To describe the anhysteretic behavior, the Sablik model uses the Langevin function. The modified Brillouin function has been integrated in the model to have a better representation of the magnetostrictive behavior under elastic stress. Furthermore, the identification method based only on macroscopic magnetization curves measured under compressive and tensile stress was quite simple and gives a good estimation of the magnetostriction.
- Since the Sablik model accounts directly for the mechanical strain, punching process simulations have been performed to estimate the plastic strain distribution near the punching edges. Two examples have been simulated: a steel sheet and a tooth of an electrical machine. The effect of punching parameters, such as the punch-die clearance and sheet thickness, have been investigated.
- The implementation in FEM of the degraded magnetic properties at the punching edges was carried out by considering the “degradation profile”. It approximates the spatial strain distribution given by the punching simulation by an exponential function of the distance from the punching edge.
- The identification method of the “degradation profile” has been compared with the full strain distribution along the sheet thickness as given by punching simulation. The analysis is conducted from the magnetic point of view by comparing the distribution of the magnetic flux density and the total magnetic energy for two examples: a steel sheet sample and a tooth of an electrical machine.
- It has been shown that the degradation profile defined by the average value of the strain at each position from the edge does not reflect the real plastic strain distribution in the steel sheet depth. Indeed, depending on the magnetic flux density magnitude and the dimensions of the studied system, the magneto-mechanical behavior varies substantially. A first approach has been proposed to adjust its method of calculation.

3. Outline of the thesis

This thesis report is divided into four chapters. The current section introduces the research work briefly and summarizes the main findings. Chapter I reviews the main theoretical notions of

ferromagnetism and fundamentals of magneto-mechanical interactions. Then, the relevant experimental and modeling aspects related to magneto-mechanical coupling are reviewed. Chapter II presents the magneto-mechanical model considered to take into account the effect of punching process. The proposed modifications to the model and the identification methodology have been detailed. Subsequently, chapter III describes the modeling chain from the mechanical punching process till its effect on the magnetic properties. The development is illustrated through the analysis of academic example: a steel sheet sample. Chapter IV investigates the effect of punching process, by considering the degradation profile, for academic examples and for an industrial synchronous machine. An analysis of the method used to account for the plastic strain at the punching edge has been performed. Finally, a conclusion summarizing the main findings and some perspectives to this work have been listed.

Chapter I

Literature review

In this chapter, a review of the literature in fields related to this thesis is presented. First the main theoretical notions of ferromagnetism are presented, then the fundamentals of magneto-mechanical interactions in ferromagnetic materials are explained. Particular attention is given to magneto-plastic behavior and dislocations density. Finally, the experimental and modeling aspects of magneto-mechanical coupling are reviewed.

I.1 Magnetism and ferromagnetic materials

To understand the background of magnetic materials and the physical quantities employed to evaluate their magnetic state, some aspects of magnetism are explained in this section [3][4].

I.1.1 Magnetic quantities definitions

According to the scientific discipline where magnetism is involved, the magnetic quantities used can be different. In general, physicists and material scientists are more interested in magnetization and susceptibility, while engineers are usually more concerned with magnetic flux density and permeability.

❖ **Magnetic field**

The motion of electric charges, which forms an electric current, creates a magnetic field H in the surrounding environment. The strength and direction of the magnetic field depend on the density and direction of the electric current, the shape and dimensions of the conductor through which the current flows. The magnetic field H is a vector quantity and has the unit of $(\mathrm{A.m^{-1}})$

❖ **Magnetization**

As illustrated in Fig. I.1, each atom has a magnetic moment which is the contribution of an orbital magnetic moment $\boldsymbol{m_o}$, which results from the rotation of the electrons around the nucleus, and the so-called spin magnetic moments $\boldsymbol{m_s}$ associated to the electrons. Thus, the magnetic moment $\boldsymbol{m}$ of an atom is the vector sum of these two moments.

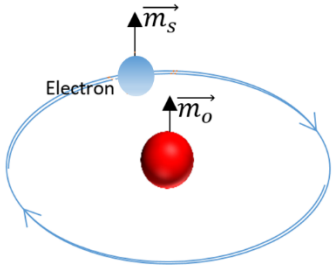

Fig. I.1 Magnetic moments

The magnetization M of a material having a volume v is defined as the total magnetic moment per unit volume, which is:

$$M = \sum_i \frac{m_i}{\mathrm{v}} \tag{I.1}$$

M has the same unit as H, $(\mathrm{A.m^{-1}})$.

❖ **Magnetic flux density**

When a magnetic field is applied to a medium, a magnetic flux ϕ is induced within this medium. The magnetic flux density defines the amount of magnetic flux per unit of cross-sectional area, it is a vector noted B and has the unit of (Tesla).

❖ **Permeability**

All media respond to a magnetic field by a magnetic induction which depends on the magnetization of the medium and the applied magnetic field:

$$B = \mu_0(H + M) \tag{I.2}$$

where $\mu_0 = 4\pi 10^{-7}\, H.m^{-1}$ is the permeability of vacuum. In a magnetic material, the permeability μ is defined by:

$$B = \mu H \tag{I.3}$$

This permeability reflects the ability of the material to be magnetized with regard to the vacuum, this property is defined by the relative permeability μ_r such that:

$$\mu = \mu_0\mu_r \tag{I.4}$$

In the vacuum, M is equal to zero and μ_r is therefore equal to one, and it is dimensionless.

❖ **Susceptibility**

The magnetization M of a material (material's response) can be written as a function of the magnetic field H (excitation field) using the magnetic susceptibility χ such as

$$M = \chi H \tag{I.5}$$

Then, from the definition of μ_r, one finds than M can also be related to H by

$$M = (\mu_r - 1)H \tag{I.6}$$

This leads to the following relation between the permeability and the susceptibility.

$$\mu_r = 1 + \chi \tag{I.7}$$

Depending on their magnetic susceptibility χ, the magnetic materials are classically divided into three groups summarized in Tab. I.1.

Tab. I.1 Classification of magnetic materials

Type of Magnetic Material	Susceptibility	Examples
Diamagnetic	$\approx -10^{-6}$	Cu, Au, Si
Ferromagnetic	50 to 10^4	Fe, Ni, Co
Paramagnetic	10^{-6} to 10^{-3}	Al, Pt

For electromagnetic energy conversion, ferromagnetic materials are mostly used thanks to their high magnetic susceptibility that allows to obtain high energy densities for the conversion process. In the following, physical properties of ferromagnetic materials are described.

I.1.2 Ferromagnetic materials

Ferromagnetic materials are characterized by a presence of magnetization at the microscopic scale, even in the absence of an external magnetic field. This particularity is due to the electronic configuration of their chemical composition as well as the crystalline structure which allows magnetic moments to align with each other.

I.1.2.1 Magnetic domain theory

At the macroscopic scale, generally no magnetization is observed. To explain the absence of magnetization at this scale, the theory of Pierre Weiss [4] states that a ferromagnetic material is composed of regions with specific orientations of magnetization. For example, in electrical steels, each metallurgical grain is subdivided into several domains, usually called the Weiss domains. Within each magnetic domain, the magnetization, called *spontaneous* magnetization, is uniform (Fig.I.2). Each domain is delimited by *magnetic domain walls*.

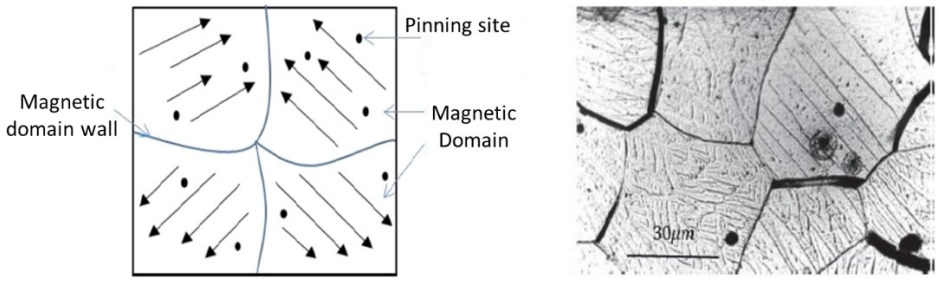

Fig. I.2 Domains in a polycrystalline sample 3% Si-Fe [5]

The magnetic equilibrium and the formation of Weiss domains is explained by the free energy W_α which involves the following energy terms:

- W_{ech} : exchange energy
- W_{an} : anisotropic energy
- W_{mag} : magneto-static energy
- W_σ : magneto-elastic energy

$$W_\alpha = W_{ech} + W_{an} + W_{mag} + W_\sigma \tag{I.8}$$

❖ **Exchange energy**

This energy results from the interaction between two neighboring atoms. The exchange interaction leads to an arrangement of magnetic moments parallel to each other. In ferromagnetic materials, it is minimal if the magnetic moments of two neighboring atoms point in the same direction.

❖ **Anisotropic energy**

The anisotropic energy tends to align magnetic moments along certain crystallographic axes of the material. It is minimum for magnetic moments oriented parallel to a certain crystallographic direction named “easy magnetization direction". As shown in Fig. I.3 the magnetization is function of the direction cosines $\alpha_1, \alpha_2, \alpha_3$, in case of Fe-Si alloys the easy directions are $\langle 100 \rangle$.

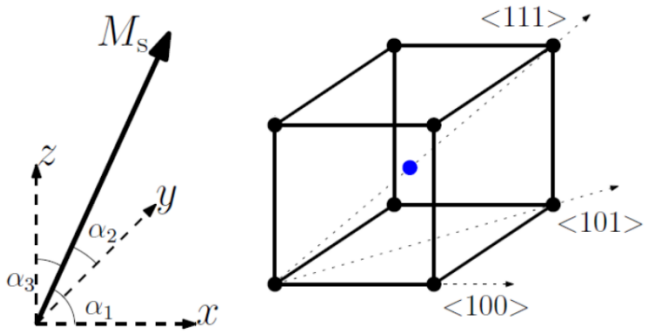

Fig.I.3 Crystallographic axes (x, y, z) and the direction cosines $\alpha_1, \alpha_2, \alpha_3$ of the saturation magnetization M_s of a magnetic domain [6]

The anisotropic energy is given by the relation:

$$W_{an} = K_0 + K_1(\alpha_1^2\alpha_2^2 + \alpha_2^2\alpha_3^2 + \alpha_3^2\alpha_1^2) + K_2(\alpha_1^2\alpha_2^2\alpha_3^2) \quad \text{(I.9)}$$

where K_0, $K_1$and K_2 are the anisotropy coefficients.

❖ **Magneto-static energy**

This energy results from long distance interactions between magnetic moments. Each magnetic moment is subject to a local field created by all other magnetic moments. The magneto-static energy is given by equation (I.10) where H, H_D and M represent, respectively, the applied field, the demagnetizing field and the magnetization.

$$W_{mag} = \frac{1}{2}\mu_0(H + H_D)M^2 \quad \text{(I.10)}$$

In the absence of an external field, the magneto-static energy which will be equal to the demagnetizing energy is given by (I.11), N_D is the demagnetizing factor.

$$W_{mag} = W_D = \frac{1}{2}N_D M_s^2 \quad \text{(I.11)}$$

❖ **Magneto-elastic Energy**

The magneto-elastic energy allows to understand the magneto-mechanical coupling. Assuming a uniform strain within a grain, the magneto-elastic energy W_σ is given by

$$W_\sigma = -\boldsymbol{\sigma}: \boldsymbol{\varepsilon_\lambda} \quad \text{(I.12)}$$

where $\boldsymbol{\sigma}$ is the mechanical stress tensor and $\boldsymbol{\varepsilon_\lambda}$ the magnetostriction strain tensor.

$$\boldsymbol{\varepsilon_\lambda} = \begin{bmatrix} \lambda_{100}\left(\alpha_1^2 - \frac{1}{3}\right) & \lambda_{111}\alpha_1\alpha_2 & \lambda_{111}\alpha_1\alpha_3 \\ \lambda_{111}\alpha_1\alpha_2 & \lambda_{100}\left(\alpha_2^2 - \frac{1}{3}\right) & \lambda_{111}\alpha_2\alpha_3 \\ \lambda_{111}\alpha_1\alpha_3 & \lambda_{111}\alpha_2\alpha_3 & \lambda_{100}\left(\alpha_3^2 - \frac{1}{3}\right) \end{bmatrix} \quad \text{(I.13)}$$

In (I.13) λ_{100} and λ_{111} are the saturation magnetostriction coefficients in the $\langle 100 \rangle$ and $\langle 111 \rangle$ directions, respectively. The magnetostriction phenomenon will be detailed in section I.3.2.1.

I.1.2.2 Magnetization mechanism

The minimization of the free energy mentioned previously leads to a structure described by the Weiss magnetic domains. The application of a sufficiently strong external magnetic field will cause the disappearance of the domain structure and the material acquires a macroscopic magnetization oriented in the direction of the applied magnetic field. Fig. I.4 illustrates the magnetization process and the evolution of the domain structure with respect to the applied magnetic field from the demagnetized state "a" to the saturation state "d".

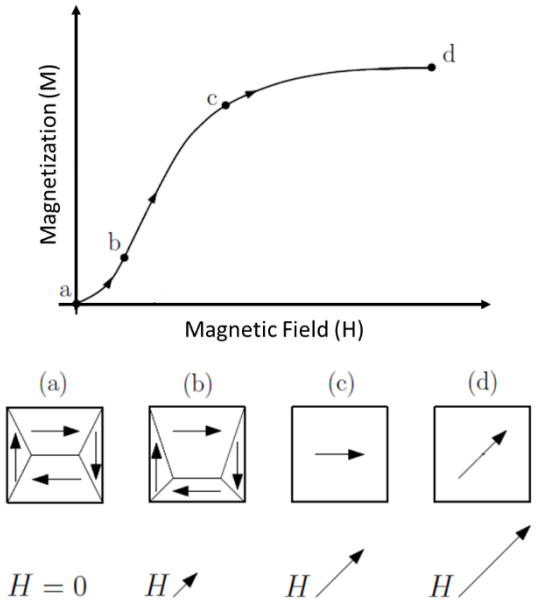

Fig I.4 Mechanism of ferromagnetic material magnetization [6]

At point "b" (Fig I.4) the external magnetic field causes the movement of the walls of magnetic domains of which the spontaneous magnetization direction is close to that of the applied field. This phenomenon leads to the expansion of domains favorable to the external magnetic field. As the magnetic field increases, all domains tend to its direction (point "c" Fig I.4) and domains walls will vanish. Then, the applied energy becomes sufficiently strong to cause the rotation of domains and align them with the magnetic field direction (point "d" Fig I.4).

The mechanism presented above describes the magnetization process of a material which has not been magnetized and the resulting curve is called the first magnetization curve. Under these conditions, if we decrease the intensity of the applied field, the curve M(H) will deviate from the first magnetization curve. Indeed, within ferromagnetic materials there are many crystalline imperfections due to metallurgic processes (carbides, nitrides, cementite, dislocations ...), they constitute the *pinning sites* which oppose the domain wall motion and are associated to energy dissipation within the material. The associated macroscopic phenomenon is called the magnetic hysteresis. As illustrated in Fig. I.5, when the material is subjected to cyclic excitation, a hysteresis loop is obtained.

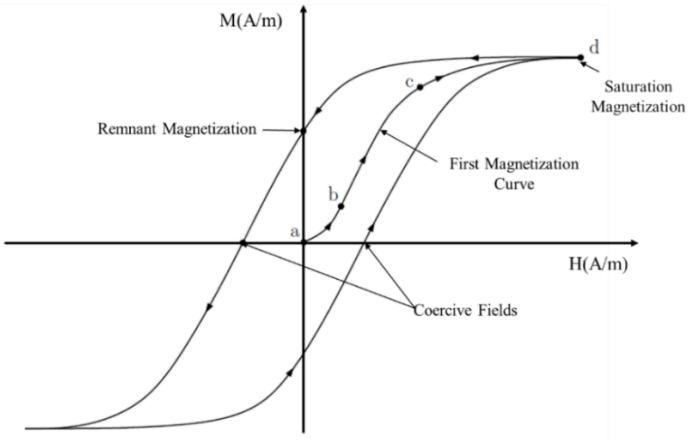

Fig I.5 Hysteresis loop

The hysteresis loop has specific points:
- Saturation magnetization: specific to any material and corresponds to the state where there is no longer any domain structure in the material.
- Coercive field: it corresponds to the excitation field for which the magnetization is canceled.
- Remanent magnetization: magnetization obtained when the external magnetic field H passes through zero.

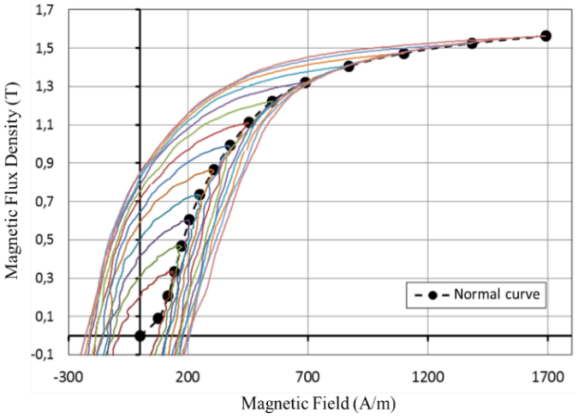

Fig I.6 Construction of a normal curve [7]

Due to experimental difficulty determination of a first magnetization curve, another curve called *normal magnetization curve* is often measured. The ferromagnetic material is excited by a cyclic

magnetic field. The maximum excitation field H_{max} is varied monotonously in order to obtain a set of hysteresis loops as shown in Fig. I.6. Thus, the normal magnetization curve corresponds to the B-H curve obtained by connecting the maxima ($B_{max} - H_{max}$) of each loop.

Another type of B-H curve is often used to describe the ideal magnetization process is called the *anhysteretic curve*. This latter represents the case where the magnetization process is not associated to any energy dissipation. An approximation of the anhysteretic may be obtained by averaging the upper and lower envelopes of a major hysteresis loop.

I.2 Microstructure and mechanical properties

I.2.1 Crystalline structure and defects

A crystalline material is influenced by the presence of defects which make it different compared to a perfect single crystal. There exist four types of defects: point defects (0D), line defects (dislocations) (1D), surface defects (2D) and volume defects (3D).

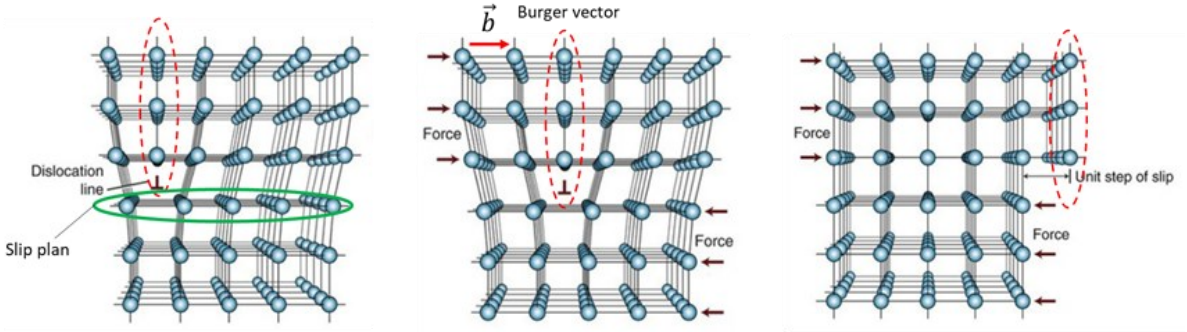

Fig. I.7 Mechanism of generation and motion of edge dislocation [8]

As shown in Fig.I.7 the dislocation is defined as a slipping of a part of the crystal along a plane of atoms. It is characterized by its Burgers vector, which is the direction and the size of the lattice distortion. Two main distinct dislocation types can be distinguished, known as edge and screw dislocations. In an edge dislocation (Fig. I.7), the Burgers vector is normal to the dislocation line. In a screw dislocation the Burgers vector is parallel to the dislocation line. Mixed dislocations exist as well, consisting of edge and screw parts.

Figure I.8 shows the formation of a screw-type dislocation, it consists in the slip of a part of the crystal by a Burgers vector ***b*** along a plane (ABCD).

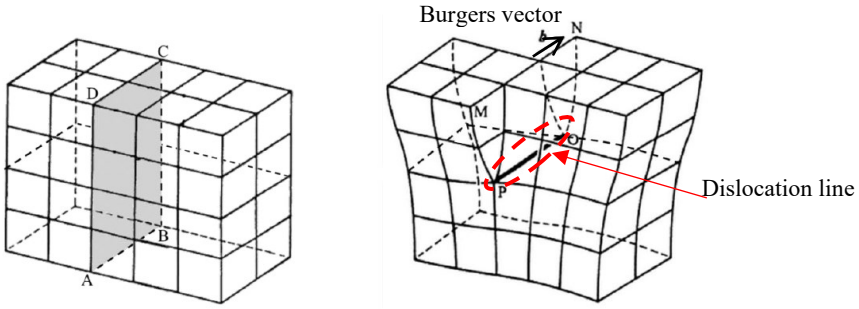

Fig. I.8 Formation of a screw dislocation [8]

- *Dislocation density*

Dislocation is commonly given as a density, which describes the length of line dislocations per unit volume. According to this definition the dislocation density in IS units is given in m^{-2}. Typical dislocation densities in metals are $10^{10} - 10^{16}$ m^{-2} [8].

I.2.2 Strain stress curve

The mechanical characterization of solid materials is ensured by standardized tests; they allow the prediction of the material's behavior under different mechanical constraints. The most common tests are tensile test, compression test, bending test, creep deformation test, and indentation test (hardness measurement). In this section we will focus on the tensile – compression test and the indentation test. These are widely used to study the magneto-mechanical behavior in materials impacted by manufacturing processes.

I.2.2.1 Tensile test – conventional curve

The tensile test is described in standard (ISO 6892-1: 2009 E) [9], it consists in subjecting specimens to an increasing uniaxial force F applied at a given speed, using an electromechanical testing machine. Fig I.9 represents the elongation Δl of a cylindrical specimen, where l_0 is the initial useful length and s_0 its section.

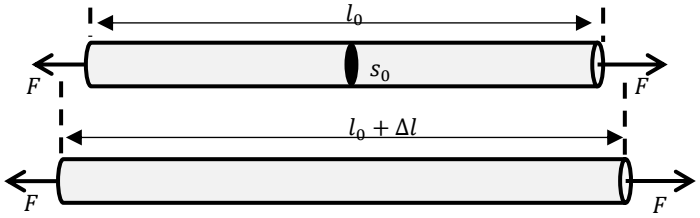

Fig. I.9 Principe of tensile test

The tensile test leads to the curve represented in figure I.10, it gives the evolution of the applied Force F, or the stress $\sigma = F/s_0$, as a function of the elongation Δl, or the strain $\varepsilon = \Delta l/l_0$.

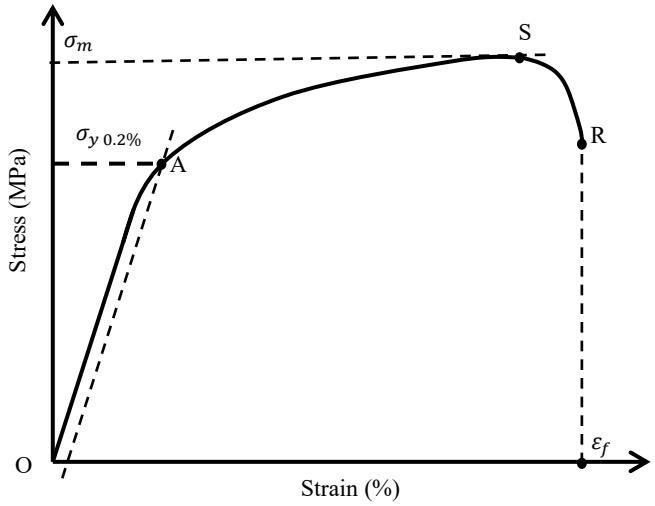

Fig. I.10 Tensile test curve

The analysis of the tensile test curve given in Fig. I.10 allows to define three mechanical zones:

- Elastic zone (OA) where the specimen elongation is reversible below an elastic limit σ_y . In practice, it is difficult to determine the elastic stress from which the material behavior becomes irreversible. Thus, a conventional elastic limit σ_y is defined at 0.2% of plastic deformation.

$$\sigma_{y\ 0,2\%} = \frac{F_{e\ 0,2\%}}{s_0} \tag{I.14}$$

This region is characterized by the Young modulus E which corresponds to the elastic curve slope as expressed in (I.15).

$$E = \frac{dF}{dl}\frac{l_0}{s_0} \tag{I.15}$$

The fundamental relationship between conventional stress σ_c and relative elongation is governed by the Hooke's law given in (I.16):

$$\sigma_c = \frac{F}{s_0} = E\left(\frac{\Delta l}{l_0}\right) = E\varepsilon \tag{I.16}$$

- Hardening plastic zone (AS) where the elongation of the specimen $\Delta l_s = l_s - l_0$ is irreversible, this zone is characterized by σ_m, it defines the maximum hardening stress reached during the test.

$$\sigma_m = \frac{F_m}{s_0} \tag{I.17}$$

- Failure zone (SR) where the load is decreasing, the point of failure R for which the ultimate specimen elongation is expressed by $\Delta l_r = l_r - l_0$, corresponding to the failure strain ε_f.

When the material is subjected to a high tensile stress, the section s_0 of the tested specimen decreases. Thus, the described conventional characteristics can only be used in the elastic range and for low deformations.

I.2.2.2 Rational characteristic

When the deformation is important, the reduction of the specimen section should be taken into account in order to precisely predict the behavior of the materials. We then use the rational characteristics. The rational stress or 'true stress' σ_t is expressed as a function of the instantaneous section s.

$$\sigma_t = \frac{F}{s} = \frac{F}{s_0}\frac{l}{l_0} \tag{I.18}$$

where $s.l = s_0.l_0$ reflects the volume conservation after plastic deformation and then the true stress is finally given by the equation.

$$\sigma_t = \sigma_c\left[\frac{(l_0 + \Delta l)}{l_0}\right] = \sigma_c\left[1 + \frac{\Delta l}{l_0}\right] \tag{I.19}$$

Similarly, the true strain is expressed as a function of the relative elongation.

$$\varepsilon_t = \int_{l_0}^{l_0+\Delta l} \frac{dl}{l} = ln\left(1 + \frac{\Delta l}{l_0}\right) \tag{I.20}$$

From the relations (I.19) and (I.20) which are determined from the experiment, the mechanical behavior can be modeled using the Lüdwick model given by (I.21)

$$\sigma_t = \sigma_0 + k{\varepsilon_t}^n \tag{I.21}$$

where ε_t is the true plastic strain, n is the hardening coefficient, k is a constant related to the material and σ_0 is the yield stress (elastic limit). The Hollomon law can model the mechanical hardening behavior, thus $\sigma_t = k{\varepsilon_t}^n$. The value of the hardening coefficient reflects the inclination of the parabolic portion of the stress-strain characteristic corresponding to the hardening capacity of the material by plastic deformation. Figure I.11 graphically compares the conventional and rational characteristics for a given material.

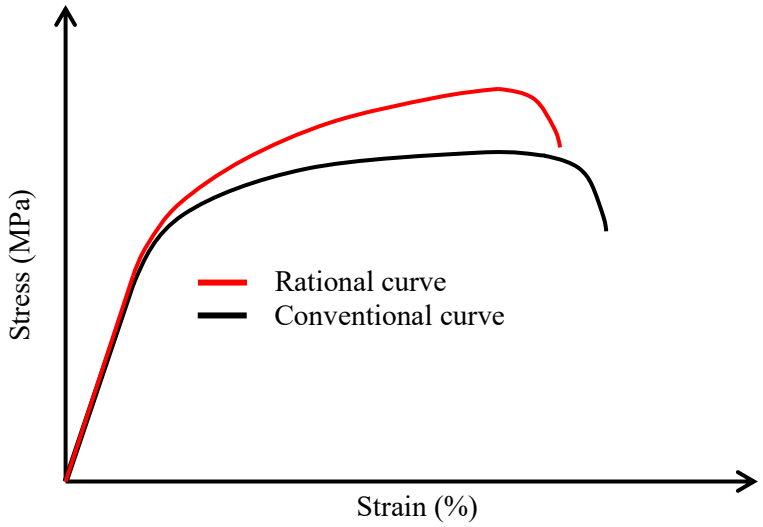

Fig I.11 Stress-Strain behavior: conventional curve and rational curve

I.2.3 Indentation measurement

Indentation testing is a widely used technique for the mechanical characterization of solid materials. It consists in measuring the hardness of a material by driving under a load an indenter which is harder than the material to be tested. The hardness H_v given by (I.22) is defined as the mechanical resistance that the material opposes to the penetration of the indenter.

$$H_v = \frac{P}{A_C} \tag{I.22}$$

where P is the applied force (N) and A_C (mm²) is the surface area of the imprint left by the indenter. Depending on the characterized material type and the maximum load of the indenter, different

techniques are proposed. The geometries of indenters and the characteristics of the most used methods are illustrated in Fig. I.12 According to the indenter size, we can distinguish the micro-indentation and the nano-indentation techniques.

Test	Indenter	Shape of indentation: Side view	Shape of indentation: Top view	Load, *P*	Hardness number
Brinell	10-mm steel or tungsten-carbide ball	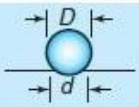		500 kg 1500 kg 3000 kg	$HB = \frac{2P}{(\pi D)\left(D - \sqrt{D^2 - d^2}\right)}$
Vickers	Diamond pyramid			1–120 kg	$HV = \frac{1.854P}{L^2}$
Knoop	Diamond pyramid	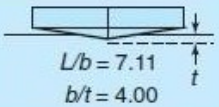	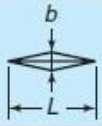	25 g–5 kg	$HK = \frac{14.2P}{L^2}$

Fig. I.12 Characteristics of mean indentation techniques [10]

In addition to the hardness measurement, indentation technique allows to calculate several mechanical properties. It uses the load-displacement curves recorded during load and unload indentation test. In [11] a method which exploits the slope of the unload curve is used to calculate the Young modulus. Furthermore, in [12] the indentation test is used to analyze a creep deformation.

I.3 Impact of manufacturing processes

Ferromagnetic materials used in electromagnetic systems, such as electrical machines and transformers, are subjected to various manufacturing processes. Fig. I.13 represents the general steps for the manufacturing of an electrical machine, the raw material is presented as a steel sheet coil which is first flattened than submitted to the forming process where the appropriate shape and size of components are obtained. For this latter step, various cutting techniques such as laser, punching, and water jet cutting may be used. Once cut, the sheets are stacked, either by welding, gluing, or interlocking. Finally, the housing of the machine is shrink-fitted on the stator core.

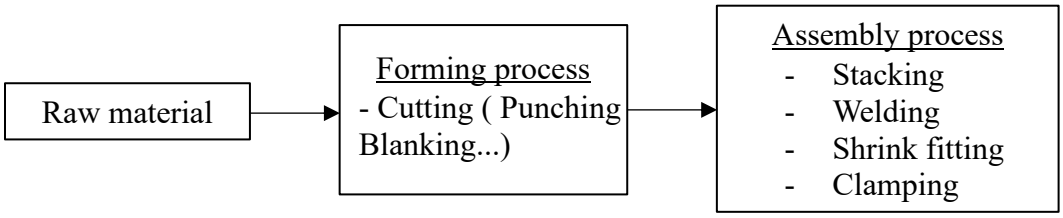

Fig I.13 Manufacturing processes of an electrical machine

Each step of the process is known to degrade the magnetic properties by increasing the iron losses and decreasing the magnetic permeability of electrical steels. In the following subsections, the effects of manufacturing processes are reviewed. Mechanical cutting-related effects are studied in detail.

I.3.1 Cutting process effects

I.3.1.1 Effects of plastic deformation on magnetic properties

Plastic deformation is the consequence of mechanical cutting processes (punching, blanking), it leads to the degradation of magnetic properties and increases the iron loss significantly. Fig. I.14 gives the anhysteretic BH curves of an electrical steel sheet 3%Si-Fe measured under different plastic deformations. The impact is significant even at weak plastic strain 0.45%, the BH curve slope is reduced which leads to the decrease of the relative permeability. Indeed, during the magnetization process of ferromagnetic material, pining sites, including dislocations, hinder the magnetic domain walls motion, thus permeability and BH curves are locally affected.

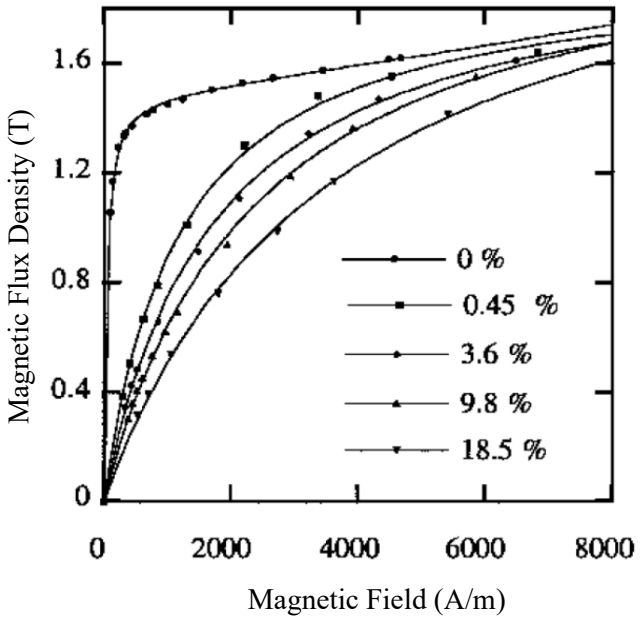

Fig. I.14 Influence of plastic strain on the anhysteretic BH curves of Fe-Si alloy [13]

Thus, the magnetic domain structure that defines the magnetic behavior of ferromagnetic material is strongly affected by plastic deformation. Using the Magneto-Optical Kerr Effect (MOKE) microscope, which consists in the detection of polarization modification of a light beam interacting with the magnetic moments on the surface of the magnetic material, an image of the domain wall structure can be built through contrast post-treatment [14]. For example, the image given in Fig. I.15 shows that, in a region of a few dozens of μm next to the cut edge, no domain contrast is visible when a magnetic field is applied. This indicates that the domain structure did not change under the applied field. This observation is supported by micro-indentation measurements that give an important amount of plastic strain near the cutting edge. It confirms that the domain wall motion is affected by the presence of plastic deformation [16] [17].

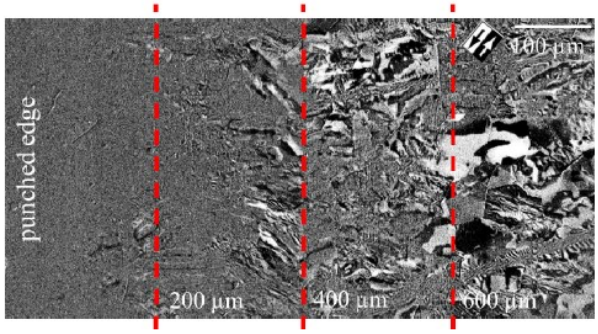

Fig. I.15 Typical MOKE micrograph near a cutting edge [15]

The amount of degradation depends on various factors, such as chemical composition, material, grade, type of cutting technique, settings of the cutting tool, etc… In the literature, different approaches are employed to study the influence of the mechanical cutting. Simple approaches consider only the effect on the macroscopic magnetic quantities of interest while other ones try to link this effect to various physical parameters such as grain size, punch die clearance and the steel sheet thickness.

A. Saleem *et al* [18] carried out an experimental work where the cutting effect on the magnetic properties of two grades of non-oriented electrical steel materials. As shown in Fig. I.16, the degradation is quantified as a function of the cutting length l_{cut}. The sample before cutting is considered as non-degraded and the shear 1 sample is more degraded than the shear 2 sample.

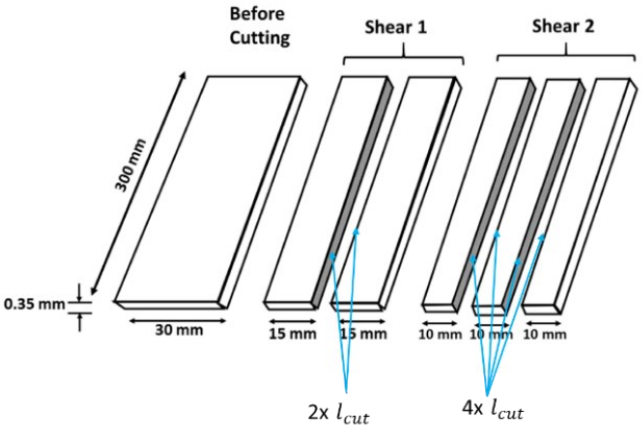

Fig. I.16 Schematic of the cut samples [18]

It was shown that, for both material grades, due to cutting the magnetic losses increase in the whole range of induction from 0.1 to 1.5 T. For the B35AV1900 grade, at 50 Hz and 1.5 T, the relative increase in the total losses is about 20% for the less impacted sample (shear 1) and about 40% for the most degraded one (shear 2). At the same frequency and induction level, for the 35WW300 grade the relative loss increase is about 9% for shear 1 and 23% for shear 2. Similar results were obtained in [19], [20] and [21].

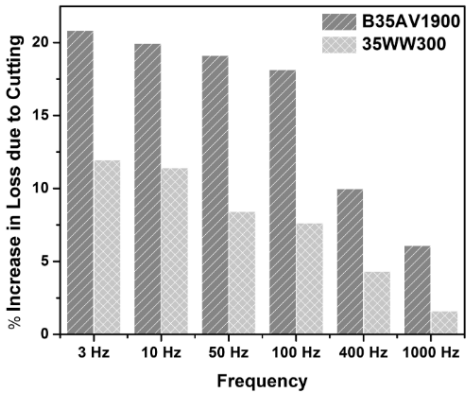

Fig. I.17 Increase in core loss, for shear 1 sample, as a function of frequency, at 1.5 T, for B35AV1900 and 35WW300 electrical steels [19]

Figure I.17 gives the evolution of the relative increase of core losses due to the cutting effect as a function of frequency. The increase is higher for B35AV1900 than for 35WW300, and it decreases with the increase of frequency for both grades. This can be explained by the fact that at lower frequency the hysteresis static loss component is dominant. These results show that the static magnetic behavior is strongly sensitive to the cutting effect which impacts directly the hysteresis parameter such as coercivity and remanence [22] [23]. At higher frequency, the eddy current loss component becomes more dominant and is not significantly affected by cutting [24].

The common cutting process of electrical steel sheet used in the manufacturing of electrical machines is schematized in Fig I.18, it represents a punching process with the relevant parameters which have an impact on the cutting quality.

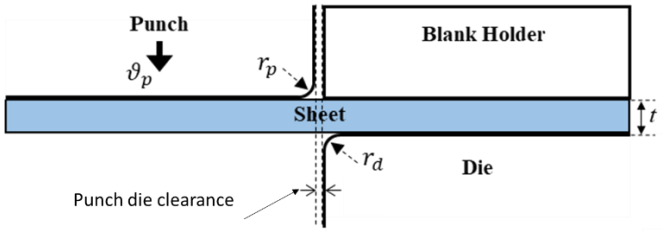

Fig. I.18 Geometry and relevant parameters of the punching process

The effect of non-oriented electrical steel sheet thickness on core loss deterioration by the punching process has been investigated in [25] and [26]. It was found that thinner sheet exhibits less iron loss deterioration. Furthermore [27] and [28] reported that high Si-alloyed grade electrical steels with large grain size are more sensitive to the deterioration of magnetic properties in the punching process.

Subramonian *et al.* [29] investigated the mechanical effect of the punching process parameters on various steel sheet of 0.25 mm and 0.8 mm thicknesses with experimental tests. The punch-die clearance is the most important factor that affects the blanked edge quality. The results showed that the rollover and shear edge increase and fractured edge decrease with increasing punch-die

clearance. In the other hand, Wang et al. [30] analyzed the combined effect of grain size and the punch-die clearance, their optimization reduces the magnetic core loss by 5.8 %.

I.3.1.2 Effect of plastic deformation on dislocation density

Due to the importance of dislocation in a magneto-plastic coupling, this section is dedicated to their evolution during a material rupture process. Figure I.19 shows the different zones of a stress-strain curve. In [31], the evolution of dislocation structure has been studied for each zone. First, the observations of the material in its initial state (elastic zone Fig I.19) reveal a low dislocations density, about $10^{12}\ m^{-2}$. Then, at the beginning of a plastic deformation (strain Lüders plateau, Fig. I.19) the hardening stress is homogeneous, and the dislocations density increases significantly compared to the initial state. This stage is characterized by the formation of the dislocation clusters. Finally, At the further plastic deformation (strain hardening zone Fig I.19), the dislocation clusters multiply and densify, while the matrix which separates them is proportionally depleted in mobile dislocations.

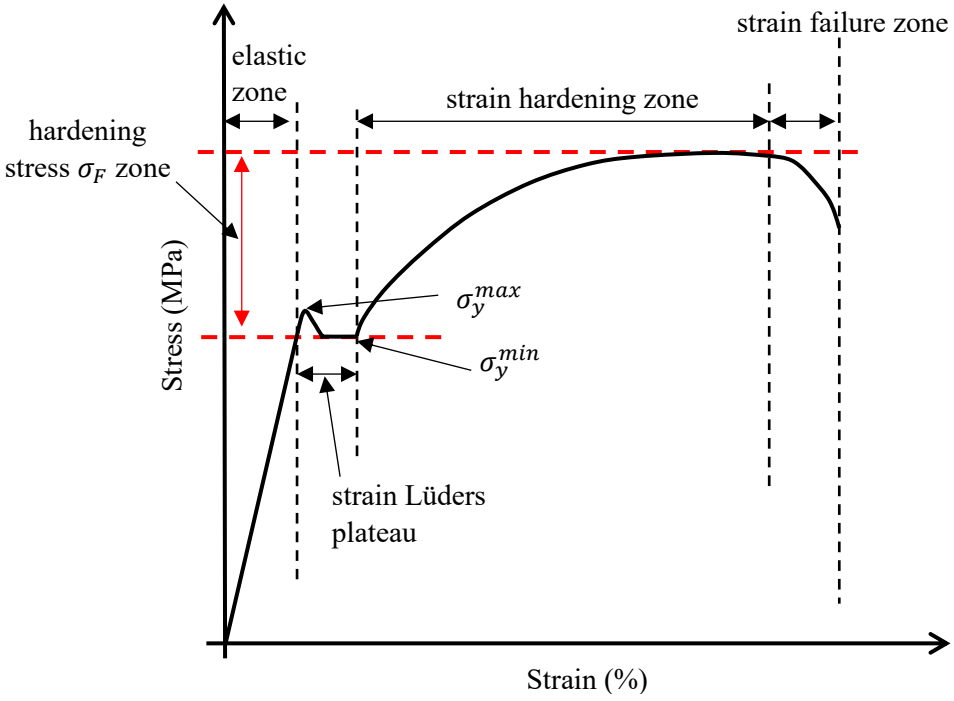

Fig. I.19 Stress strain curve of an electrical steel

It has been shown that the dislocation density at the cutting edge is more important in the upper surface compared to the lower surface (Fig. I.20) [17].

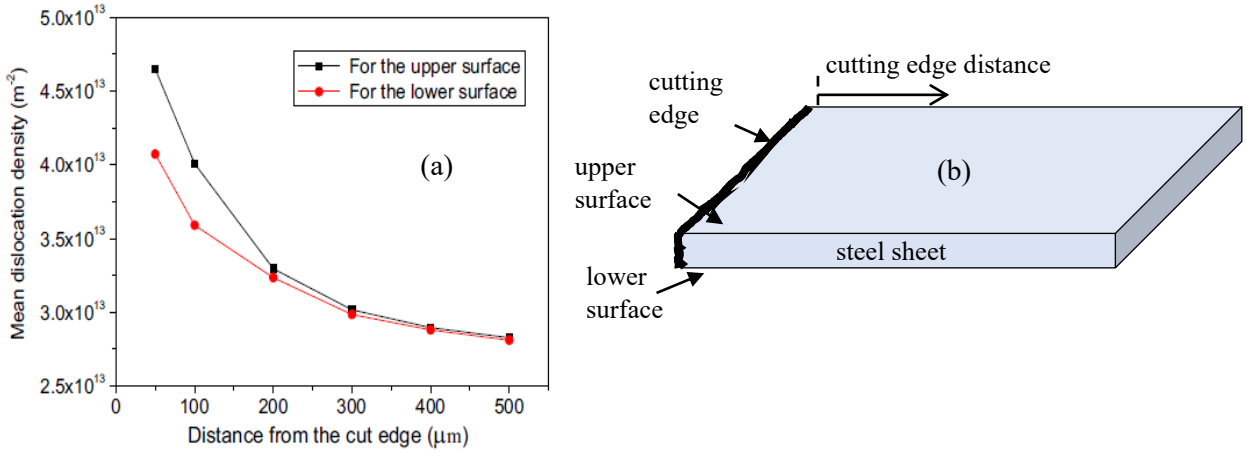

Fig I.20 Evolution of dislocation density near a cutting edge (b) Schematic of punched steel sheet [17]

I.3.1.3 Plastic deformation at the cutting edge

The determination of the distribution of the plastic strain represents an important step in the magneto-mechanical modeling process treated in this thesis. Indeed, cutting process induces plastic strain and residual stress which are concentrated near cutting edges thus delimiting a "deformation affected zone" (DAZ). Depending on the material type, the thickness, and other material parameters such as grain size the width of the DAZ may extend up to 15 mm away from the cut edge [32]. Whereas [33] postulated that the affected area is less than 10 mm wide, [34] measures a penetration depth of 0.4 mm.

In the literature the hardness measurement technique presented previously is widely used to characterize the plastic state of the DAZ. Although, the principle based on the nano-indentation is common to all the proposed methods, the experimental approaches are different. In [35] the equivalent plastic strain and its evolution with the distance from the cutting edge is computed on the top surface of the punched part. As illustrated in Fig. I.21 The distance between two adjacent indents is $\delta = 25$ µm. Due to sensitivity of the nano-indentation to the surface shape, the first indent is located at a distance of 100 µm from the cutting edge.

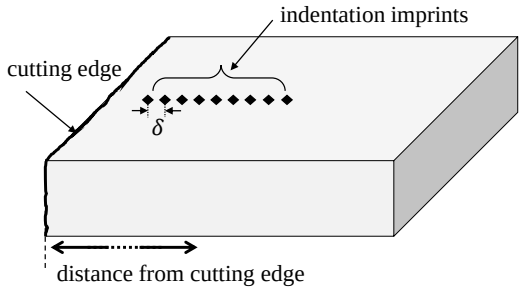

Fig. I.21 illustration of nano-indentation

Then, to estimate the plastic strain, a finite element inverse analysis of the nano-indentation test is performed. The identification technique consists in calibrating the parameters of the yielding stress

σ_y given in (I.23) in order to approach the simulated load-displacement curve to the curve obtained experimentally. The value of the equivalent plastic strain ε is thus deduced.

$$\sigma_y = k(\varepsilon + \varepsilon_0)^n \tag{I.23}$$

ε_0 is the parameter to be calibrated, it represents the initial equivalent plastic strain. The hardening exponent n and the material parameter k are determined from tensile tests. Figure I.22 gives the evolution of the equivalent plastic strain in the vicinity of the cutting edge.

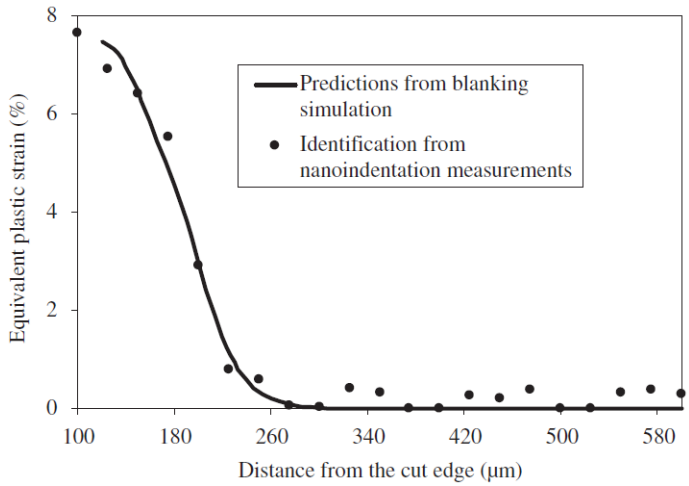

Fig. I.22 Equivalent plastic strain evolution in the vicinity of the cut edge [35]

A method to convert hardness measurements into equivalent plastic strain has been proposed in [36] [37]. This method is based on the estimation of the elastic and plastic indentation work using the load – displacement curve. In the work presented by Ossart *et al* [16], a phenomenological relationship is established between micro-indentation hardness measurements and equivalent plastic strain. The proposed formula (I.24) gives the Vickers hardness HV as a function of an equivalent plastic stain.

$$HV(\varepsilon) = HV_0 + \alpha\varepsilon^m \tag{I.24}$$

where HV_0, α and m are material dependent parameters.

The experimental procedure presented above is insufficient to describe the plastic strain distribution at the cutting edges, in fact the hardness is evaluated on the upper surface of the punched material where the indentation is applied along a straight line. As for the dislocation density, in [17] it was showed that the magnitude of the hardness measured on the upper surface is significantly different from the one measured on the lower surface. Therefore, Weiss et al [38] proposed to evaluate the spatial distribution of the residual stress in the DAZ using a micro-indentation hardness test applied in the cross section of the punched material. As shown in the Fig I.23 a distance between two adjacent indents is $\delta_x = 45$ µm and $\delta_y = 40$ µm.

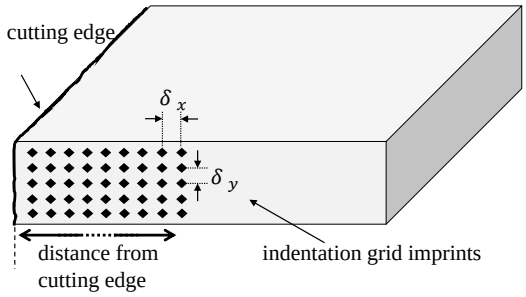

Fig I.23 Micro-hardness measurement grid on the cross-section perpendicular to the cutting edge

The conversion of hardness measurements into residual stress is performed using a finite element simulation of a cutting process calibrated by the load-displacement curves from the micro-indentation tests.

Elastic stresses contribute also to the degradation of magnetic properties. For instance, the shrink fitting process induce compressive stresses on the stator core of electrical machine. Ali *et al*. [39] analysed their effect on non-oriented steel sheet. It was shown that the core loss increases with increasing compressive stress up to 80 MPa. Further, Yamazaki and Takeuchi [40] performed a combined stress electromagnetic FE analysis and estimated an increase of 20 % in iron losses, a decrease of 2 % in torque and a decrease of 1.4 % in efficiency at the maximum speed.

I.3.2 Magneto-elastic coupling

Magneto-elastic coupling phenomena have two main manifestations: the magnetostriction deformation which is known as Joule deformation [41] and the effect of stresses on the magnetization and on the magnetostriction itself.
There is also another deformation that results from the magnetic forces and the magnetization gradients [42]. In this section, only the magnetostriction will be considered.

I. 3.2.1 Magnetostriction process

When a ferromagnetic substance is exposed to a magnetic field, its dimensions change. This effect, which is intrinsic to the material and depends on its magnetic state, is called *magnetostriction*. As shown in Fig. I.24, when an iron single crystal is magnetized to saturation in a [100] direction, the length of the crystal in this direction is found to increase, thus the magnetostriction strain is given as $\lambda = \Delta l/l$. This change is related to domain wall motion as described in the subsection I.1.2.2.

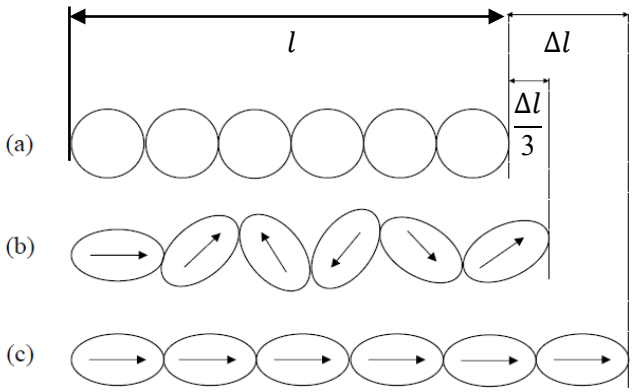

Fig. I.24 Magnetostriction of an iron crystal in the [100] direction: (a) A disorder behavior in para-magnetic regime. (b) Ordered behavior in ferromagnetic regime. (c) ferromagnetic regime with completely aligned domains with respect to the magnetic field [4]

Magnetostriction can be positive, or negative, the deformation occurs at constant volume [43]. Fig I.25 shows the evolution of the longitudinal magnetostriction of certain ferromagnetic materials. Fe and FeCo present a positive magnetostriction with different amplitudes while Nickel (Ni) presents a negative magnetostriction.

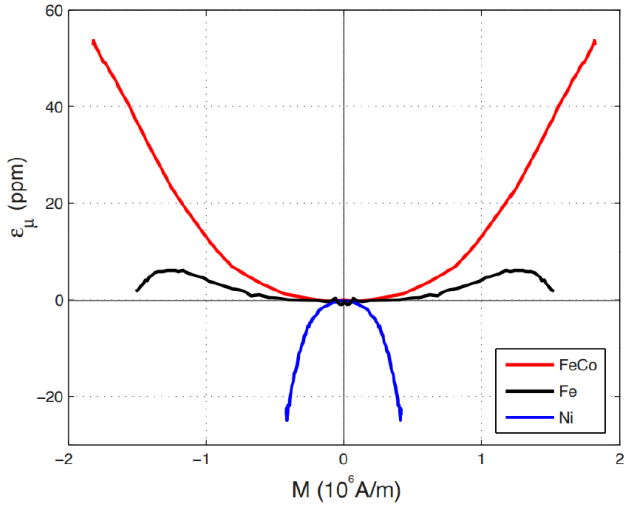

Fig I.25 Longitudinal magnetostriction of some ferromagnetic materials versus magnetization [43]

Along with the magnetization of ferromagnetic materials, the magnetostrictive behavior exhibits a strong non-linearity. This latter is associated with the existence of a maximum magnetostrictive strain, called magnetostrictive saturation strain λ_s. Fig I.26 gives the hysteretic and anhysteretic magnetic behavior (a) and the associated magnetostrictive behavior (b) of a non-oriented iron silicon electrical steel (3% Si-Fe) [44][45].

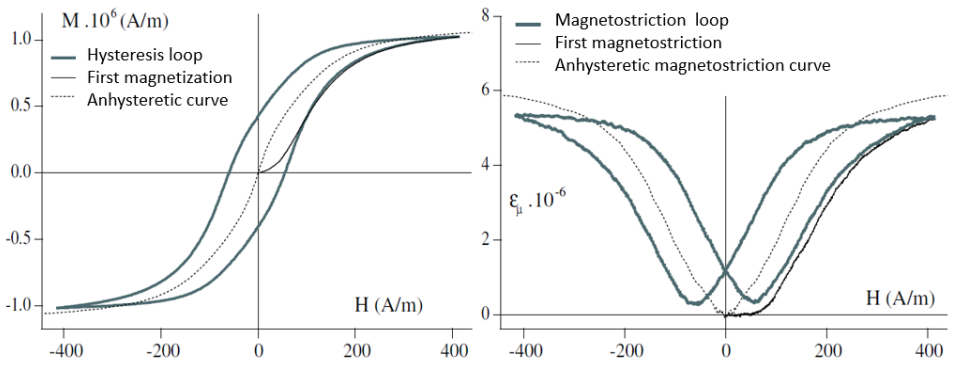

Fig I.26 (a) Magnetic behavior (b) Magnetostrictive behavior [44]

I.3.2.2 Effect of elastic stress on magnetostriction

Compressive or tensile stress induce changes in the magnetostriction, an elastic deformation is added to the magnetostrictive strain already induced by the magnetization of ferromagnetic material. Fig. I.27 shows the peak evolution of the longitudinal magnetostriction measured on a non-oriented steel sample cut in the rolling direction and subjected to different uniaxial tensile and compressive stresses.

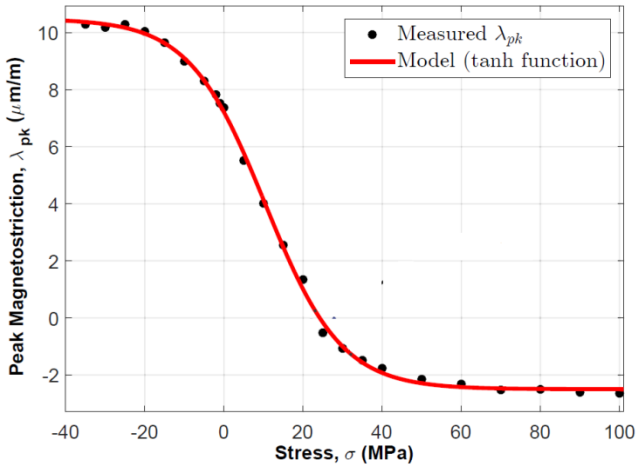

Fig. I.27 Measured and fitted peak magnetostriction λ_{pk} as a function of applied stress σ [46]

Figure I.28 shows the measurements and modeling result of magnetostriction as function of magnetization for different compressive and tensile stresses, the asymmetrical behavior of the $\lambda(M,\sigma)$ is explained according to the result of Fig I.27 where the magnetostriction peak is a tangent hyperbolic function of stress. The maximum magnetostriction is obtained for the compressive stress, it decreases for tensile stress and becomes negative for the higher tensile stresses.

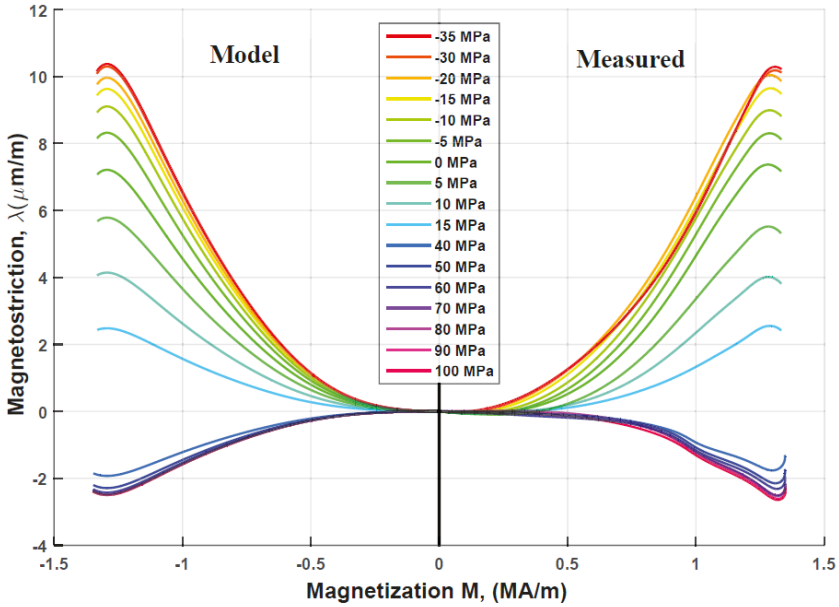

Fig I.28 Magnetostriction function of magnetization under different applied stresses [46]

I.3.2.3 Effect of elastic stress on magnetization

The modification of magnetic material behavior by applying a mechanical stress has long been established. Bozorth [47] measured the magnetic behavior of Nickel under uniaxial stress, he observed that a compressive stress at -70 MPa doubled the initial permeability and uniaxial tensile stress of the same amplitude divided it by 10.

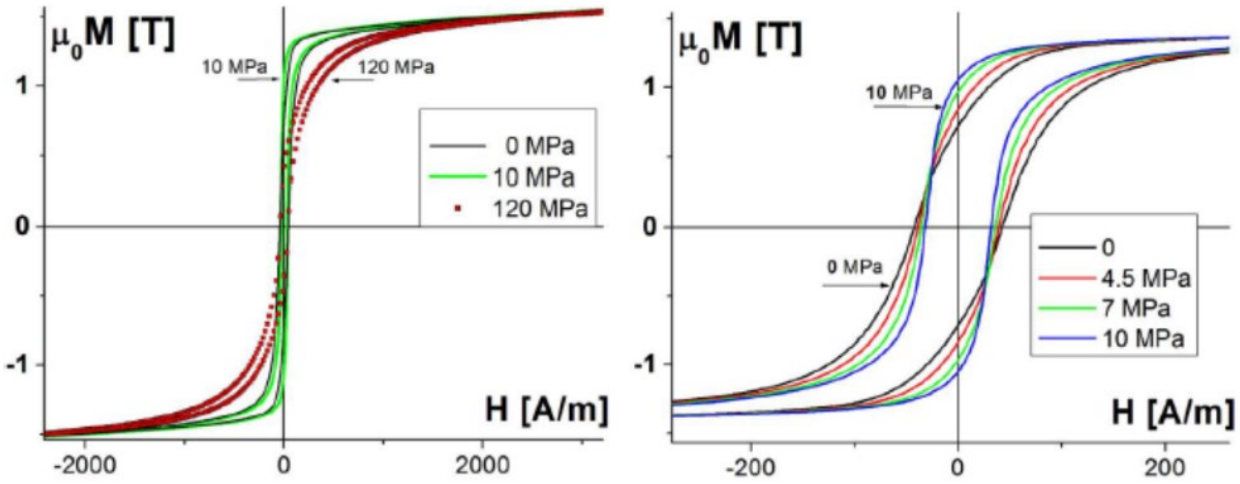

Fig I.29 (a) Hysteresis loops for tensile stress up to 120 MPa (b) and enlarged loops for small stresses below 10 MPa [48]

The behavior of iron is more complex; Fig I.29 shows a measurement of hysteresis loops under tension carried out on 3% Si-Fe. The magnetization is improved at low tensile stresses below 10 MPa and then continuously decreases with further stress increase. This non monotonic change of magnetization was confirmed by different authors [49].

As for the magnetostrictive behavior, the effect of elastic stress on the magnetization is not symmetrical in tensile and compression. In Fig. I.30, when compared to a tensile stress, the degradation of the B-H curve due to a compressive stress is stress is significantly higher. The measurements are carried out on an iron-silicon alloy (FeSi M330-50) under uniaxial mechanical loading. The stress and the magnetic field are applied in the rolling direction of the sheet [50].

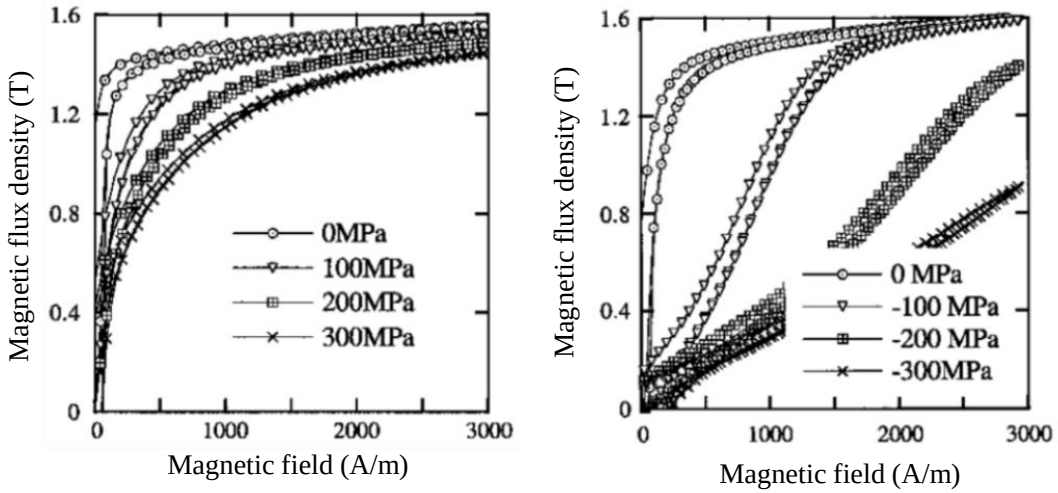

(a) tensile (a) compressive

Fig I.30 Influence of a tensile and compressive stress on the hysteresis cycle of Fe-Si alloy [50]

I.3.2.4 Measurement devices under elastic loading

The measurement of magnetic properties is governed by norms where different standardized devices exist, such as the Epstein frame [51] and the Single Sheet Tester (SST) [52]. However, there are no standard devices for magnetic characterization under mechanical loading. To carry out measurements of magnetic quantities while taking into account the impact of mechanical loading, several devices have been presented in the literature. These devices usually combine standard magnetic characterization methods, in particular the SST associated to a conventional mechanical test device. Depending on the geometry of the sample and the excitation source type, different devices have been published in the literature [53] [54]. The device proposed in [55] uses a 3-phase excitation system to obtain an arbitrary flux density waveform, especially rotating magnetic field, in a hexagonal shaped sample.

For instance, Fig. I.31 illustrates a magnetic characterization device under uniaxial mechanical loading where tensile and compressive stresses can be applied to a Fe-Si steel sheet along the rolling direction (RD), the evolution of the BH curve under stress is obtained from a field sensor and a search coil [46].

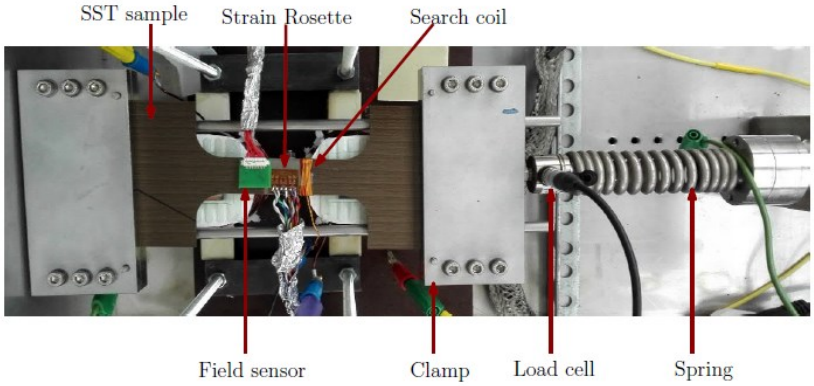

Fig. I.31 SST characterization device under uniaxial stress [46]

In order to characterize the effect multiaxial stress on the magnetic properties, specific measuring devices have been developed. As with uniaxial devices, their construction is based on the adaptation of the standard SST device with a multiaxial mechanical loading device [56]. Figure I.32 illustrates a multiaxial measurement; the hexagonal shape of the setup allows the application of a stress in different directions. The stress magnitude is controlled with servomotors and the measurement area is located in the center of the device.

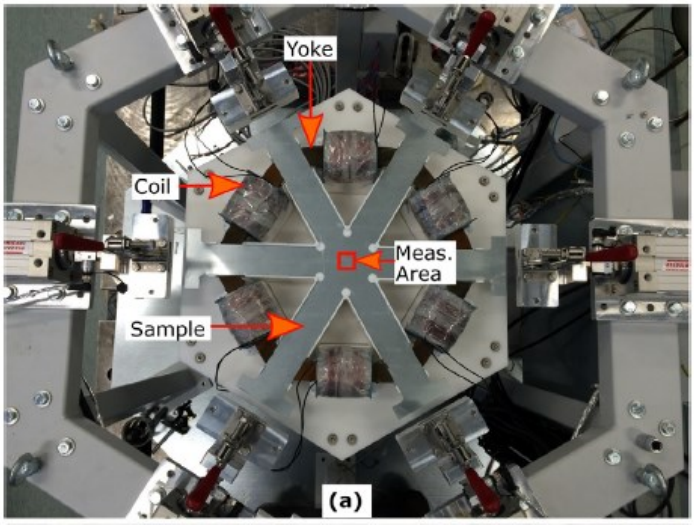

Fig. I.32 Multiaxial measurement device [56]

As shown in this section, the manufacturing processes, which characterized by a magneto-mechanical coupling affect magnetic materials properties and participate to the degradation of electrical machines performances. To anticipate this phenomenon a predictive model is needed. The modeling consists in establishing a relationship between the mechanical quantities (elastic or plastic) and the impacted magnetic quantities (B-H curve, magnetic losses). The next section presents the most commonly used models in the literature.

I.4 Magneto-mechanical modeling

This section presents magneto-mechanical modeling approaches. A classification based on the type of approach is proposed. There are two categories using energetic considerations, microscopic and macroscopic models, and a third category including empirical formulas.

I.4.1 Multiscale model

The multiscale modelling initially proposed by Buiron *et al* [57] [58], is based on an energetic approach for the equilibrium state of a magnetic domain. As illustrated in Fig. I.33, the model is based on three different scales and their associated transition relationships. The energetic behavior at the scale of a magnetic domain is first considered. A change of scale allows to define the behavior at the grain scale where multiple domains can be considered. A second transition law is used to define the behavior of a polycrystal.

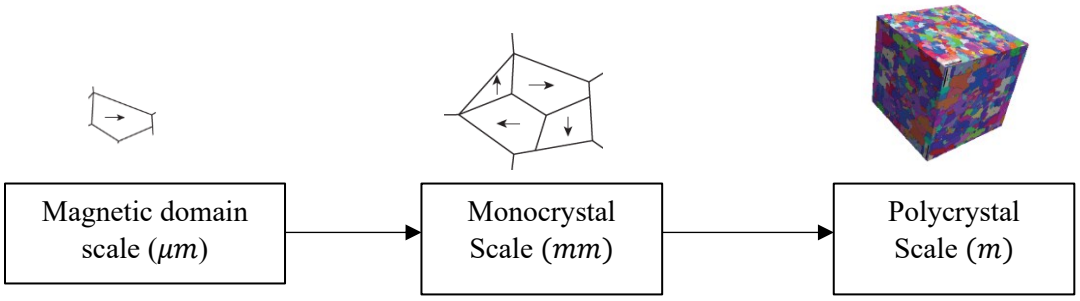

Fig. I.33 Multi-scale approach

- ***Magnetic domain scale***

The model supposes that the magnetization and the magnetic field in a single magnetic domain is uniform and the elastic properties are homogeneous. This uniformity leads to simplifications of different energy terms that compose the total free energy (I.8).
- Since the magnetization in a single domain is unchanged, therefore the exchange energy is equal to zero.
- The anisotropy energy and the magneto-elastic energy are homogeneous,
- The uniformity of the magnetization and the magnetic field leads to the uniformity of the demagnetizing energy. In a single domain, noted with α referring to domain scale, the magneto-static energy is given by:

$$W_{mag} = -\mu_0 M_\alpha H_\alpha \tag{I.25}$$

with H_α the applied field and $M_\alpha = M_s \vec{\gamma}_\alpha$ the domain magnetization where M_s is the saturation magnetization and $\vec{\gamma}_\alpha$ the direction of the magnetization in the domain.

Finally, the magnetic domain state description requires only to know the direction of the magnetization $\vec{\gamma}_\alpha$, which is defined in the crystallographic frame by an angle θ_α. The minimization of the domain free energy W_α leads to following equations:

$$W_\alpha(\theta_\alpha) = min\,(W_\alpha) \tag{I.26}$$

$$\theta_\alpha \in [0, \theta_{max}] \tag{I.27}$$

$$\theta_{max} = acos\left(\frac{\vec{\gamma}_0^\alpha . \vec{H}_\alpha}{\|\vec{H}_\alpha\|}\right) \tag{I.28}$$

where $\vec{\gamma}_0^\alpha$ is the direction of the initial easy magnetization axis and H_α is the applied magnetic field.

- ***Grain scale***

At the grain scale, the assumptions of magnetization uniformity previously stated for a domain is no longer valid. In fact, the structure of a grain is made up of magnetic domains separated by walls where the magnetization varies quickly.
The total free energy in the grain W^{grain} as given in (I.29) is then the sum of two energy terms, one is related to the total magnetic domain volume and the other one is related to the volume occupied by the walls.

$$W^{grain} = \int_{V_d} W^{domain} + \int_{V_p} W^{wall} \tag{I.29}$$

Due to the difficulty to estimate the walls volume and the complexity of their magnetic behavior, equation (I.29) is not adequate to express the scale transition from a domain to a grain. Thus, a phenomenological transition law based on the association of the grain behavior and scalar adjustment variable is used to connect domain scale to grain scale.

In this approach, magnetic domain families are defined. They correspond to directions of easy magnetization which are defined by two parameters: the orientation angle θ_α and the volume fraction f_α.

$$f_\alpha = \frac{\exp\,(-A_s . W_\alpha)}{\sum_\alpha \exp\,(-A_s . W_\alpha)} \tag{I.30}$$

$$\sum_\alpha f_\alpha = 1 \tag{I.31}$$

where A_s is an adjustment parameter which allows to take into account the effect of magnetic domain walls.
The mean value of the magnetization M^{grain} and the mean value of the magnetostriction strain tensor $\boldsymbol{\varepsilon}_{\boldsymbol{\lambda}}^{\boldsymbol{grain}}$ at the grain scale are given by (I.32) (I.33) respectively.

$$M^{grain} = \langle M_\alpha \rangle = \sum_\alpha f_\alpha . M_\alpha \tag{I.32}$$

$$\boldsymbol{\varepsilon}_{\boldsymbol{\lambda}}^{\boldsymbol{grain}} = \langle \boldsymbol{\varepsilon}_{\boldsymbol{\lambda}}^{\boldsymbol{\alpha}} \rangle = \sum_\alpha f_\alpha . \boldsymbol{\varepsilon}_{\boldsymbol{\lambda}}^{\boldsymbol{\alpha}} \tag{I.33}$$

- ***Poly-crystal scale***

At the polycrystal scale, the mechanical stress and mechanical strain are not homogenous as considered at the grain scale. Indeed, the difference in crystallographic orientation of adjacent grains in the same polycrystal generates mechanical heterogeneity.

The transition scale from a grain to a polycrystal is expressed as a connection of the applied macroscopic quantities ($\boldsymbol{\sigma_{ext}}$ and H_{ext}) with the local quantities at the grain scale ($\boldsymbol{\sigma_{\alpha}}$ and H_{α}) by a set of localization laws in terms of magnetic field and mechanical stress. The assumption of a homogeneous medium equivalent to the polycrystal where each grain is considered as a spherical inclusion gives the following localization laws:

$$\boldsymbol{\sigma_{\alpha}} = \mathcal{G}(H_{ext}\,, \boldsymbol{\sigma_{ext}}\ ) \tag{I.34}$$

$$\boldsymbol{\sigma_{\alpha}} = \boldsymbol{\sigma_{ext}} + \ \boldsymbol{C}^{*}\colon \left(\boldsymbol{E} - \boldsymbol{\varepsilon_{\alpha}^{\lambda}}\right) \tag{I.35}$$

$\mathcal{G}$ is an auto-coherent function, $\boldsymbol{E}$ is the total strain, $\boldsymbol{C}^{*}$ is the Hill tensor and $\boldsymbol{\varepsilon_{\alpha}^{\lambda}}$ is the magnetostriction strain tensor at the domain scale. Also, $H_{d\alpha}$ is the demagnetizing field at the domain scale such as:

$$H_{\boldsymbol{\alpha}} = \mathcal{G}(H_{ext}\,, \boldsymbol{\sigma_{ext}}\ ) \tag{I.36}$$

$$H_{\boldsymbol{\alpha}} = H_{ext} + H_{d\alpha} \tag{I.37}$$

To solve this problem, various modifications and simplifications have been proposed in the literature. Instead of minimizing the total free energy, the use of Boltzmann type distribution function has been proposed in [58]. Later, Vanoost *et al* [59] proposed a correction parameter for the calculation of the Boltzmann distribution under stress with better accuracy. To consider the hysteretic behavior of ferromagnetic material Daniel *et al.* [60] introduced an irreversible contribution.

Although they have a strong physical basis, the main limit of multiscale modeling approaches concerns their efficient integration in the numerical simulations tool of electromagnetic phenomena. Indeed, the computational cost is relatively high despite the simplification of the full multiscale model published for the anhysteretic behavior [61] and for the hysteretic behavior [62][63].

I.4.2 Macroscopic models

The macroscopic approach of magneto-mechanical modeling uses macroscopic magnetic and mechanical quantities. It is generally based on the modification of models already developed for hysteretic and anhysteretic magnetic behavior by introducing a new term to take into account the impact of mechanical loadings.

- **Modified Preisach model**

The Preisach model is a phenomenological approach of the magnetic hysteresis modeling. In this model, the magnetic material is associated to a distribution of elementary hysteresis loops,

called hysterons, for which the magnetic state is represented by two possible saturation levels, $M = \pm 1$. From the description of the pinning and unpinning of a domain walls, the hysterons are defined as asymmetric elementary loops associated to asymmetric switching fields, denoted as α and β in Fig. I.34. The magnetic material is then described by its statistical distribution $\rho(\alpha, \beta)$ of elementary loops [64] [65]. Finally, the reconstruction of the material hysteresis loop requires knowing the statistical distribution of elementary loops given for any $H(t)$:

$$M(t) = \iint \rho(\alpha, \beta)\phi_{\alpha\beta}H(t)d\alpha\, d\beta \tag{I.38}$$

where $\phi_{\alpha\beta}$ represents an operator associated with the elementary magnetic cycle and $\rho(\alpha, \beta)$ represents the Preisach distribution function, which is characteristic of the considered material.
From physical considerations, especially the dissipative property of magnetic hysteresis, the domain definition of the Preisach distribution is a triangle with surface S in the Preisach plane defined in Fig. I.34-b. In this figure, $L(t)$ is a variable which divides the domain S, and makes possible to define the magnetic state at any time $M(t)$.

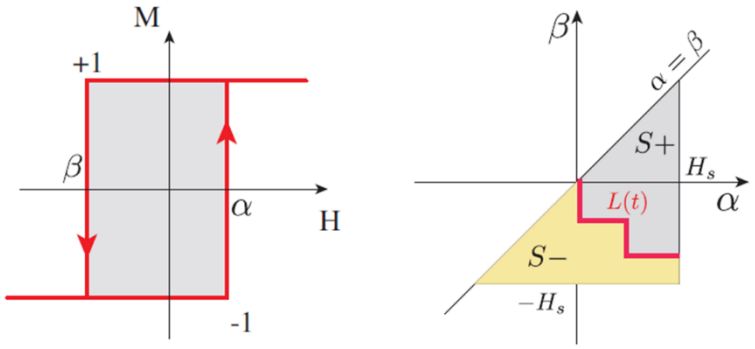

(a) Elementary loop (b) Preisach plan

Fig. I.34 Preisach model construction [65]

In the modified Preisach model for magneto-mechanical modeling, this distribution is expressed as a function of stress. Sipeky *et al.* [66] introduced a stress dependency into the Preisach distribution function to model the effect of uniaxial tensile stress on magnetic hysteresis.

$$\rho(\alpha, \beta, \sigma) = \begin{cases} exp\left(\left(\dfrac{\left(\alpha - \beta - (c + g\sigma)\right)^2}{10^{a+e\sigma}} - \dfrac{\left(\alpha + \beta - (d + h\sigma)\right)^2}{10^{b+f\sigma}}\right)\right), & \alpha + \beta \leq 0 \\ exp\left(\left(\dfrac{\left(\alpha - \beta - (c + g\sigma)\right)^2}{10^{a+e\sigma}} - \dfrac{\left(\alpha + \beta + (d + h\sigma)\right)^2}{10^{b+f\sigma}}\right)\right), & \alpha + \beta \leq 0 \end{cases} \tag{I.39}$$

where a, b, c, d, e, f, g, h are the model's parameters, they are identifiable using experimental data.

The major difficulty in magneto-mechanical modeling, when using the Preisach model, is the accurate definition of the distribution function. Indeed, it requires a large amount of experimental data for the model identification.

❖ **Jiles-Sablik model**

This model, based on a macroscopic energy approach, was initially developed by Jiles and Atherton [67] [68] to model hysteretic behavior of ferromagnetic materials. It has been extended to account for mechanical effect in the elastic region by the introduction of a magneto-elastic field which is added to the effective magnetic field.

In the original magnetic hysteresis model, Jiles and Atherton consider the total magnetization M as a sum of two contributions: reversible and irreversible (equation I.40). The reversible component M_{rev} represents the reversible motion of the magnetic domain walls and the reversible rotation of the magnetic moments.

$$M = (M_{irr} + M_{rev}) \tag{I.40}$$

The irreversible contribution M_{irr} results from the movement of the domain walls which is impeded by the presence of pining sites [69]. A local energy dissipation occurs as the domain walls pin and unpin during their motion. The increase of energy dissipation during the magnetization process is characterized by the energy density E_{pin} given by equation (I.41) where k represents a microstructural parameter proportional to the density of the pinning sites.

$$E_{pin}(M) = k \int_0^M dM \tag{I.41}$$

When the material is magnetized, the corresponding energy density is given by the following equation:

$$\int_0^M M\, dB_e = \int_0^M M_a\, dB_e - k \int_0^M \left(\frac{dM}{dB_e}\right) dB_e \tag{I.42}$$

$$B_e = \mu_0 H_e \tag{I.43}$$

$$H_e = H + \alpha M \tag{I.44}$$

where B_e represents the effective magnetic flux density and H_e the effective magnetic field, and $k \int_0^M \left(\frac{dM}{dB_e}\right) dB_e$ represents the energy dissipated during the domain wall motion. α represents the interdomain coupling parameter.

The differentiation of (I.42) with respect to B_e gives the expression of the irreversible magnetization (I.45).

$$\frac{dM_{irr}}{dH} = \frac{M_{an} - M_{irr}}{\frac{\ell k}{\mu_0} - \alpha(M_{an} - M_{irr})} \tag{I.45}$$

where ℓ is a parameter related to the magnetic field evolution such that:

- $\ell = 1$ if $\frac{dH}{dt} > 0$
- $\ell = -1$ if $\frac{dH}{dt} < 0$

M_{an} is the anhysteretic magnetization, in the original Jiles-Atherton model, the Langevin function is used to describe this behavior, where M_s is the saturation magnetization and $\mathfrak{L}$ the Langevin function.

$$M_{an} = M_s \mathfrak{L}\left(\frac{H_e}{a}\right) = M_s \left(\coth\left(\frac{H_e}{a}\right) - \frac{a}{H_e}\right) \tag{I.46}$$

The reversible magnetization is associated to the reversible deformation of magnetic wall domain when a magnetic field is applied, it is given by (I.47), where c_r represents the reversibility coefficient $c \in [0\ 1]$.

$$M_{rev} = c_r(M_{an} - M_{irr}) \tag{I.47}$$

The differentiation of the total magnetization (I.40) which is the sum of the reversible (I.47) and the irreversible magnetization (I.45) with respect to H gives the expression (I.48).

$$\frac{dM}{dH} = \frac{(1 - c_r)\frac{dM_{irr}}{dH_e} + c_r \frac{dM_{an}}{dH_e}}{1 - \alpha c_r \frac{dM_{an}}{dH_e} - \alpha(1 - c_r)\frac{dM_{irr}}{dH_e}} \tag{I.48}$$

The expressions of $\frac{dM_{irr}}{dH_e}$ and $\frac{dM_{an}}{dH_e}$ are given respectively in (I.49) and (I.50)

$$\frac{dM_{irr}}{dH_e} = \frac{M_{an} - M_{irr}}{\ell k} \tag{I.49}$$

$$\frac{dM_{an}}{dH_e} = \frac{M_s}{a}\left[1 - \coth^2\left(\frac{H_e}{a}\right) + \left(\frac{a}{H_e}\right)\right] \tag{I.50}$$

The Jiles-Atherton model can be also adapted to have $M(B)$. The total magnetization is differentiated with respect to B given in (I.51) and we obtain:

$$\frac{dM}{dB} = \frac{(1 - c_r)\frac{dM_{irr}}{dB_e} + c_r \frac{dM_{an}}{dB_e}}{1 + \mu_0(1 - c_r)(1 - \alpha)\frac{dM_{irr}}{dB_e} + \mu_0 c_r(1 - \alpha)\frac{dM_{irr}}{dB_e}} \tag{I.51}$$

$$\text{with } \frac{dM_{irr}}{dB_e} = \frac{M_{an} - M_{irr}}{\mu_0 \ell k} \tag{I.52}$$

The model parameters M_s, α, a, k et c_r are determined from experimental measurements.

- ***Magneto-elastic coupling***

To take into account the effect of elastic mechanical loading, Jiles and Sablik added a term to the effective magnetic field H_e. Assuming an isotropic material, and a uniaxial stress applied in the direction of the magnetic field, its expression is given as follows:

$$H_e = \frac{1}{\mu_0}\left(\frac{\partial A}{\partial M}\right)_T \tag{I.53}$$

$$\text{with} \quad A = G + \mu_0 HM \tag{I.54}$$

$$\text{and} \quad G = U - TS + \left(\frac{3}{2}\right)\sigma\lambda \tag{I.55}$$

where A the Helmholtz free energy, G represents the Gibbs free energy, $U = \frac{1}{2}\alpha\mu_0 M^2$ represents the internal energy due to the magnetization, S the entropy, σ the applied mechanical stress and λ the magnetostriction function. The final expression of the effective field is given by (I.56).

$$H_e = H + \alpha M + H_\sigma \tag{I.56}$$

$$H_\sigma = \frac{3}{2}\frac{\sigma}{\mu_0}\left(\frac{\partial \lambda}{\partial M}\right)_T \tag{I.57}$$

where H_σ is the magneto-elastic field, it represents the magnetic contribution to the total effective magnetic field H_e due to the application of an external elastic stress σ.

- ***Magneto-plastic coupling***

To take into account the magneto-plastic coupling Sablik, proposed an extension to the Jiles magneto-elastic model [70]. It is based on the consideration that the parameters a and k, which are constants in the original Jiles-Atherton model, are now dependent on the dislocation density ξ. The dislocation density is the main characteristic of plastic deformation, it depends on the applied hardening stress σ_F , the shear modulus G, the Burger vector b and the dislocation density prior to plastic deformation ξ_{d0} which is related to the material composition.

$$\xi_d = \left(\left[\frac{\sigma_F}{\alpha_K G b}\right] + \xi_{d0}\right)^2 \tag{I.58}$$

This magneto-plastic modeling approach based on the dislocation density will be used in this thesis to model the impact of the mechanical cutting process on the magnetic properties of FeSi sheets. In the next chapter more details about the improvements made to this model and the used identification technique will be presented.

❖ **Hirsinger's model**

This model was proposed by Hirsinger *et al* [71] and, in the same way as in the Jiles-Sablik model, it is based on the "effective field" approach. Instead of a Langevin function, this model proposes an arc-tangent function to model the anhysteretic magnetization as given by equation (I.59)

$$M_{an} = \frac{2M_s}{\pi} \operatorname{atan}\left(\frac{\pi}{2}\chi_a(\sigma)\frac{H}{M_s}\right) \tag{I.59}$$

$$\chi_a{}^{-1}(\sigma) = \chi_{a0}{}^{-1} + A.\sigma \tag{I.60}$$

where χ_{a0}, A et M_s are the model parameters.

I.4.3 Magneto-mechanical formulas

This type of modelling approach uses mathematical formulas to represent the effect of mechanical stress on magnetic properties without any phenomenological or physical basis. Such models are usually employed to represent the degradation of magnetic behavior at the cutting edges of ferromagnetic materials due to the forming processes. Overall, they express the magnetic flux density, magnetization, or permeability as a function of magnetic field and the distance x from the edge. This section presents some mathematical expressions.

An hyperbolic formula (I.61) has been proposed in [72] where the magnetization M is given as a function of the cutting edge distance x. Fig I.35 gives a schematic of steel sheet punched at the edge. The magnetization M (equation I.61) is function of the parameters M_0, M_1 and D that themselves depend on the magnetic field H. The variable x is the distance from x_0 associated to the half the sample width.

$$M(x) = M_0 - M_1 \cosh\left(D\frac{x}{x_0}\right) \tag{I.61}$$

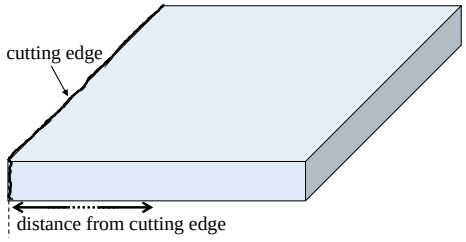

Fig I.35 illustration of a cut steel sheet

Another analytical formula (equation I.62) has been proposed in [73] to express the dependency of reluctivity υ on the uniaxial stress.

$$\upsilon(B^2,\sigma) = \upsilon(B^2,0) + a\sigma \exp\left(\frac{(B^2-(b-c\sigma)^2)^2}{d-e\sigma}\right) \tag{I.62}$$

where a, b, c, d and e are constants estimated from measured BH curves under different stresses. B is the magnetic flux-density and σ the mechanical stress applied in the direction parallel to B.

The main advantage of these formulas is their simple and easy implementation in numerical calculation tools, which is inexpensive in terms of calculation time. For example, a modeling of the flux density distribution of a stator considering the cutting effect using an empirical formula has been used presented in [74-76].
However, these models also lack the ability to predict behavior under magneto-mechanical loadings other than those employed for their identification.

I.5 Conclusion

In this chapter we have presented the theoretical background necessary to understand the subject of this thesis. The Weiss magnetic domain theory as well as the typical physical quantities of interest for the magneto-mechanical coupling have been defined and explained.

The manufacturing effect on magnetic properties have been reviewed, we focused on the impact of mechanical cutting on the magnetic properties of electrical steels. It has been shown that magnetic permeability and iron losses are strongly affected, depending on the material composition, the grain size, and the cutting process parameters the iron loss increase vary between 20% and 40%.

The theoretical study of magneto-mechanical coupling allowed to understand the mechanisms by which mechanical loads affect the magnetic properties of materials. A distinction is made between magneto-elastic coupling which is related to the phenomenon of magnetostriction and magneto-plastic coupling which is characterized by the increase of the dislocation density as the plastic deformation increases, which considerably affects the magnetic properties.

The reviewed magneto-mechanical models were classified into three categories: macroscopic models, microscopic models and mathematical approaches. According to the final aim of the modeling, each model has advantages and disadvantages. The multi-scale approach is interesting for modeling magneto-elastic multiaxial phenomena. The mathematical approaches, which are not based on physical considerations, are limited to the materials used for the identification of the model. However, because of its easy implementation in a numerical calculation tool, it can be interesting as a first approach to illustrate the effect of magnetic properties degradation on industrial electromagnetic systems such as rotating electrical machines.

In this thesis, the Sablik model has been chosen to model the mechanical punching effect on the anhysteretic magnetic behavior of electrical steels used for magnetic circuits in electrical machines. The model will be integrated into a finite element method calculation code to analyze the overall impact on electrical machine performances.
Compared to the analytical models, the Sablik model presents the advantage to have a physical basis which allows its generalization. Also, the use of macroscopic quantities makes its identification as well as its implementation and computational cost in numerical tools relatively acceptable. Typically, this model does not require complex measurements for its identification and

its impact on the numerical computation time is relatively limited. In the context of the present thesis, some modifications have been realized in this model; they are presented in the next chapter.

Chapter II

Magneto-mechanical modeling

In this chapter, the magneto-mechanical model considered to take into account the effect of punching process on magnetic properties of ferromagnetic materials is discussed. First the original magneto-plastic model proposed by Sablik and its theoretical background is presented. Secondly, the proposed modifications to the model are detailed, it concerns the introduction of a new modeling method of the anhysteretic and magnetostrictive behaviors, and the introduction of an equivalent stress to take into account the multiaxial stress effect. Finally, the identification methodology has been presented in detail.

II.1 Magneto-plastic model – Sablik's approach

II.1.1 Sablik model

As explained in the previous chapter, section I.4.2, to take into account the plastic deformation effect in the magnetoelastic Jiles-Atherton model, Sablik rewrites the parameters a (equation I.46) and k (equation I.49) as a function of the dislocation density.

Since the parameter k is related to the pinning sites density, it is proportional to the coercivity and hence has the same dependence. Based on the experimental works [77-80] which show that coercivity is proportional to the square root of the dislocation density, Sablik in [70][81][82] proposes the expression of the wall pinning parameter k given by (II.1).

$$k = \left[G_1 + \frac{G_2}{d}\right] k_0 {\xi_d}^{\frac{1}{2}} \tag{II.1}$$

Regarding the scaling parameter a, this latter is proportional to the domain density in the demagnetized state, which is determined by the pinning site density, which is in turn proportional to the pinning parameter k. Thus, Sablik proposes the expression (II.2) of the scaling parameter a where it exhibits the same dependence as k on the dislocation density ξ_d.

$$a = \left[G_3 + \frac{G_4}{d}\right] a_0 {\xi_d}^{\frac{1}{2}} \tag{II.2}$$

with G_1, G_2, G_3 and G_4 are constants related to the grain size d, a_0 and k_0 are respectively the wall pinning and scaling parameters prior to plastic deformation. The dislocation density ξ_d is expressed as:

$$\xi_d = \left(\left[\frac{\sigma_F}{0.76\, Gb}\right] + \xi_{d0}\right)^2 \tag{II.3}$$

where ξ_{d0} is the initial dislocation density prior to the plastic deformation, G is the specimen shear modulus as given by (II.4), b is the appropriate Burgers vector magnitude for the specimen's dislocations, υ is the Poisson ratio and Y is the Young modulus.

$$G = \frac{Y}{2(1+\upsilon)} \tag{II.4}$$

The plastic deformation ε which is represented by the hardening stress σ_F is directly related to the dislocation density ξ_d as expressed in (II.3). The hardening stress as illustrated in Fig.II.1 is given by $\sigma_F = \sigma - \sigma_y$ where σ_y represents the yield stress and, σ the applied stress modeled by the Hollomon law such as $\sigma(\varepsilon) = k_F \varepsilon^{n_F}$, where k_F is the hardening coefficient and n_F the exponent.

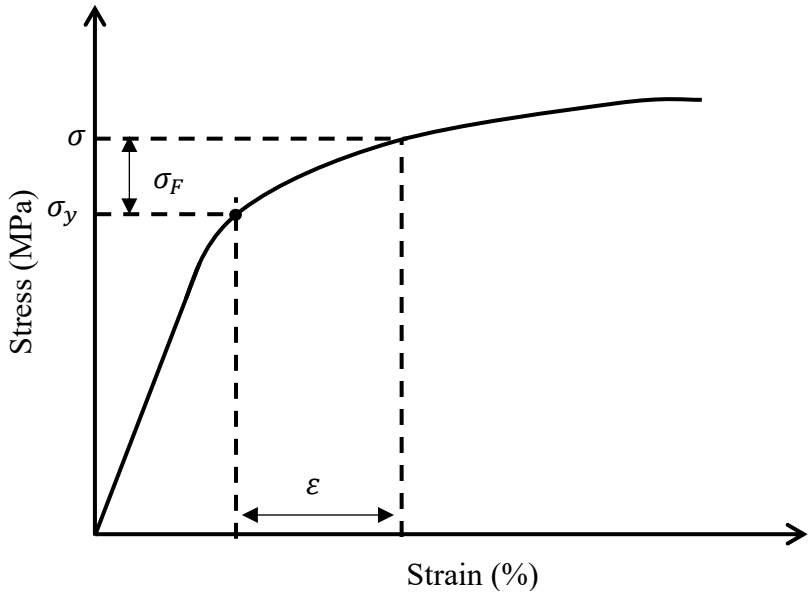

Fig.II.1 Illustration of the hardening stress

In the following we will only consider the anhysteretic behavior. Thus, the magneto-mechanical model is expressed by equation (I.46) which gives the anhysteretic magnetization M_{an} as a function of the scaling parameter a (II.2), the effective field H_e (I.56), and the magneto-mechanical field H_σ (I.57) which is related to the magnetostriction function λ. Its expression will be discussed in more details in this section.

II.1.2 Anhysteretic functions

An accurate representation of the magneto-mechanical behavior also relies on the ability of the magnetic model, in our case the anhysteretic function, to reproduce the observed experimental behavior. In that context, most of the magnetic models exploit the Langevin function for description of the anhysteretic magnetic behavior. Although it exhibits interesting advantages, limited number of parameter and physical behavior, the Langevin function can lead to accuracy problems, especially when employed for hysteresis modeling [83][84]. In this section two anhysteretic functions based on the Brillouin function, which were developed to model the anhysteretic behavior, are presented and adapted for the magneto-mechanical modeling.

The Brillouin function expressed in (II.5) was originally developed for the quantum physics, with J the internal quantum number varying from $J = 1/2$ to $J \longrightarrow \infty$. It reduces to the Langevin function in the limit $J \longrightarrow \infty$ and for $J = 1/2$ it reduces to the hyperbolic function.

$$B_J(x) = \left(\frac{2J+1}{2J}\right)\coth\left(\frac{2J+1}{2J}x\right) - \frac{1}{2J}\coth\left(\frac{1}{2J}x\right) \quad \text{(II.5)}$$

Figure II.2 gives Brillouin function for different values of J .

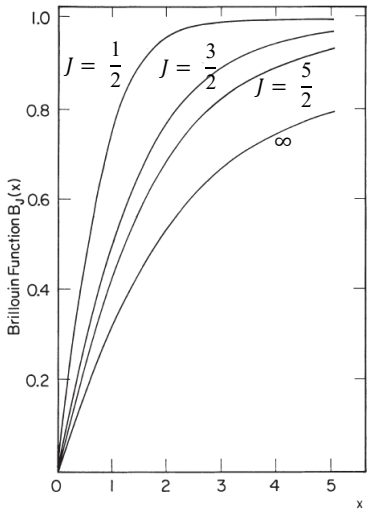

Fig II.2 Brillouin function for various values of J [3]

The Brillouin function was originally derived for paramagnet materials, where the magnetic moments are assumed oriented in random direction without interaction in the absence of an external magnetic field. However, like the Langevin function used in the Sablik model, it can be used for ferromagnet by considering the effective field. In [85], the author proposes, based on the Brillouin model, an anhysteretic function that is a linear combination of two Langevin functions. Its expression is given in (II.6) where, on the one hand, M_{s_1} and M_{s_2} are parameters related to the saturation magnetization such as $M_s = M_{s_1} + M_{s_2}$ and, on the other hand, a_1 and a_2 are the scaling parameters.

$$M_{an} = M_{s_1}\left(\coth\left(\frac{H_e}{a_1}\right) - \frac{a_1}{H_e}\right) + M_{s_1}\left(\coth\left(\frac{H_e}{a_2}\right) - \frac{a_2}{H_e}\right) \quad \text{(II.6)}$$

Another approach to represent the anhysteretic function, called the “modified Brillouin function”, has been proposed by Wlodarski [86]. It consists of a double Langevin function with the introduction of an additional hyperbolic tangent term, its expression is given in (II.7).

$$M_{an} = M_{s_1}\left(\coth\left(\frac{H_e}{a_1}\right) - \frac{a_1}{H_e}\right) + M_{s_2}\tanh\left(\frac{|H_e|}{a_2}\right)\left(\coth\left(\frac{H_e}{a_2}\right) - \frac{a_2}{H_e}\right) \quad \text{(II.7)}$$

where M_{s_1}, M_{s_2}, a_1, a_2 are the model parameters and have the same definition as in the double Langevin function (II.6).

In their original configuration, H_e in (II.6) and (II.7) refers to the effective magnetic field, where only the magnetic behavior is modeled. In the present work, based on the Sablik model, we propose to adapt the anhysteretic function to the magneto-mechanical modeling by introducing the effective field H_e as expressed in (I.56) and write the parameters a_1 and a_2 as a function of the plastic strain.

II.1.3 Magnetostriction model

In this study, the magnetostriction λ refers to the magnetostrictive deformation along the magnetization direction. As reported in chapter I, it has been observed experimentally that λ is an even function of the magnetization, which means that the deformation due to the magnetization is independent of its direction. Furthermore, the magnetostriction has an asymmetrical and nonlinear dependency on the tensile and compressive stress [87]. Since the scientific community began to be interested in magnetostrictive behavior under mechanical loading, different models have been proposed.

Through their several works on the magnetoelastic behavior modeling, Jiles and Sablik used different magnetostriction functions. In [88], a magnetostriction model, which depends on the magnetization and the elastic stress, has been proposed. The function λ given in (II.8) is expressed in term of the saturation magnetostriction λ_s that depends on the elastic stress and the square of magnetization M^2.

$$\lambda = \frac{3}{2}\lambda_s(\sigma)\left(\frac{M}{M_s}\right)^2 \tag{II.8}$$

$$\text{With } \lambda_s = \begin{cases} \left(\lambda_{s_0} - \lambda_{s_t}\right)\left(1 - \left({}^{\sigma}/_{\sigma_t}\right)^{1/2}\right) + \lambda_{s_t} & \sigma \geq 0 \\ \left(\lambda_{s_0} - \lambda_{s_c}\right)\left(1 - \left({}^{\sigma}/_{\sigma_c}\right)^{1/2}\right) + \lambda_{s_c} & \sigma \leq 0 \end{cases} \tag{II.9}$$

$\lambda_{s_0}, \lambda_{s_t}$and λ_{s_c} are the maximum value of magnetostriction in the unload state, under maximum tension σ_t and under maximum compression, respectively. However, the magnetostriction function represented in (II.8) and (II.9) does not respect an asymmetrical dependency on the stress. Indeed, this model always predicts improvement of the magnetic permeability for the tensile stress and degradation for compressive stress.

Another more elaborated magnetostriction function has been proposed in [89] [90]. It is derived from magnetoelastic considerations by considering the mechanical equilibrium state of the material. The magnetostriction is function of the mechanical parameters υ and Y that are the Poisson ratio and Young modulus, respectively. E_{mag} refers to the magnetic energy and C_e is a constant.

$$\lambda = -\left(\frac{2}{3}\frac{C_e(1+\upsilon)}{Y}\right)\left[\left\{1 + \left(\frac{9Y}{2{C_e}^2(1+\upsilon)^2}\right)E_{mag}(M_s)\right\}^{\frac{1}{2}} - \left\{1 + \left(\frac{9Y}{2{C_e}^2(1+\upsilon)^2}\right)\left[E_{mag}(M_s) - E_{mag}(M)\right]\right\}^{\frac{1}{2}}\right] \tag{II.10}$$

Compared to the function proposed in (II.8), this model is able to reproduce the asymmetrical magnetostrictive behavior with respect to the compressive and the tensile stresses. However, its identification is not straightforward.

Recently, based on experimental observations, a mathematical model of the magnetostriction has been proposed by Deepak *et al* [91]. The proposed model consists in the product of two distinct functions as given in (II.11).

$$\lambda = \left(\sum_{j=1}^{p} \beta_j M^{2j}\right)\left(C_1 + \tanh\left(\frac{\sigma - \sigma_0}{\tau}\right)\right) C_2 \tag{II.11}$$

The first function reproduces the evolution of the magnetostriction in terms of the magnetization and, as for the models presented above, it considers a $2p$ degree polynomial dependency on the magnetization. The second function scales the magnetostriction depending on the stress, using the hyperbolic tangent which is controlled by the parameters C_1, C_2, τ, σ_0.

The authors showed that the function presents a good agreement with magnetostriction measurements under different elastic stresses. The nonlinear dependency on the compressive and tensile stresses, which was the weakness of the previous models, is well respected. Within the context of this work, this function will be integrated in the original Sablik model.

II.1.4 Equivalent stress approach

The main limitation of Sablik model is that the effect of stress on the magnetic behavior is restricted to uniaxial stress. Yet, stress is multiaxial in most of industrial applications. To overcome this limitation, an equivalent stress is the adaptative solution in the case of the scalar modeling approach used in the Sablik model. In this section, a brief review of the different definitions of "equivalent stress" proposed in the literature will be introduced, then the equivalent stress proposed by Hubert and Daniel [92] will be presented in more details.

An equivalent stress σ_{eq} from the magnetic point of view is a fictive uniaxial stress that would change the magnetic behavior in a similar way to the real multiaxial stress tensor $\boldsymbol{\sigma}$ given in (II.12):

$$\boldsymbol{\sigma} = \begin{bmatrix} \sigma_{xx} & \sigma_{xy} & \sigma_{xz} \\ \sigma_{yx} & \sigma_{yy} & \sigma_{yz} \\ \sigma_{zx} & \sigma_{zy} & \sigma_{zz} \end{bmatrix} \tag{II.12}$$

Based on experimental observations of materials submitted to biaxial stress, Kashiwaya [93] proposed the equivalent stress given in (II.13):

$$\sigma_{eq} = K(\sigma_{xx} - \sigma_{max}) \tag{II.13}$$

with K a constant, σ_{xx} the stress aligned with the magnetic field direction as illustrated in Fig. II.3 and σ_{max} the maximal value of the stress tensor $\boldsymbol{\sigma}$. From (II.13), the equivalent stress is always negative or null and if the magnetic field is applied along the direction of the maximum stress, the equivalent stress is zero, so that a tensile stress or an equi-biaxial tension or compression are supposed to have no effect on the magnetic behavior. This approach does not represent the observed physical behavior.

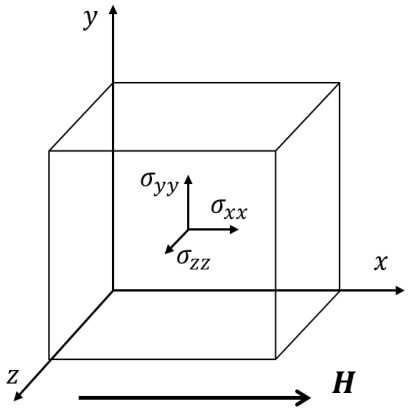

Fig II.3 Multiaxial stress illustration

Another approach has been proposed by Schneider and Richardson [94], the equivalent stress is expressed by (II.14):

$$\sigma_{eq} = \left(\sigma_{xx} - \sigma_{yy}\right) \tag{II.14}$$

where σ_{xx} and σ_{yy} are the stresses in the plane, the magnetic field being aligned in the direction of σ_{xx}. The main difference with Kashiwaya's equivalent stress is that the area of the stress plane where $\sigma_{xx} > 0$ and $\sigma_{yy} < 0$ defines a positive equivalent stress. However, an equibiaxial stress is still supposed to have no effect on the magnetic behaviour.

Sablik *et al*, [95] proposed the following definition of the equivalent stress, based on magneto-mechanical measurements:

$$\begin{cases} \sigma_{eq} = \frac{1}{3}\left(2\sigma_{xx} - \sigma_{yy}\right) & \text{if } \sigma_{xx} < 0 \\ \sigma_{eq} = \frac{1}{3}\left(\sigma_{xx} - \sigma_{yy}\right) & \text{if } \sigma_{xx} > 0 \end{cases} \tag{II.15}$$

where σ_{xx} is the stress aligned with the magnetic field. This approach presents a significant difference with the previous one, tensile and compression biaxial stress do not lead to the same result, however this model is discontinuous when σ_{xx} changes sign.

II.1.4.1 Daniel and Hubert (D-H) equivalent stress

All the previous proposals for an equivalent stress are restricted to biaxial stress and the magnetic field is necessarily applied along an eigendirection of the stress tensor. Daniel and Hubert (D-H) proposed a definition of a more general equivalent stress which is based on an equivalence in magnetoelastic energy [92][96][97]. The magnetoelastic energy W_σ over a volume V is given in (II.16).

$$W_\sigma = -\boldsymbol{\sigma}: \boldsymbol{\varepsilon_\lambda} \tag{II.16}$$

$$\boldsymbol{\varepsilon_\lambda} = \begin{bmatrix} \lambda & 0 & 0 \\ 0 & -\frac{1}{2}\lambda & 0 \\ 0 & 0 & -\frac{1}{2}\lambda \end{bmatrix} \tag{II.17}$$

where $\boldsymbol{\sigma}$ and $\boldsymbol{\varepsilon_\lambda}$ are the macroscopic stress and magnetostriction strain tensors, respectively. $\boldsymbol{\varepsilon_\lambda}$ is written for an isotropic material and the magnetostriction is assumed to be isovolumetric which means that the volume magnetostriction is neglected, so that the the trace of $\boldsymbol{\varepsilon_\lambda}$ is equal to zero. The magnetostriction λ and the magnetic field are measured in the direction x. Thus, the magnetoelastic energy can be developed as given in (II.18):

$$W_\sigma = -\lambda\left[\sigma_{xx} - \frac{1}{2}\left(\sigma_{yy} + \sigma_{zz}\right)\right] = -\lambda\left[\frac{3}{2}\sigma_{xx} - \frac{1}{2}\mathrm{tr}(\boldsymbol{\sigma})\right] \tag{II.18}$$

The term $\mathrm{tr}(\boldsymbol{\sigma})$ represents the trace of the stress tensor $\boldsymbol{\sigma}$. In order to get a definition independent from the chosen coordinate system, the stress component in the direction of the magnetic field σ_{xx} is given by (II.19):

$$\sigma_{xx} = \boldsymbol{h^t \sigma\, h} \tag{II.19}$$

where $\boldsymbol{h}$ denotes the direction of the applied field and $\boldsymbol{h^t}$ the transpose of $\boldsymbol{h}$. Thus, the expression for the magnetoelastic energy is finally written, for any stress tensor $\boldsymbol{\sigma}$, as expressed in (II.20):

$$W_\sigma = -\lambda\left[\frac{3}{2}\boldsymbol{h^t \sigma\, h} - \frac{1}{2}\mathrm{tr}(\boldsymbol{\sigma})\right] \tag{II.20}$$

Now, by considering a uniaxial stress σ_u applied in the direction parallel to the magnetic field, leads to the magnetoelastic energy given in (II.22):

$$\boldsymbol{\sigma} = \begin{bmatrix} \sigma_u & 0 & 0 \\ 0 & 0 & 0 \\ 0 & 0 & 0 \end{bmatrix} \tag{II.21}$$

$$W_\sigma = -\lambda[\sigma_u] \tag{II.22}$$

Assuming that the same magnetoelastic energy leads to the same magnetic behavior, equations (II.20) and (II.22) are considered equivalent. The following expression for the equivalent stress σ_{eq} is finally obtained:

$$\sigma_{eq} = \frac{3}{2}\boldsymbol{h^t \sigma\, h} - \frac{1}{2}tr(\boldsymbol{\sigma}) \tag{II.23}$$

This definition of the equivalent stress is used to take into account the effect of a multiaxial stress on the magnetostriction behavior in the Sablik model. Thus, the uniaxial stress σ in (I.57) and (II.11) is replaced by the equivalent stress σ_{eq} defined in (II.23).

II.1.4.2 Validation of the D-H equivalent stress

As illustrated in Fig II.4, D-H equivalent stress definition states that a material under multiaxial stress (Fig II.3-a) exhibits the same magnetic behavior as a material submitted to this equivalent stress aligned with the magnetic field (Fig II.3-b).

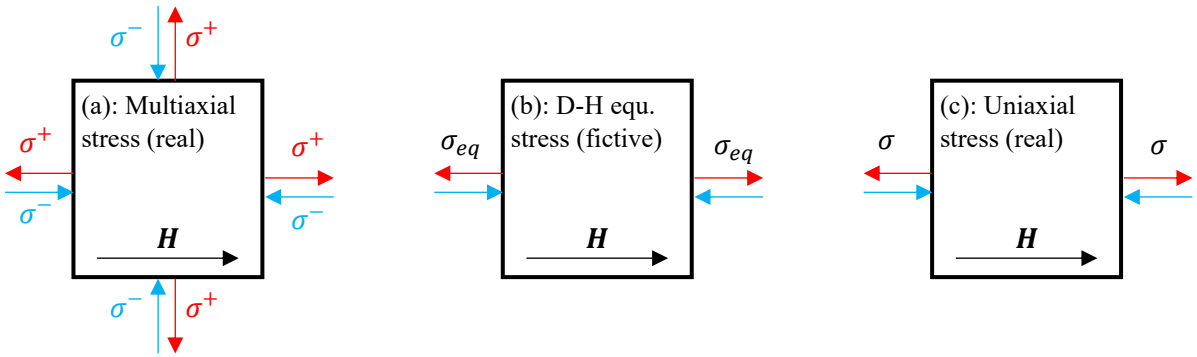

Fig. II.4 Illustration of bi-axial and equivalent stress configurations

The proposed validation is based on the comparison of measured anhysteretic magnetization curves under different biaxial and uniaxial stresses. The measurements were performed on a M400-50A non-oriented electrical steel sheet by using a custom-made single sheet tester device. The detail of the measurement setup and experimental procedure can be found in [56]. The validation process follows two steps:

- First, using equation (II.23) the D-H equivalent stress is calculated for each biaxial stress, with the magnetic field aligned along x direction. Table II.1 gives the applied stresses $[\sigma_{xx}\ \sigma_{yy}\ \sigma_{zz}]$ and their corresponding D-H equivalent stress. The three colors distinguish between uniaxial (blue), equi-biaxial (orange) and shear-biaxial (green) stresses. We note that in the case of a uniaxial stress applied in the direction of the magnetic field, the equivalent stress is obviously the applied stress.

Tab. II.1 Calculation of the D-H equivalent stress

$[\sigma_{xx}\ \sigma_{yy}\ \sigma_{zz}]$ (MPa)	D-H σ_{eq} (MPa)	$[\sigma_{xx}\ \sigma_{yy}\ \sigma_{zz}]$ (MPa)	D-H σ_{eq} (MPa)	$[\sigma_{xx}\ \sigma_{yy}\ \sigma_{zz}]$ (MPa)	D-H σ_{eq} (MPa)
[-30 0 0]	-30	[-30 -30 0]	-15	[-30 +30 0]	-45
[-20 0 0]	-20	[-20 -20 0]	-10	[-20 +20 0]	-30
[-10 0 0]	-10	[-10 -10 0]	-5	[-10 +10 0]	-15
[+10 0 0]	+10	[+10 +10 0]	+5	[+10 -10 0]	+15
[+20 0 0]	+20	[+20 +20 0]	+10	[+20 -20 0]	+30
[+30 0 0]	+30	[+30 +30 0]	+15	[+30 -30 0]	+45

- Second, the magnetization curves measured under biaxial stresses are compared to the ones obtained under uniaxial stress for the same magnitudes of the equivalent (from bi-axial) and real uni-axial stresses. For example, the magnetization curve measured under the shear-biaxial [-20 +20 0] which has a D-H equivalent stress $\sigma_{eq} = -30$MPa is compared to the one measured under the uniaxial $\sigma = -30$MPa.

Figure II.5 gives the comparison of the magnetization curves measured under the fictive uniaxial stress given by the D-H equivalent stress and their corresponding real uniaxial stress. It shows that the magnetization curves measured under the fictive uniaxial stress exhibits the same magnetization curves as those measured under the real uniaxial stress.

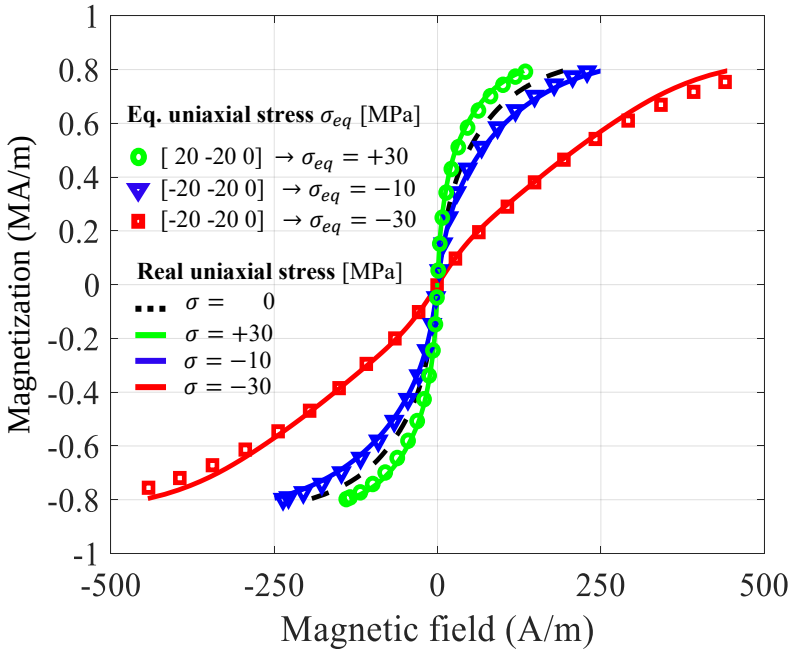

Fig. II.5 Magnetization curves measured under (a) equivalent stress (b) real uniaxial stress

II.1.5 Summary

In this section, the original Sablik approach for the magneto-plastic modeling has been presented. Some modifications are proposed to have a better representation of the experimental behavior. The original model uses the Langevin function (I.46) to describe the anhysteretic curve. We will investigate the ability of the double Langevin (II.6) and modified Brillouin (II.7) functions to better model the anhysteretic behavior. Also, we propose to use a more appropriate magnetostriction function which best expresses its dependence on the magnetization and stress. Then the D-H equivalent stress, which considers the multiaxial mechanical loading, is introduced to account for the magneto-elastic behavior. Finally, the expression of the magneto-elastic field given in (I.57) is written as follows:

$$H_\sigma = \frac{3}{2}\frac{\sigma_{eq}}{\mu_0}\left(\frac{\partial\lambda(M_{an},\sigma_{eq})}{\partial M_{an}}\right)_T \tag{II.24}$$

where σ_{eq} is the D-H equivalent stress given in (II.23) and $\lambda(M_{an}, \sigma_{eq})$ is the magnetostriction function given in (II.11) and expressed as follows:

$$\lambda = \left(\sum_{j=1}^{p} \beta_j {M_{an}}^{2j}\right)\left(C_1 + \tanh\left(\frac{\sigma_{eq} - \sigma_0}{\tau}\right)\right)C_2 \quad \text{(II.25)}$$

There is no modification in the plastic dependent parameters, whatever the considered anhysteretic function Langevin, double Langevin or modified Brillouin, the parameters a, a_1 or a_2 are expressed in terms of the dislocation density, therefore in terms of the plastic strain ε.

II.2 Model identification

The parameters of the anhysteretic Sablik model are identified using magnetization curves measured under different elastic stresses and plastic strains. Two groups of measured magnetization curves have been used:

- The first group is performed by M. El Youssef [49] from L2EP laboratory. The NO electrical steel sheet (1.3%) Si-Fe M330-35A grade has been investigated, where the magnetization curves are measured under different elastic uniaxial stresses, and under different plastics strains. The measured data are used to identify the whole Sablik model.
- The second group carried out by U. Aydin [56] from Aalto University considers a NO electrical steel sheet (3%) Si-Fe M400-50A grade. The magnetization curves are measured under different elastic biaxial stresses. The measured data have been used previously to validate the D-H equivalent stress approach from the magnetic point of view.

As presented in section II.1.2, three functions can be used to model the anhysteretic behavior: the Langevin, double Langevin and modified Brillouin functions. In this section a comparison in terms of fitting accuracy is carried out between the three approaches. There are three distinct steps to follow during the identification of the Sablik model parameters. First, without considering the stress dependence, the initial parameters of the model are identified. Second, the elastic stress dependence is considered and the parameters of the magnetostriction function are identified. Finally, the plastic dependency is introduced, and its parameters identified.

Expressions of the magnetization in (I.46), (II.6) or (II.7) are implicit equations which require an iterative resolution. Fig. II.6 gives the flow chart of the Langevin function resolution, the method is also valid for the double Langevin and the modified Brillouin functions. To carry out the curve fitting in this study, the least square error between the model and the experiment was used as the objective function to be minimized.

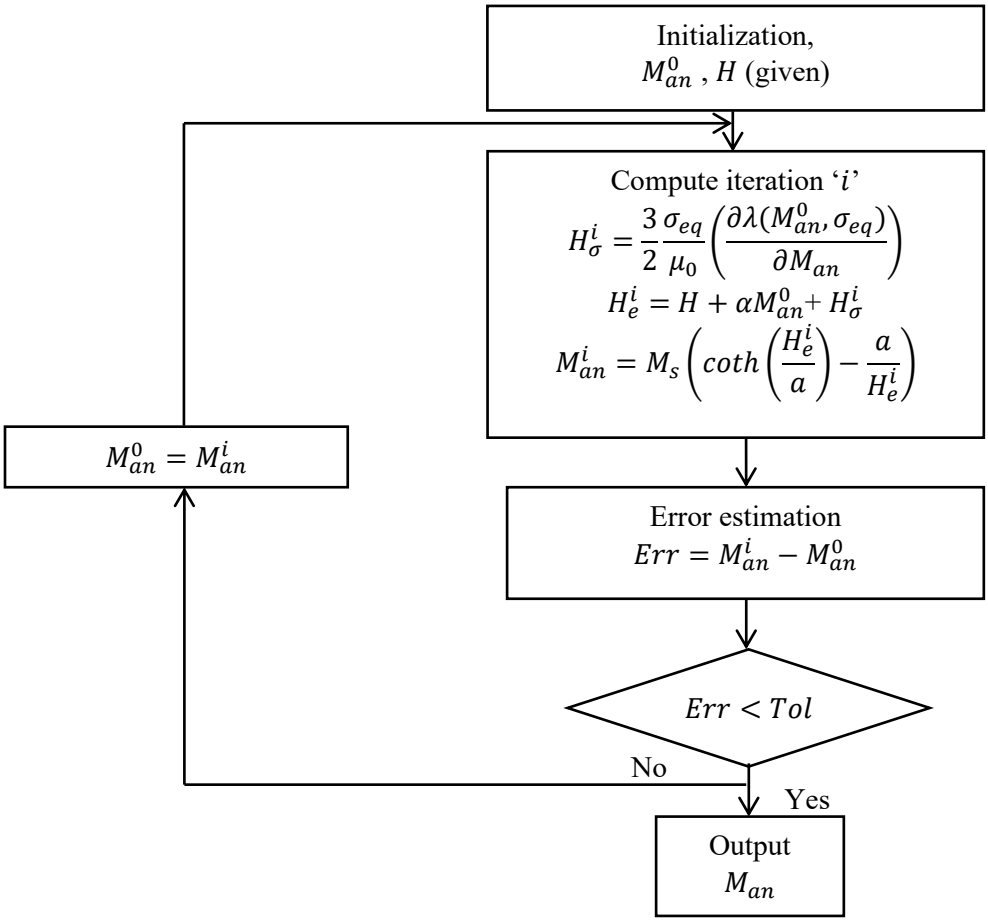

Fig. II.6 Flow chart for the solution method of the magneto-plastic model

II.2.1 Initial identification

Without considering the stress dependence in (II.24) ($H_\sigma = 0$), the initial parameters of the model are identified by fitting the global formula of magnetization curve measured for the grade M330-35A. According to the considered anhysteretic function, the model parameters are identified separately. For the Langevin function the magnetization model is given in (I.46) and the identified parameters are given in Tab. II.2.

Tab II.2 Initial parameters of the Langevin function for the grade M330-35A

Parameter	Value
M_s(A/m)	1.39×10^6
a_0(A/m)	120.86
α	4.10×10^{-5}

When the double Langevin function (II.6) and the modified Brillouin function (II.7) are used. The identified parameters are given in Tab. II.3

Tab. II.3 Initial parameters of the modified Brillouin function for the grade M330-35A

Parameter	Double Langevin	Modified Brillouin
M_{s_1}(A/m)	2.74×10^5	3.07×10^5
M_{s_2}(A/m)	1.31×10^6	1.21×10^6
a_{0_1}(A/m)	2436.7	1099.6
a_{0_2}(A/m)	97.36	76.24
α	8.78×10^{-6}	8.78×10^{-6}

The subscript '0' in a_0, a_{0_1}, a_{0_2} refers to the 'initial' values, i.e. without stress or strain. Figure II.7 gives the fitted and measured magnetization curves for the three anhysteretic functions.

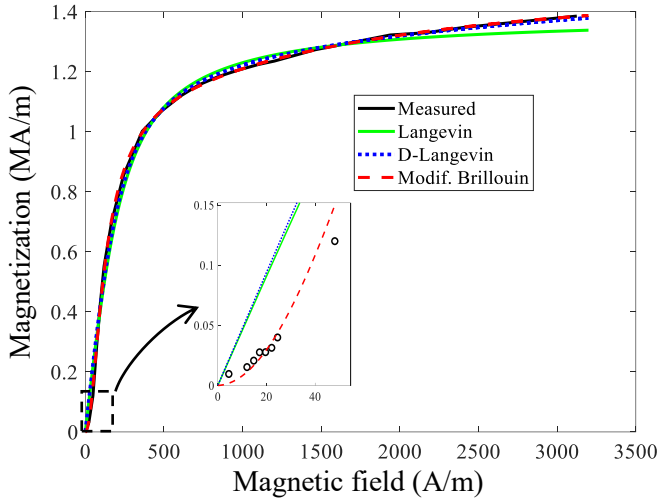

Fig. II.7 Modeled and measured magnetization curve without considering the stress effect for different anhysteretic functions for the grade M330-35A

The best fitting accuracy is obtained with the Brillouin function, as illustrated in Fig III.8, where the relative deviation for the different anhysteretic functions is plotted. Although, it shows a discrepancy for all at the beginning of the linear zone. The modified Brillion function presents the weakest fitting deviation at the linear and the saturation zones of the magnetization curve.

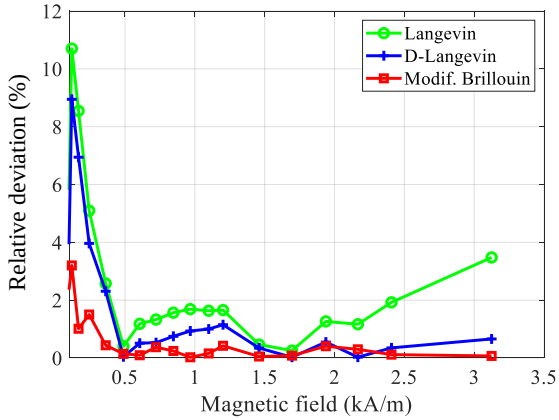

Fig II.8 Relative fitting deviation for the different anhysteretic functions

Even, the double Langevin function presents a weak fitting deviation at the saturation zone, it remained relatively high at the linear zone. Thus, for the next identification steps only the Langevin function used in the original Sablik model and the modified Brillouin function will be also investigated.

II.2.2 Elastic identification

This identification step keeps fixed the parameters previously determined and identify the parameters which depends on the elastic stress.

II.2.2.1 Elastic identification under uniaxial stress

The elastic stress dependence is considered in (II.24) where the magneto-mechanical field $H_\sigma \neq 0$, and the stress is given by the D-H equivalent stress. To carry out the identification, Langevin and modified Brillouin functions are considered. Thus, formulas (II.24) (II.25) and (I.57) are combined in (I.46) when Langevin function is considered and combined in (II.7) when the modified Brillouin function is considered, then the global expression of magnetization is fitted with the measured magnetization curves (grade M330-35A) for both approaches and the parameters of the magnetostriction function given in II.25 are identified.

The magnetostriction function λ is a product of two terms, a polynomial of degree $2p$ $\sum_{j=1}^{p} \beta_j {M_{an}}^{2j}$ and a tangent function $\left(C_1 + \tanh\left(\frac{\sigma_{eq}-\sigma_0}{\tau}\right)\right) C_2$ depending on the stress. The parameters of the magnetostriction model are β_j ($j = 1 \longrightarrow p$), C_1, C_2, σ_0 and τ.

- **Langevin function**

When the anhysteretic behavior is expressed using the Langevin function, the global magnetization given in (I.46) is fitted with magnetization curves measured under different uniaxial tensile and compressive elastic stresses. As seen in the initial identification step the Langevin function presents a fit inaccuracy at the beginning of the linear zone and the saturation zone which makes the convergence of the iterative process described in Fig II.5 difficult, thus the degree of the polynomial function in (II.25) is set to 2 (*i.e.* p=1).

The fitting result is given in Fig. II.9, the modeled curves reproduce the global behavior of the measured magnetization curves under elastic stress.

Up to a certain elastic stress value $\sigma = 16.7$ MPa the magnetization exhibits an improvement compared to the unloaded case; besides this value the degradation of magnetization curves starts.

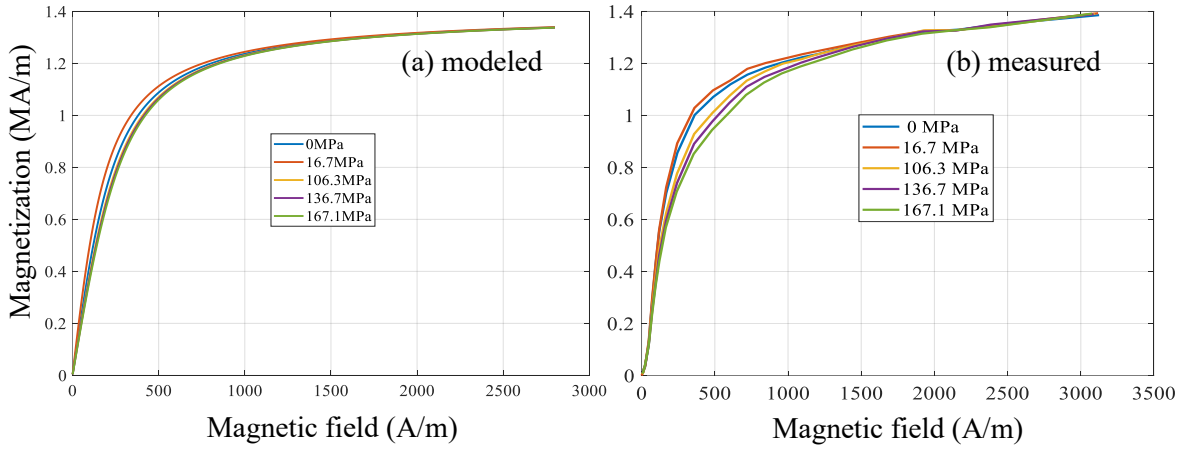

Fig II.9 Measured and fitted magnetization curves under different stress levels using the Langevin function for the grade M330-35A

The magnetization curve fitting presented in Fig II.9 leads to the magnetostriction model parameters given in Tab. II.4.

Tab. II.4 Fitted magnetostriction parameters using the Langevin function for the grade M330-35A

Parameter	Value	Parameter	Value
β_1	-1,13×10^{-18}	σ_0(MPa)	8.29
C_1	-0.94	τ(MPa)	24.54
C_2	1.46	-	-

Figure II.10 gives the identified magnetostriction function for different stress levels. Compared to measured magnetostriction under elastic stress presented in [91], it shows a good agreement. The nonlinear dependence on the compressive and tensile stress is well modeled. However, the convergence by setting the degree of the polynomial term $p = 1$ prevent to reach the magnetostriction at saturation.

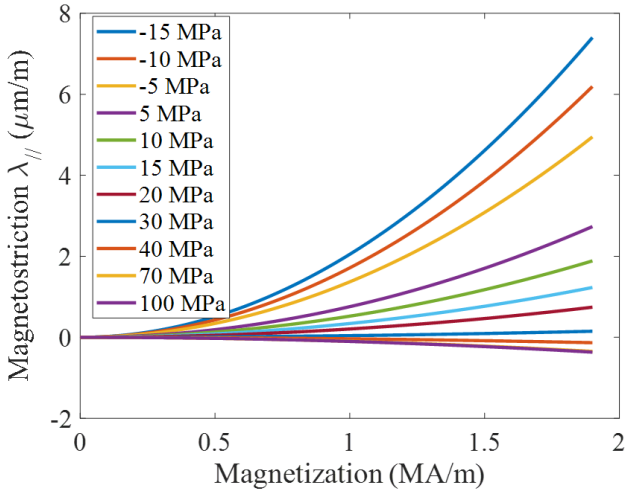

Fig. II.10 Stress dependency of the magnetostriction model - Langevin function for the grade M330-35A

- **Modified Brillouin function**

By considering the modified Brillouin function, the global magnetization is given by (II.14). It is fitted with measured magnetization curves under different elastic stress levels. In that case, it was possible to improve the accuracy of the fitting by setting the degree of the magnetostriction polynomial term to $p = 5$ as recommended in [91]. Figure II.11 gives the fitting results. As for the Langevin function, the modeled curves reproduce the global behavior of the measured magnetization curves under elastic stress, moreover the quality of fitting is better. Fig II.12 gives the comparison of relative fitting deviation obtained with both anhysteretic function.

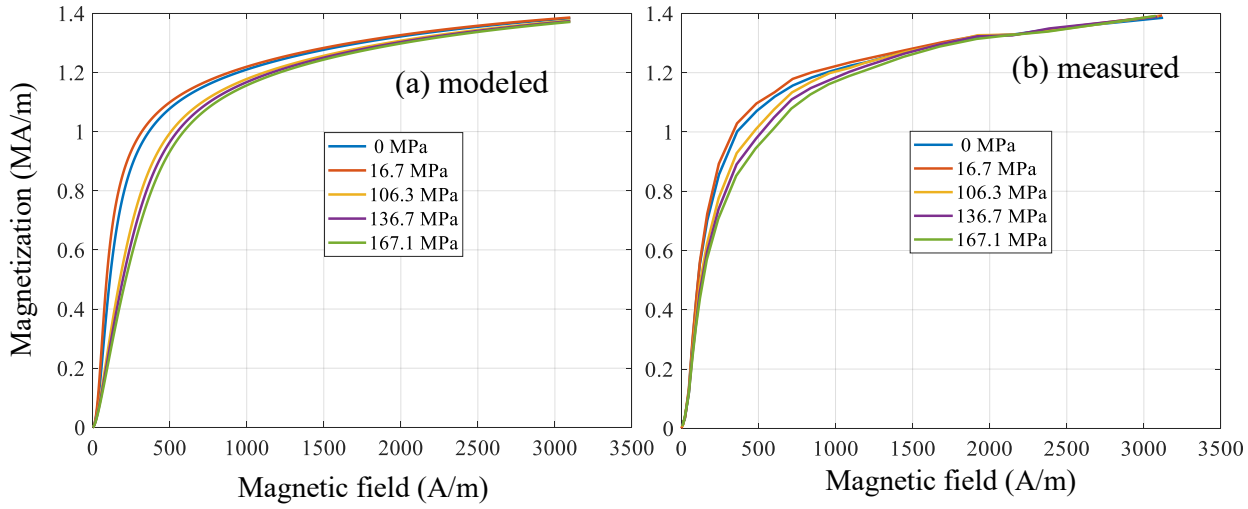

Fig. II.11 Measured and fitted magnetization curves under different stress levels using the modified Brillouin function for the grade M330-35A

Figure II.12 shows that the modified Brillouin function presents only about 4% fitting deviation in the linear and almost nil at the saturation zone, while the Langevin function reach about 23% fitting deviation in the linear zone and 4% in the saturation zone.

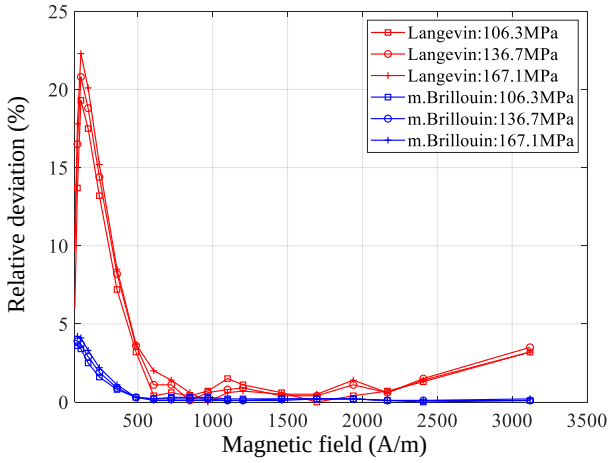

Fig II.12 Comparison between the relative fitting deviation obtained with Langevin function and the modified Brillouin function

The magnetization curve fitting presented in Fig II.11 leads to the identification of the magnetostriction model parameters given in Tab. II.5.

Tab. II.5 Fitted magnetostriction parameters using the m. Brillouin function for the grade M330-35A

Parameter	Value	Parameter	Value
β_1	8.36×10^{-19}	C_1	2.43
β_2	2.96×10^{-31}	C_2	1.88
β_3	-2.50×10^{-43}	σ_0(MPa)	9.36
β_4	1.19×10^{-55}	τ(MPa)	-22.85
β_5	-2.42×10^{-68}	-	-

The modeled magnetostriction function for different stress levels is given in Fig. II.13. The use of the modified Brillouin function to model the anhysteretic magnetization allowed to obtain better results in terms of magnetization curves and consequently a more realistic magnetostrictive behavior. The non-uniform dependency on the compressive and the tensile applied stress of λ is represented, furthermore the magnetostriction at saturation is reached.

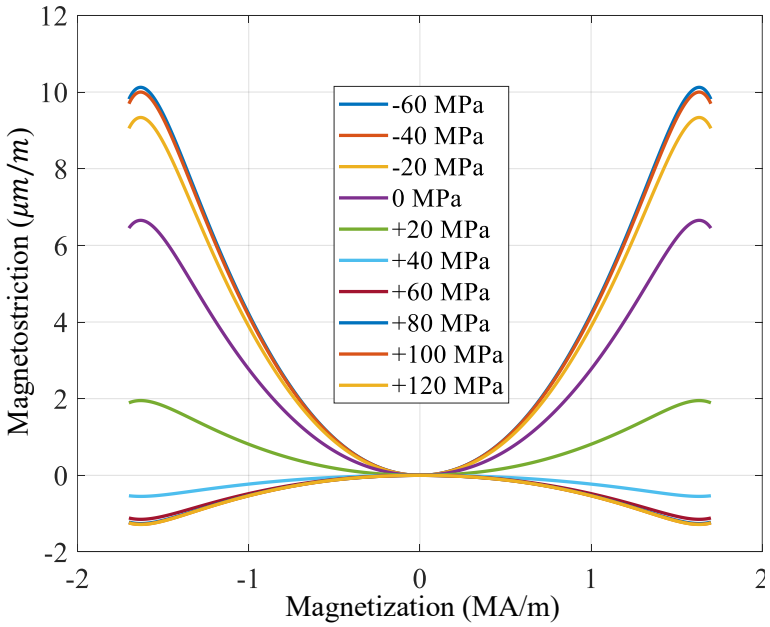

Fig. II.13 Stress dependency of the magnetostriction model using the modified Brillouin function for the grade M330-35A

II.2.2.2 Elastic identification under biaxial stress

The aim of this identification under biaxial stresses is to validate the D-H equivalent stress approach from the magnetostrictive behavior point of view using the measurements carried out on the material grade M400-50A. From Tab. II.1, first the measured magnetization curves under compressive and tensile equivalent stresses σ_{eq} = -30 MPa, -20 MPa, -15 MPa, 0 MPa, 30 MPa

are selected, which correspond, respectively to the biaxial stresses (in MPa) $[\sigma_{xx}\ \sigma_{yy}\ 0] = [-20\ +20\ 0]$, [-20 0 0], [-10 +10 0], [0 0 0], [+20 -20 0]. Then, as in the uniaxial case, the parameters of the magnetostriction model are identified. The global anhysteretic magnetization is described using the Langevin function (I.46) and the modified Brillouin function (II.7).

The measured magnetization curves used in this subsection are different from those used in the initial identification section. Therefore, the initial parameters for both Langevin function and the modified Brillouin function are identified again using the magnetization curve measured without stress. they are given in Tab. II.6

Tab II.6 Initial parameters of the Langevin and the modified Brillouin functions for the grade M400-50A

Langevin	Value	m. Brillouin	Value
$M_s(\mathrm{A/m})$	1.12×10^{6}	$M_{s1}(\mathrm{A/m})$	8.46×10^{5}
$a(\mathrm{A/m})$	112.40	$M_{s2}(\mathrm{A/m})$	1.28×10^{5}
α	2.51×10^{-4}	α	6.76×10^{-5}
-	-	$a_{0_1}(\mathrm{A/m})$	51.06
-	-	$a_{0_2}(\mathrm{A/m})$	11.05

The fitted parameters of the magnetostriction model are given in Tab. II.7. The degree of the polynomial term of the magnetostriction model is set $p = 5$ with both anhysteretic functions.

Tab. II.7 Fitted magnetostriction parameters – D-H equivalent stress approach for the grade M400-50A

Parameter	Value	Parameter	Langevin	m. Brillouin
β_1	6.05×10^{-19}	C_1	-3.95	-4.81
β_2	2.14×10^{-31}	C_2	3.37	4.17
β_3	-1.81×10^{-43}	σ_0(MPa)	39.20	48.56
β_4	8.61×10^{-55}	τ(MPa)	32.82	-14.41
β_5	-1.75×10^{-68}	-	-	

The modeled magnetization curves using the Langevin and the modified Brillouin functions (solid and dashed line respectively) and measured magnetization curves (dotted line) for different equivalent stresses are given in Fig. II.14. The modeled curves show the same fit accuracy with both anhysteretic functions. Indeed, the used magnetization curves are measured in an interval of magnetic flux density [-1,1] T which makes the shape of the magnetization curve suitable for fit with both anhysteretic functions.

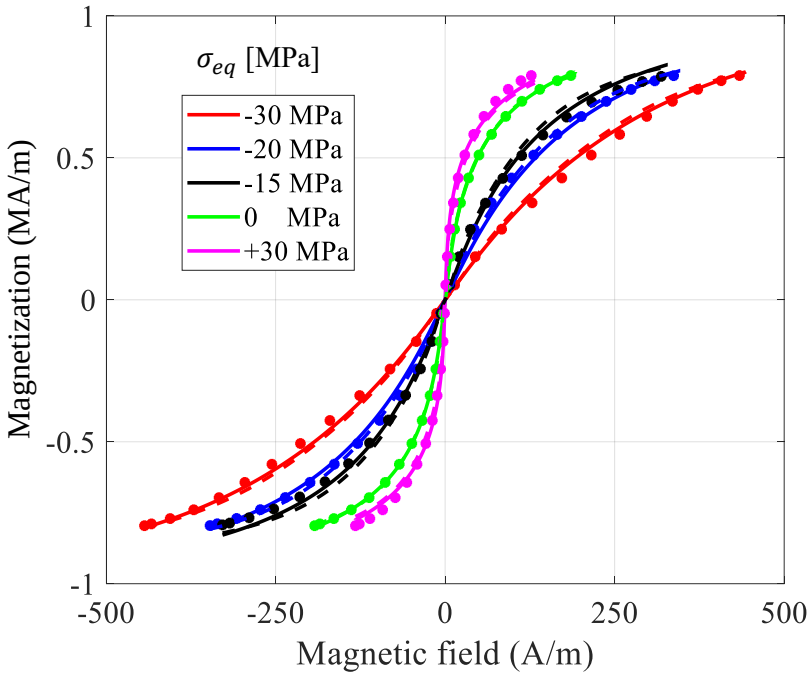

Fig. II.14 Modeled magnetization (solid line: Langevin, doted line: m. Brillouin) and measured magnetization (dashed line) under different equivalent stresses. for the grade M400-50A

Figure II.15 gives the modeled stress dependence of the magnetostriction function by considering the D-H equivalent stress approach to define the multiaxial and the Langevin function or the modified Brillouin function to model the anhysteretic magnetization. The global behavior with respect to the magnetization and elastic stress is respected, the difference in the magnitude of saturation magnetostriction is since the magnetization curves used to identify the parameters are measured on two different electrical steels with different measurement setups.

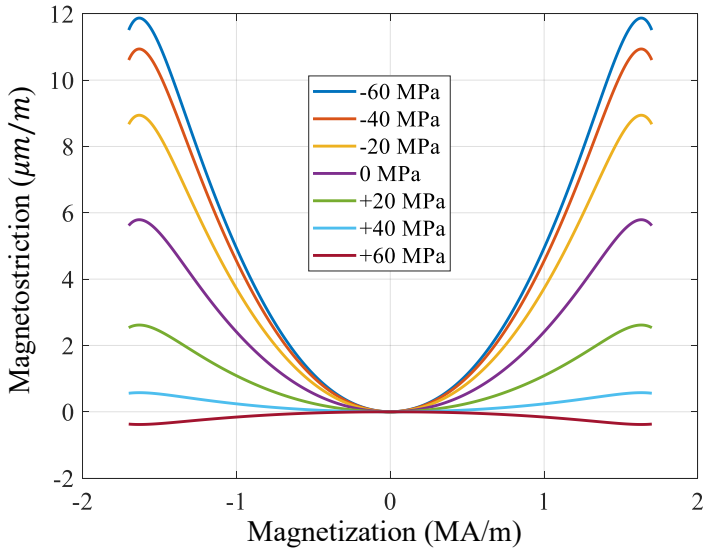

Fig. II.15 Stress dependency of the magnetostriction model – D-H equivalent stress approach for the grade M400-50A

II.2.3 Plastic identification

In this last step of the identification process, the parameters identified previously for the initial (without stress) and elastic configurations are kept fixed. Then, the dependence of the model on the plastic strain is introduced and the parameters of the dislocation density are identified. As in the previous identification steps, the use of the Langevin function and modified Brillouin function to define the anhysteretic magnetization are compared. The magnetization curves used to identify the model parameters are those measured for the material grade M330-35A, they have been used in the initial and the elastic uniaxial identification. Thus, If the anhysteretic magnetization is expressed by the Langevin function, the initial and the elastic parameters of the model are given in Tab. II.2 and Tab. II.4, respectively. In the case of an anhysteretic magnetization expressed using the modified Brillouin function the initial and elastic parameters are given in Tab. II.3 and Tab. II.5, respectively.

- **Conditions of the plastic identification**

To perform the plastic identification, the parameter a is now function of the dislocation density (II.2), and consequently function of the plastic strain through the relation of the hardening stress $\sigma_F(\varepsilon) = k_F \varepsilon^{n_F} - \sigma_y$. However, the evolution of the elastic parameters in the presence of the plastic strain has not been explicitly defined in the original Sablik model. Indeed, it was shown in [98] that the magnetostriction evolves for a small plastic strain (0.01%), therefore during the plastic identification the magneto-elastic quantities, H_σ (II.24) and the magnetostriction function λ (II.25) will depend on the plastic applied stress $\sigma = k_F \varepsilon^{n_F}$.

To estimate the dislocation density ξ_d, the following measured parameters are considered: The Young modulus $Y = 174$ GPa, the Poisson ratio $\upsilon = 0.3$, the Hollomon law parameters, $k_F = 701.8$ MPa and $n_F = 0.23$ [49]. The Burgers vector $b = 10{\times}10^{-10}$ m is the typical value given in [77][78].

Table II.7 gives the fitted parameters of the dislocation density ξ_{d0}, d, G_3, G_4 when the anhysteretic magnetization is modeled with the Langevin function.

Tab. II.7 Fitted dislocation density parameters using the Langevin function for the grade M330-35A

Parameter	Value
ξ_{d0} (m^{-2})	$0.55{\times}10^{12}$
G_3(m)	10^{-6}
G_4 (m^{-2})	$1.07{\times}10^{-11}$
d(m)	$30{\times}10^{-6}$

Figure II.16 gives the modeled and measured magnetic flux density curves under different plastic strains when the anhysteretic behavior is modeled with the Langevin function.

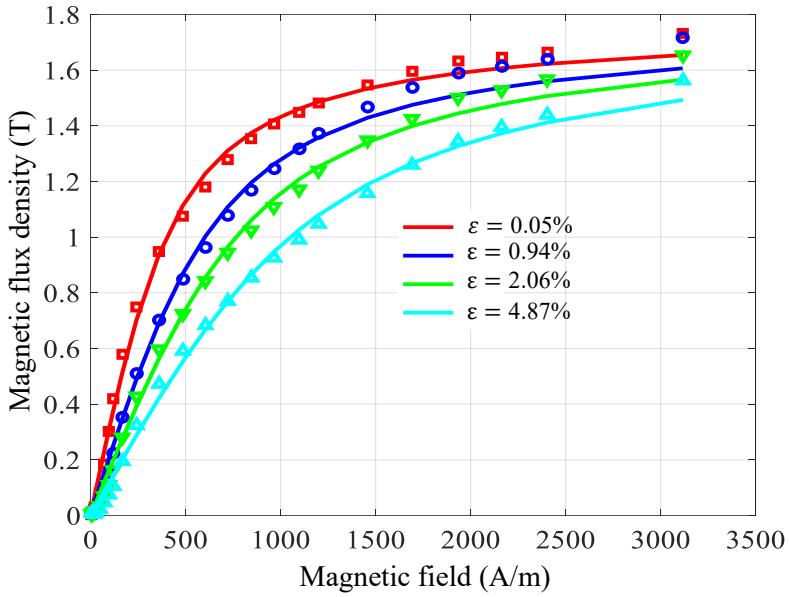

Fig. II.16 Measured (dotted line) and modeled (solid line) magnetic flux density curves for different values of plastic strain – Langevin function for the grade M330-35A

We know from experimental measurement that the dislocation density, as shown in Fig. II.17-a, is proportional to the square of the hardening stress $\sigma_F{}^2$ and the scaling parameter a as illustrated in Fig. II.17-b is expected to be proportional to square root of the plastic strain $\sqrt{\varepsilon}$ [77].

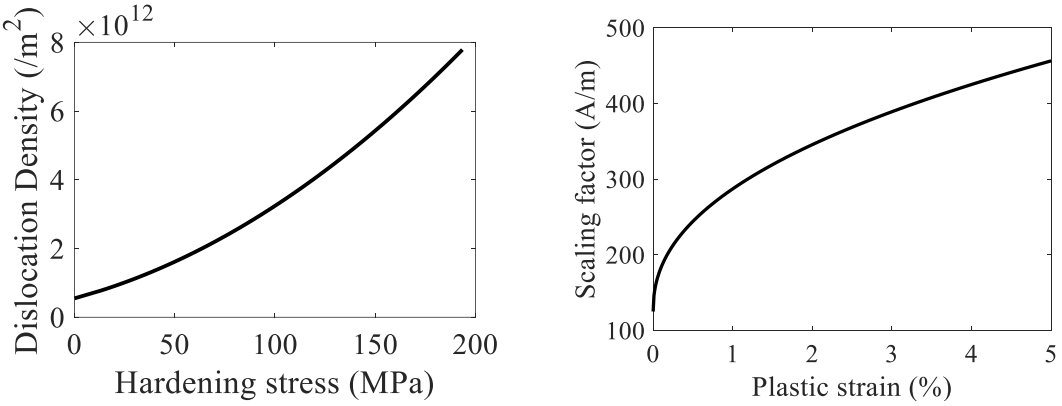

Fig. II.17 (a) Evolution of the dislocation density with respect to the hardening stress (b) Evolution of the fitted scaling factor with respect to plastic strain for the grade M330-35A

Since the behavior of the scaling parameter a with respect to the plastic strain ε has been verified and confirmed by various works [99][100], we propose the following simple expression:

$$a = a_0 a_p \tag{II.26}$$

where a_0 represents the initial scaling parameter (without stress), while a_p is a factor that depends on the plastic strain, its expression is given by the function (II.27). d_1, d_2, d_3 and r are the model coefficients.

$$a_p = d_1\varepsilon^r + d_2\varepsilon + d_3 \tag{II.27}$$

The proposed expression of the scaling parameter given by (II.26) is now considered in the Langevin function. Then, the plastic identification process is performed. First the parameter a_p is identified by fitting the Sablik model with the measured magnetization curves for different plastic strains, then its evolution is fitted with the expression (II.27). Tab. II.8 gives the fitted coefficients.

Tab. II.7 Fitted a_p coefficients

Parameter	Value
d_1	1.005
d_2	0.299
d_3	1.00
r	0.215

Figure II.18 gives the evolution of the scaling parameter a given by the proposed expression (II.26), it shows the same behavior as the one shown in Fig. II.17-b obtained by considering the original expression of the scaling parameter given by (II.2). Thus, the use of (II.26) allowed to directly account for the plastic strain in the Sablik model. Furthermore, it avoids the identification of the dislocation density parameters.

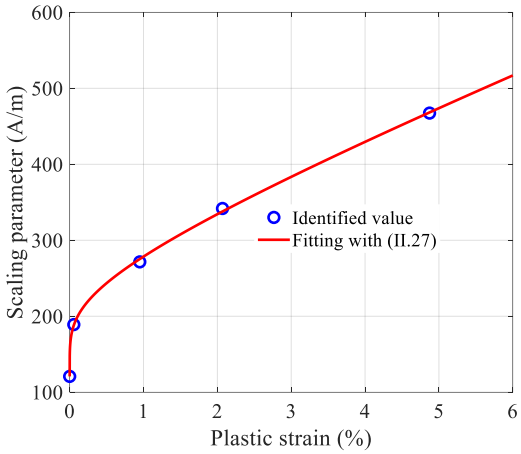

Fig. II.18 Evolution of the fitted scaling parameter a with respect to plastic strain

For the modified Brillouin function (II.7), the proposed formula (II.26) is used to express the plastic behavior. Thus, the expressions of a_1 and a_2 are givens as follows:

$$a_1 = a_{0_1} a_{p_1} \tag{II.28}$$

$$a_2 = a_{0_2} a_{p_2} \tag{II.29}$$

The same identification procedure as for a has been followed to identify a_1 and a_2 .

Figure II.19 gives the modeled and measured magnetic flux density curves under different plastic strains when the anhysteretic behavior is modeled with the modified Brillouin function.

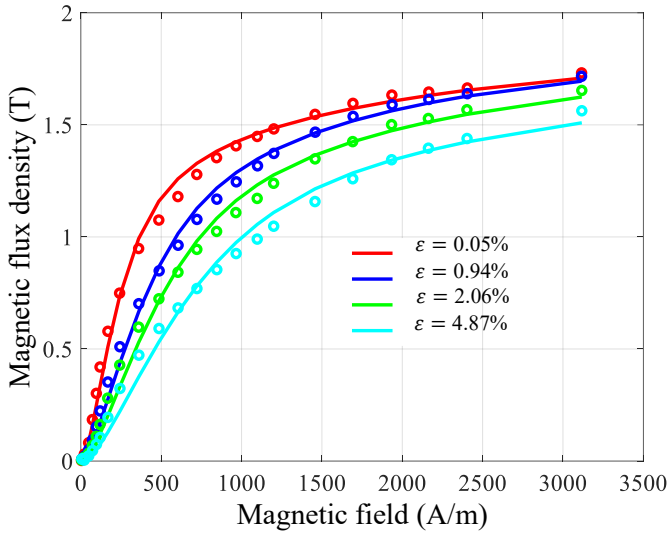

Fig. II.19 Measured (circle line) and modeled (solid line) magnetic flux density curves for different values of plastic strain using the modified Brillouin function for the grade M330-35A

Tab. II.8 gives the fitted coefficients of the scaling parameters a_{p_1} and a_{p_2}

Tab. II.8 Fitted coefficients of a_{p_1} and a_{p_2}

Parameter	a_{p_1}	a_{p_2}
d_1	-329.5	0.798
d_2	0.3904	0.225
d_3	330.1	1.00
r	5.622×10^{-4}	0.305

The evolution of the parameters a_1 and a_2 with respect to the plastic strain are given in Fig. II.20-a and Fig. II.20-b, respectively. a_2 exhibits the same behavior as a in the Langevin function, while a_1 shows a different evolution with respect to the plastic strain.

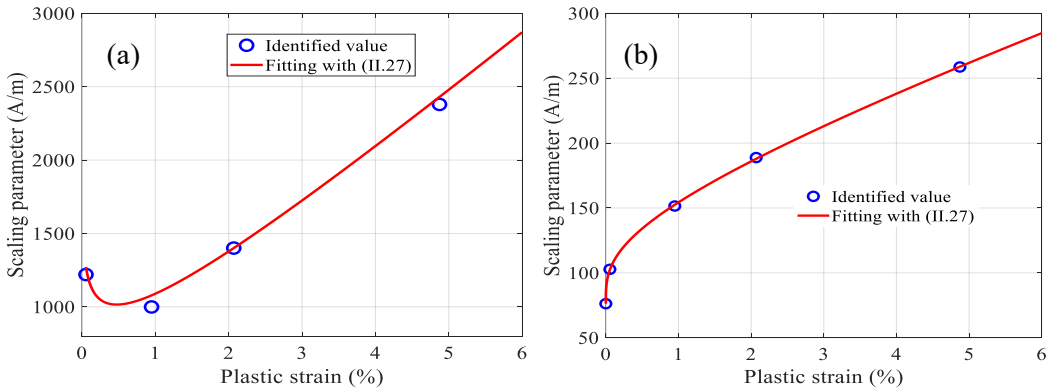

Fig. II.20 Evolution of the fitted scaling parameters a_1 and a_2 with respect to the plastic strain

Figure II.21 gives the relative fitting deviation obtained with the Langevin function and modified Brillouin function.

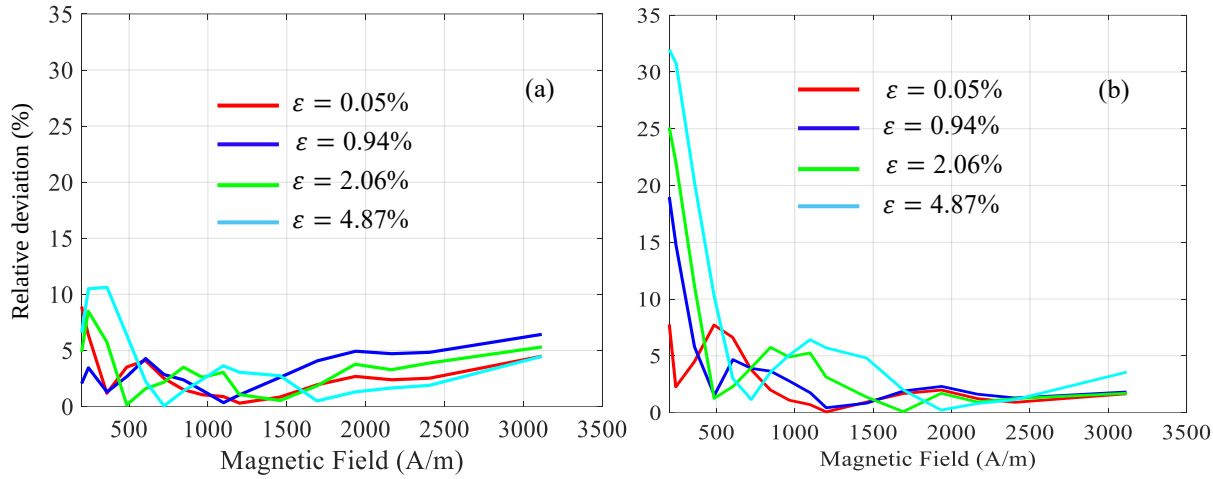

Fig. II.21 Relative fitting deviation of the magnetization curves (a) Langevin function (b) modified Brillouin function

The result shows that the introduction of the modified Brillouin function allowed to improve the fitting accuracy at the saturation zone (Fig II.21-b). However, at the linear and knee zones the fitting deviation is relatively important than when the Langevin function is used.

Finally, to simulate the effect of mechanical punching process, the considered Sablik model is expressed as follows:

- Although the modified Brillouin function improved the magnetostrictive identification in the elastic part of the model, compared to the Langevin function, its plastic identification did not show an important improvement of fitting accuracy, except at the saturation zone. Thus, the Langevin function given by (I.46) will be considered to investigate the magneto-mechanical coupling in the following chapters. The initial and the magnetostriction parameters are given in Tab. II.2 and Tab. II.4, respectively.
- The scaling parameter a is given by (II.26), its corresponding coefficients are given in Tab II.7. The original relation of a could have been used, however (II.26) is more suitable since it accounts directly for the plastic strain.
- The mechanical quantities (plastic strain ε and the stress σ_{eq}) of the Sablik model are scalar values.

II.3 Discussions and conclusion

In this chapter an approach based on the Sablik model for the magneto-mechanical modeling has been presented.

The first modification made to the original Sablik model concerns the introduction of the D-H equivalent stress. This approach based on an equivalence in the magnetoelastic energy induced by

the real multiaxial stress and the defined fictive uniaxial stress (σ_{eq}) has been validated. In section II.1.4.2 different magnetization curves measured under multiaxial stress and their corresponding real uniaxial equivalent stress were compared. The result shows that the magnetization curves under real and fictive uniaxial stresses are close. However, it should be noted that they are measured under elastic stress which did not exceed +30 MPa in tensile and -30 MPa in compressive stress. The second test is carried out with the equivalent stress implemented in the Sablik model and the identified magnetostriction model. The result agrees with the expected magnetostrictive behavior.

The second modification concerns the introduction of the modified Brillouin function to model the anhysteretic magnetization instead of the Langevin function used in the original model. In section II.2.1, Fig. II.7 the comparison made between the anhysteretic functions in the unload state showed that the modified Brillouin function compared to the Langevin and double Langevin functions exhibits an accurate fitting for the whole range of the measured magnetization curve (linear, knee and saturation regions). This accuracy of the fitting allowed then to have a better modeling of the magnetostrictive behavior. However, when the plastic dependence is introduced the fitting accuracy of the modified Brillouin function seems less efficient in the linear and knee regions magnetization curve. Indeed, compared to the Langevin function, the use of the modified Brillouin function improves the accuracy fitting in the saturation zone and exhibits less accuracy in the linear and knee zones. This degradation of the accuracy can be explained by the shape of the magnetization curves. Under high plastic strains, the slope of the linear zone is strongly decreased, consequently the characteristic zones of the magnetization curve are not clearly delimited which makes the fitting with modified Brillouin function not as accurate as in the unloaded case. Nevertheless, it can also be a fitting problem. Therefore, the least square error used as the objective function to carry out the fitting process should be replaced.

Also, the stress dependent magnetostriction model presented in subsection II.1.3 was able to model the magnetostrictive behavior with respect to the magnetization and the asymmetrical variation with respect to stress. The identification method based only on macroscopic magnetization curves measured under compressive and tensile stress was quite simple and gives a good estimation of the magnetostriction.

Chapter III

Finite element implementation of the magneto-mechanical model

This chapter describes the modeling chain from the mechanical punching process till its effect on the magnetic properties. In addition to the description of the numerical models employed to simulate the magnetic and mechanical punching, we present the numerical tools that were developed to interface both physics through the magneto-mechanical behavior law described by the Sablik model that accounts for the plastic strain. The developments are illustrated through the analysis of academic example: a steel sheet sample.

III.1 Numerical tools

III.1.1 Maxwell equations for magnetostatics and behavior laws

Maxwell's equations are fundamental relations for the description of the electromagnetic phenomena. James Clerk Maxwell unified the known experimental laws: Gauss law, Faraday law and Ampere law. In this chapter, a nonlinear magnetostatic problem is represented in Fig. III.1, with different sources of magnetic field, such as a winding supplied by a current i, a permanent magnet modeled by a remanent magnetic flux density $\boldsymbol{B}_r$ and an imposed magnetic flux ϕ flowing through boundaries of the domain.

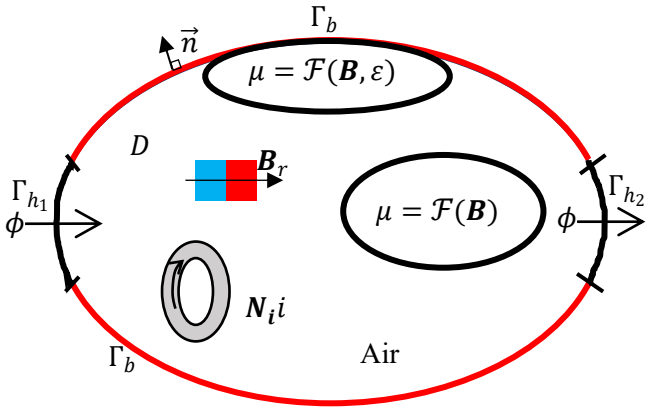

Fig III.1 Domain D and boundaries of the considered magnetostatic problem.

The magnetostatic problem, *i.e.* the electrical conductivity is neglected, in the domain D of boundary Γ is described by the following Maxwell equations.

$$\boldsymbol{curl}\, \boldsymbol{H} = \boldsymbol{N}_i\, i \tag{III.1}$$

$$div \boldsymbol{B} = 0 \tag{III.2}$$

with $\boldsymbol{H}$ [A/m] the magnetic field vector, $\boldsymbol{B}$ [T] the magnetic flux density vector and $\boldsymbol{N}_i\, i = \boldsymbol{J}_s$ [A/m^2] the source current density associated to the winding, where $\boldsymbol{N}_i$ is a vector that depends on the geometry of the winding, and which is proportional to the electrical current i. The vector $\boldsymbol{N}_i$ verifies:

$$div\, \boldsymbol{N}_i = 0 \text{ in } D_w \tag{III.3}$$

with D_w the subdomain corresponding to the winding. The solution of the above equations requires adding the magnetic behavior law (III.4), where the scalar function $\mathcal{F}$ links the $\boldsymbol{B}$ and $\boldsymbol{H}$ fields.

$$\boldsymbol{B} = \mathcal{F}(\boldsymbol{H}) \tag{III.4}$$

In this case, the function $\mathcal{F}$ corresponds to the magnetic permeability. Usually, the inverse of $\mathcal{F}$ might be required depending on the chosen formulation to solve the magnetostatic problem. Then, the inverse function $\mathcal{F}^{-1}$ representing the magnetic reluctivity is expressed as given by (III.5).

$$\boldsymbol{H} = \mathcal{F}^{-1}(\boldsymbol{B}) \tag{III.5}$$

III.1.2 Boundary conditions

The equations system composed of Maxwell's equations and the magnetic behavior law admit an infinity of solutions. Boundary conditions ensure its uniqueness.

$$\boldsymbol{H} \wedge \boldsymbol{n}|_{\Gamma_{h_1},\Gamma_{h_2}} = 0 \tag{III.6}$$

$$\boldsymbol{B}.\boldsymbol{n}|_{\Gamma_b} = 0 \tag{III.7}$$

$$\phi = -\iint_{\Gamma_{h_1}} \boldsymbol{B}\, d\boldsymbol{\Gamma} = \iint_{\Gamma_{h_2}} \boldsymbol{B}\, d\boldsymbol{\Gamma} \tag{III.8}$$

with $\Gamma_{h1} \cup \Gamma_{h2} \cup \Gamma_b = \Gamma$ and $\Gamma_{h1} \cap \Gamma_{h2} \cap \Gamma_b = 0$. The magnetic flux ϕ is imposed across the boundaries Γ_{h1} and Γ_{h2}. The boundary condition given in (III.6) imposes that the tangential component of the magnetic field $\boldsymbol{H}$ is equal to zero. In (III.7), the normal component of the magnetic flux density is equal to zero.

III.1.3 Vector potential formulation

Solving the above magnetostatic problem is carried out by considering the vector potential formulation. Thus, based on (III.2), the magnetic flux density $\boldsymbol{B}$ is expressed as a function of the vector potential $\boldsymbol{A}$ and of the imposed magnetic flux ϕ such that [101]:

$$\boldsymbol{B} = \boldsymbol{curl}\, \boldsymbol{A} + \boldsymbol{N}_\phi \phi - \boldsymbol{B}_r \qquad \text{with} \qquad \boldsymbol{A} \times \boldsymbol{n}|_{\Gamma_b} = 0 \tag{III.9}$$

with $\boldsymbol{N}_\phi$ a source field defined in the whole domain D, $\boldsymbol{B}_r$ the remanent magnetic flux density defined in a subdomain corresponding to the permanent magnets and verifying the following conditions:

$$div\, \boldsymbol{N}_\phi = 0 \qquad \text{in } D \tag{III.10}$$

with
$$\boldsymbol{N}_\phi.\boldsymbol{n}|_{\Gamma_b} = 0 \tag{III.11}$$

and
$$-\iint_{\Gamma_{h_1}} \boldsymbol{N}_\phi d\boldsymbol{s} = -\iint_{\Gamma_{h_2}} \boldsymbol{N}_\phi d\boldsymbol{s} = 1 \tag{III.12}$$

The magnetic behavior law (III.5) and the expression of $\boldsymbol{B}$ (III.9) are combined in the Maxwell Ampere equation (III.1). Then, the strong formulation to be solved is:

$$\boldsymbol{curl}\left(\mathcal{F}^{-1}\left(\boldsymbol{curl}\, \boldsymbol{A} + \boldsymbol{N}_\phi \phi - \boldsymbol{B}_r\right)\right) = \boldsymbol{N}_i\, i \tag{III.13}$$

III.1.4 Finite element method

For complex geometries, the vector potential formulation is solved by a numerical approach. The finite element method (FEM) is the most used. It is based on the transformation of partial differential equations into a system of algebraic equations. It was originally designed for the computation of mechanical structures [102], and then introduced in electromagnetism by Silver and Chari [103].

III.1.4.1 Finite element formulation

The strong formulation is not adapted for the finite element method. Indeed, the potential formulation must be developed under a weak form. To determine the weak formulation, the weighted residuals method is used, it consists in multiplying a residual R by a so-called weighting function and by integrating over the domain D [104][105]. Thus, based on the magnetostatic strong formulation given in (III.13), the residual $\boldsymbol{R}(\boldsymbol{A})$ is expressed as follows:

$$\boldsymbol{R}(\boldsymbol{A}) = \left[\boldsymbol{curl}\left(\mathcal{F}^{-1}\left(\boldsymbol{curl}\,\boldsymbol{A} + \boldsymbol{N}_\phi\phi - \boldsymbol{B}_r\right)\right) - \boldsymbol{N}_i\, i\right] \tag{III.14}$$

The weak formulation is obtained by multiplying the residual by weighting functions ψ and by integrating over the domain D:

$$\iiint_D \left[\boldsymbol{curl}\left(\mathcal{F}^{-1}\left(\boldsymbol{curl}\,\boldsymbol{A} + \boldsymbol{N}_\phi\phi - \boldsymbol{B}_r\right)\right) - \boldsymbol{N}_i\, i\right]\cdot \psi\, dD = 0 \tag{III.15}$$

The application of the Green theorem and the divergence theorem [106] and by considering the boundary conditions, the magnetostatic vector potential formulation in the integral form is given as follows:

$$\iiint_D \left(\mathcal{F}^{-1}\left(\boldsymbol{curl}\,\boldsymbol{A} + \boldsymbol{N}_\phi\phi - \boldsymbol{B}_r\right)\right)\cdot\left(\boldsymbol{curl}\,\psi\right) dD - \iiint_{D_w} \left(\boldsymbol{N}_i\, i\right).\psi\, dD = 0 \tag{III.16}$$

III.1.4.2 Discretization

The discretization by the FEM is originally based on the nodal elements, the introduction of the Whitney elements, which defines the edges and facets of elements, contributed greatly to the development of the method [107][108]. As illustrated in Fig. III.2, the spatial discretization of the domain D is carried out by elementary volumes D_e (tetrahedron, prisms or hexahedron in 3D), which consists of nodes, edges, facets, and volumes. We denote by n_n, n_e, n_f and n_v respectively the number of nodes, edges, facets, and volumes of the mesh.

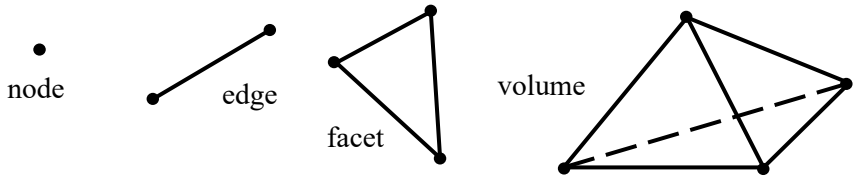

Fig. III.2 Examples of geometrical elements

III.1.4.3 Interpolation functions

An interpolation function is associated to each geometric entity: node, edge, facet, and volume.

- **Nodes**

A continuous scalar function w_n^0 is associated to each node n of the domain D. It is equal to 1 at the node n and 0 on all the others. The set of functions defines a finite dimensional space denoted W^0. If u is a scalar function defined in W^0, then it can be expressed as a linear combination of functions w_n^0, such as:

$$u = \boldsymbol{U}_n^t \boldsymbol{W}_n = \sum_{n=1}^{n_n} u_n \, w_n^0 \tag{III.17}$$

where $\boldsymbol{W}_n$ is the vector of the interpolation functions w_n^0 and $\boldsymbol{U}_n$ the vector of the coefficients u_n which corresponds to the set of degrees of freedom associated to the nodes.

- **Edges**

The geometric entity "edge" is associated to a vector function w_e^1 defined by:

$$w_e^1 = w_i^0 \, \boldsymbol{grad}\, w_j^0 - \, w_j^0 \, \boldsymbol{grad}\, w_i^0 \tag{III.18}$$

with w_i^0 and w_j^0 the nodal functions associated to nodes i and j of edge e. w_e^1 is equal to 1 on the edge e and 0 on all the others. The function w_e^1 is continuous on each element and its tangential component is continuous when passing from one edge to another. The space generated by the functions $\boldsymbol{w}_e^1$ is denoted by $\boldsymbol{W}^1$, thus if $\boldsymbol{u} \in \boldsymbol{W}^1$, we get:

$$\boldsymbol{u} = \boldsymbol{U}_e^t \boldsymbol{W}_e = \sum_{e=1}^{n_e} u_e \, \boldsymbol{w}_e^1 \tag{III.19}$$

with $\boldsymbol{W}_e$ the vector of the interpolation functions $\boldsymbol{w}_e^1$, $\boldsymbol{U}_e$ the set of degrees of freedom associated to the edges and u_e the circulation of $\boldsymbol{u}$ along the edge e defined by:

$$u_e = \int_e \boldsymbol{u}.\, dl \tag{III.20}$$

- **Facets**

The geometric entity "facet" is associated to a vector function w_f^2 defined by:

$$\begin{aligned} \boldsymbol{w}_f^2 = \; & 2w_i^0 \left(\boldsymbol{grad}\, w_j^0 \wedge \boldsymbol{grad}\, w_k^0\right) + 2w_k^0 \left(\boldsymbol{grad}\, w_i^0 \wedge \boldsymbol{grad}\, w_j^0\right) \\ & + 2w_j^0 \left(\boldsymbol{grad}\, w_k^0 \wedge \boldsymbol{grad}\, w_i^0\right) \end{aligned} \tag{III.21}$$

with w_i^0, w_j^0, w_k^0 the nodal functions of the nodes i, j and k of the facet f. $\boldsymbol{W}^2$ represents the facet elements space generated by the set of functions $\boldsymbol{w}_f^2$. Thus if $\boldsymbol{u} \in \boldsymbol{W}^2$, we have:

$$\boldsymbol{u} = \boldsymbol{U}_f^t \boldsymbol{W}_f = \sum_{f=1}^{n_f} \boldsymbol{u}_f \, \boldsymbol{w}_f^2 \tag{III.22}$$

where $\boldsymbol{W}_f$ is the vector of the interpolation functions and $\boldsymbol{U}_f$ the set of degrees of freedom associated with the facets of the mesh. As the normal component of functions $\boldsymbol{w}_f^2$ is continuous through each facet, therefore the normal component of a function attached to $\boldsymbol{W}^2$ is also continuous. The flux of $\boldsymbol{w}_f^2$ which across the facet f is equal to 1 and 0 on all the others. The flux of the function $\boldsymbol{u}$ across the facet f' verifies the relation (III.23)

$$\int_{f'} \boldsymbol{u} \, d\boldsymbol{f}' = \sum_{f=1}^{n_f} u_f \int_{f'} \boldsymbol{w}_f^2 \, d\boldsymbol{f}' = u_{f'} \tag{III.23}$$

III.1.4.4 Discretization of the magnetostatic formulation

Considering the scalar or vector variable U such as $U \in W^i$ with $i = (0, 1, 2, 3)$, its interpolation with Whitney's elements is:

$$U = \sum_k w_k u_k \quad \text{with} \quad k = \{n, e, f, v\} \tag{III.24}$$

The magnetic vector potential $\boldsymbol{A}$ is discretized with edge elements, and the vectors $\boldsymbol{N}_i$ and $\boldsymbol{N}_\phi$ are discretized with facet elements. The so-called facets and edges tree technique is used to ensure $\boldsymbol{div}\boldsymbol{N}_i = 0$ and $\boldsymbol{div}\, \boldsymbol{N}_\phi = 0$ in a discrete form [109].

$$\boldsymbol{A} = \sum_{e=1}^{n_e} a_e \, \boldsymbol{w}_e^1 \quad \boldsymbol{A} \in \boldsymbol{W^1} \tag{III.25}$$

$$\boldsymbol{N}_i = \sum_{f=1}^{n_f} n_{i_f} \, \boldsymbol{w}_f^2 \quad \boldsymbol{N}_i \in \boldsymbol{W^2} \tag{III.26}$$

$$\boldsymbol{N}_\phi = \sum_{f=1}^{n_f} n_{\phi_f} \, \boldsymbol{w}_f^2 \quad \boldsymbol{N}_\phi \in \boldsymbol{W^2} \tag{III.27}$$

where a_e is the circulation of the vector potential $\boldsymbol{A}$ on the edge e and n_{i_f} and n_{ϕ_f} are the fluxes across the facets f of $\boldsymbol{N}_i$ and $\boldsymbol{N}_\phi$ respectively.

To solve the vector potential formulation in its weak from, the Ritz-Galerkin's method is considered [110]. It consists in choosing the weighting function ψ as the interpolation function w, which depends on the considered discretization (w_n, w_e, w_f or w_v). By combining (III.25), (III.26), (III.27) and (III.16), we obtain the system of equations to be solved under the form $[M][A] = [F]$ with:

$$\mathrm{M}_{ij} = \int_{D_e} \mathcal{F}^{-1}(\boldsymbol{B})\boldsymbol{curl}\,\boldsymbol{w}_i^1 \cdot \boldsymbol{curl}\,\boldsymbol{w}_j^1 dv \quad \forall\,(i,j) = \{1,..N_e\}^2 \tag{III.28}$$

$$F_j = \int_{D_e} (\boldsymbol{N}_i\, i)\cdot \boldsymbol{w}_j^1\, dv - \int_{D_e} \mathcal{F}^{-1}(\boldsymbol{B})\boldsymbol{N}_\phi \phi \cdot \boldsymbol{curl}\,\boldsymbol{w}_j^1\, dv + \int_{D_e} \mathcal{F}^{-1}(\boldsymbol{B})\boldsymbol{B}_r \cdot \boldsymbol{curl}\,\boldsymbol{w}_j^1\, dv \qquad \forall\, j = 1,..N_e \tag{III.29}$$

$$A = \begin{bmatrix} A_1 \\ A_2 \\ \vdots \\ A_{N_e} \end{bmatrix} \tag{III.30}$$

where $\boldsymbol{B}$ is given by (III.9), v refers to the volume of the element D_e and N_e the number of degrees of freedom related to the considered volume.

The magnetostatic problem studied in this chapter contains a linear permanent magnet and ferromagnetic material, part of which is impacted by mechanical punching process. Thus, the function $\mathcal{F}^{-1}$ in (III.5) takes the value of $\nu_{pm} = 1/\mu_{pm}$ when the linear permanent magnet is considered, where ν_{pm} and μ_{pm} represent its magnetic reluctivity and permeability, respectively. In the ferromagnetic material, the scalar function $\mathcal{F}^{-1}$ has a nonlinear behavior, it is given by the reluctivity as a function of the magnetic flux density $\nu(B)$ in the non-impacted zone, while it is given by $\nu(B,\varepsilon)$ as a function of both magnetic flux density and plastic strain ε in the impacted zone. This last relation expresses the magneto-mechanical coupling due to the punching process; it has been modeled by the Sablik model in chapter II, in the following, its explicit expression will be developed.

III.1.4.5 Numerical integration – Gauss method

The numerical Gauss method is used to estimate the elementary integrals of the discretized formulation (III.28) and (III.29). For a given function f, the Gauss integration over a 3D reference element is given in (III.31):

$$\int_{-1}^{1}\int_{-1}^{1}\int_{-1}^{1} f(\xi,\eta,\varsigma)d\xi d\eta d\varsigma = \sum_{i=1}^{r} p_i\, f(\xi_i,\eta_i,\varsigma_i) \tag{III.31}$$

The integral of the polynomial function $f(\xi,\eta,\varsigma)$ is replaced by a linear combination of the values of f at the points ξ_i,η_i,ς_i (integration points) and the Gauss weights p_i. The coordinates of the r integration points are calculated to ensure the exact integral of the polynomial $f(\xi,\eta,\varsigma)$ which have at maximum the order $n \leq 2r-1$.
For example, Figure III.3 gives the location of the Gauss points of hexahedron reference element. Their coordinates ξ_i,η_i,ς_i and Gauss weights p_i are known values and can be found, for example, in [102][111].

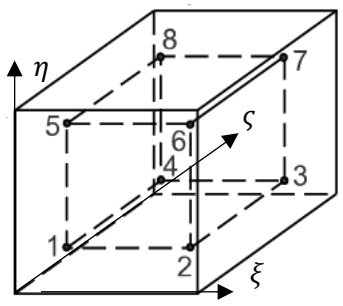

Fig. III.3 Location of the Gauss points in a reference hexahedron element [102]

III.2 Inverse of Sablik model

The magnetic behavior law modeled by the Sablik model, allows to express $\mathcal{F} = \mu(\boldsymbol{H}, \varepsilon)$. However, the vector potential formulation developed previously needs the inverse of the function $\mathcal{F}$, as $\mathcal{F}^{-1} = \nu(\boldsymbol{B}, \varepsilon)$. Since the Sablik model is based on the Langevin function, its inversion cannot be represented in an explicit form and requires an approximation.

Different approaches have been proposed in the literature to provide an approximation for the inverse Langevin function. Kuhn *et al* proposed a formula based on the Taylor series expansion, it uses the first four coefficients [112]. On the other hand, Itskov *et al* expressed the Taylor series with 22 terms [113] and 62 terms [114]. For the present study, to express the inversion of the Sablik model, an approximation approach based on the Padé technique has been considered [115]. Compared to the Taylor series expansion, its expression is a simple polynomial function.

The Sablik model given in (I.46), (I.56) and (I.57) derives from the Langevin function: $y = \mathfrak{L}(x) = \coth(x) - 1/x$, where $x = H_e/a$. Thus, based on [115] the Padé approximation of the inverse of the Langevin function $\mathfrak{L}^{-1}(y)$ is expressed by (III.32) such that:

$$x = \mathfrak{L}^{-1}(y) \approx \frac{y^2 - 3y + 3}{1 - y} \tag{III.32}$$

We set $y = M_{an}/M_s$ then (III.32) is applied to (I.46). It leads to the following expression:

$$\frac{H_e}{a} \approx \frac{\left(\frac{M_{an}}{M_s}\right)^2 - 3\left(\frac{M_{an}}{M_s}\right) + 3}{1 - \left(\frac{M_{an}}{M_s}\right)} \tag{III.33}$$

After introducing (I.56), in (III.33), the final expression of the inverse Sablik model is given by (III.34). It expresses the magnetic field magnitude H as a function of the magnetic flux density magnetitude B and the plastic strain ε (the parameter $a(\varepsilon)$ is function of the plastic strain: cf. section II.1.1).

$$H \approx \left\{ \left[\frac{\left(\left(\frac{B}{\mu_0} - H\right)\frac{1}{M_s}\right)^2 - 3\left(\left(\frac{B}{\mu_0} - H\right)\frac{1}{M_s}\right) + 3}{1 - \left(\left(\frac{B}{\mu_0} - H\right)\frac{1}{M_s}\right)} \right] a(\varepsilon) \right\} - \alpha\left(\frac{B}{\mu_0} - H\right) - H_\sigma \tag{III.34}$$

Figure III.4 gives the $B(H)$ curve obtained with Sablik model and the comparison between the exact $H(B)$ curve and its approximation obtained with (III.34).

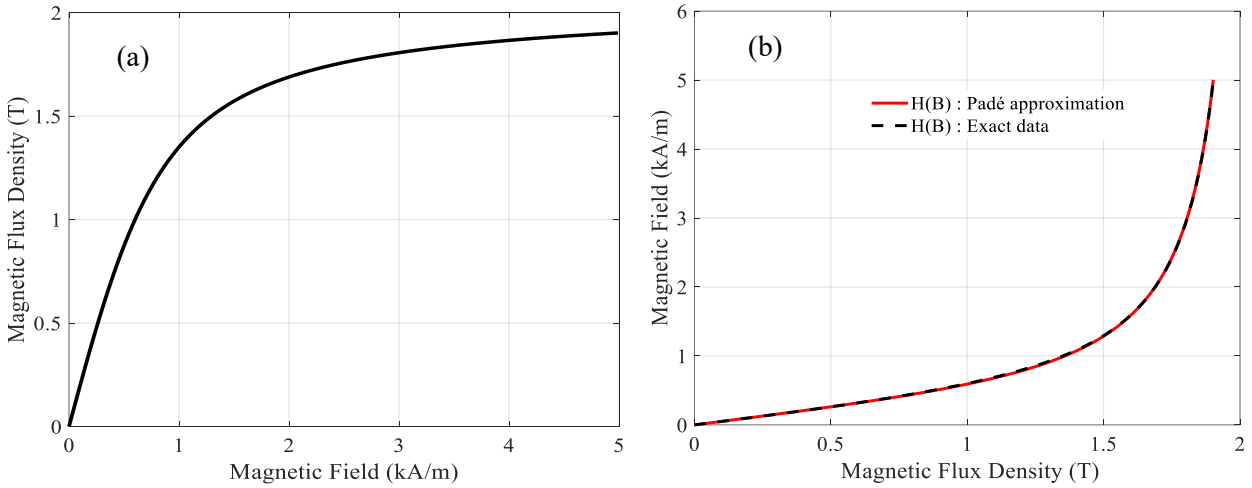

Fig III.4 $B(H)$ curve and the approximation of its inverse $H(B)$ curve

The result shows a good accuracy of the approximation method. As shown in Fig. III.5 the relative deviation does not exceed 1.5%.

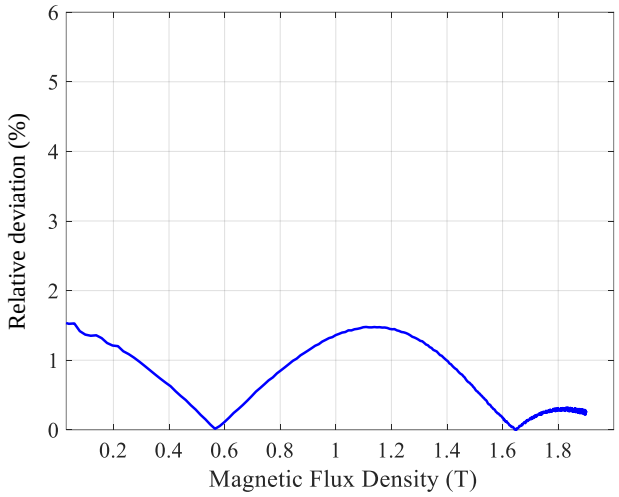

Fig III.5 Relative deviation of the Padé approximation method

Finally, to take into account the magneto-mechanical coupling, the reluctivity $\nu(B,\varepsilon) = H/B$ is considered in the assembly of the matrix M (III.28) and the vector F (III.29). Nevertheless, the spatial distribution of the plastic strain due to the punching process is needed to solve the FE problem. The next section proposes its estimation.

III.3 Determination of the plastic strain distribution

As explained previously, the Sablik model requires the knowledge of the distribution of the plastic strain. Although it can be approximated through micro-hardness measurements [30][38], we chose to perform a realistic mechanical simulation of the punching process based on the

literature. The explicit module of the industrial software ABAQUS which allows to simulate the fracture of materials has been used. A steel sheet sample has been simulated.

III.3.1 Punching process simulation

III.3.1.1 Principle of the industrial punching process

The conventional punching process is illustrated in Fig. III.6. It is made up of a holder and a die which maintain the sheet fixed. The punching tool is animated with a velocity, it exerts a force on the contact surface of the sheet until the fracture of the material. Fig. III.6-b gives the relevant parameters of the punching process, where r_d, r_p, ϑ_p are the punch corner radius, the die corner radius, and the velocity of the punch, respectively. The parameter c is the punch-die clearance, it represents the normal distance between the die and the punch tool and is expressed as a percentage of the sheet thickness.

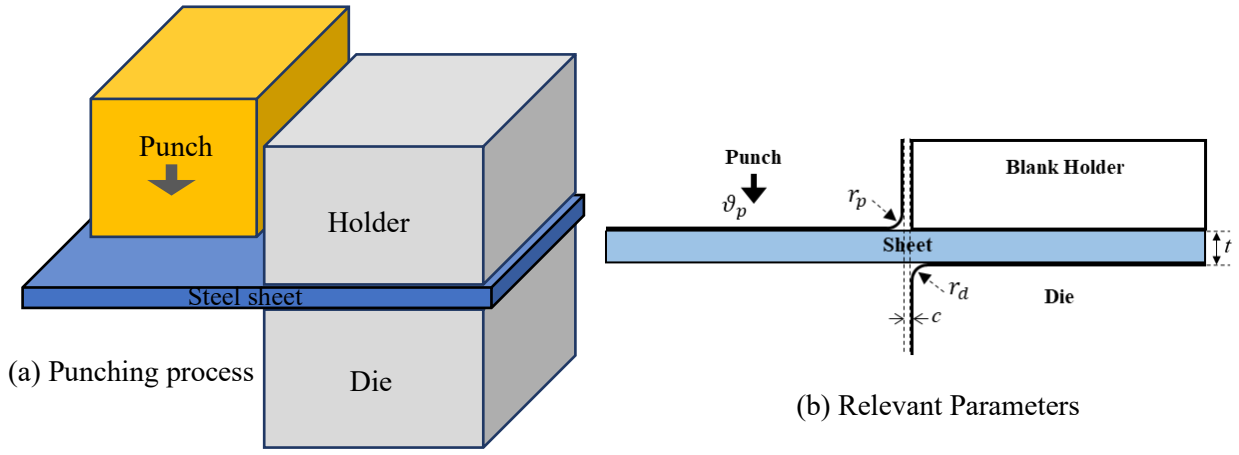

(a) Punching process (b) Relevant Parameters

Fig. III.6 Schematic illustration of a conventional punching process

The physical process leading to a material rupture can be described by the mechanics progressive damage, which is decomposed into three stages, corresponding to specific microstructural mechanisms [116]. The process is described in Fig. III.7.

- First, the application of the mechanical loading concentrates the constraints around the microstructural defaults included in the matrix, which leads to the germination (or nucleation) of the microcavities (Fig. III.6-b).
- Then, the microcavities grow progressively under the applied stress (Fig. III.7-c). This phase includes two combined phenomena. On the one hand, the increase in the number of cavities obtained by nucleation and, on the other hand, the increase of their size.
- Finally, coalescence phase of the cavities (Fig. III.7-d). Cavities close to each other interact and precipitate the growth of their volume until they meet and thus lead to the rupture of the material (Fig. III.6-e).

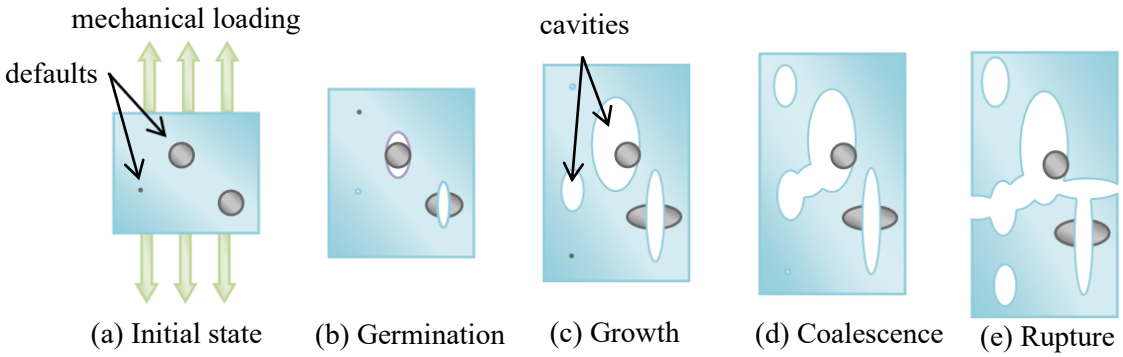

Fig. III.7 Schematic illustration of a conventional punching process [117]

In practice, the surface state of the punched area is an indicator of the quality of the process. Fig III.8 gives the different zones of the punching edge [118][119].

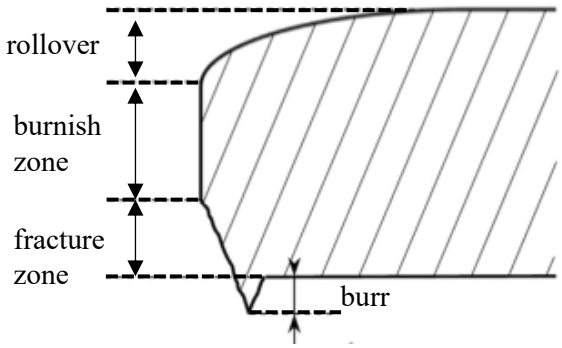

Fig. III.8 Punching edge schema [120]

The rollover zone is a curved zone that was entrained first during tool penetration. It is due to the plastic deformations induced at the beginning of punching process. Then the burnish and fracture zones which are characterized by a smooth appearance. Finally, the burr zone, which is a slight irregularity appearing at the end of the punching process. From the mechanical point of view, quality of the punching process is assessed by a smooth punching edge without rollover and Burr zones, which represent an ideal situation and is impossible to reach. The formation of the different zones is influenced by material properties, sheet thickness and the punching process parameters.

III.3.1.2 Material characteristics

The punching process simulation carried out in this section is based on the data given in the literature especially [121] and [35]. The investigated material is a non-oriented steel sheet (3%) Si-Fe M800 65A grade. It presents almost the same mechanical characteristics as the material used to identify the magneto-mechanical model in Chapter II.

To define the mechanical behavior of the material, the authors of [121] performed various tensile tests in different directions with respect to the rolling direction. The average mechanical properties are listed in Tab III.1 where σ_y^{max}, σ_y^{min} are the maximum and the minimum yield stresses related to the Luders strain plateau, classically encountered in 'bcc' (body centered cubic) steels such as

FeSi electrical steels (cf. section I.3.1.2). The values σ_m and ε_f are the ultimate stress and the failure plastic strain, respectively.

Tab. III.1 Mechanical characteristics for (3%) Si-Fe obtained by tensile tests along various directions in the sheet plane [121]

Parameter	RD	45°	TD	Average
σ_y^{max}(MPa)	312	322	317	317
σ_y^{min}(MPa)	301	311	295	302
σ_m(MPa)	422	444	428	433
ε_f (%)	40	40	42	40

According to the results of the mechanical characterization (Tab III.1), the material behavior is assumed to be mechanically isotropic. To account for the strain rate sensitivity, the authors of [121] propose the expression of stress given in (III.35):

$$\sigma\ (\varepsilon) = k\varepsilon^n \left(\frac{\dot{\varepsilon}}{\dot{\varepsilon_0}}\right)^m \tag{III.35}$$

where $\dot{\varepsilon}$ is the strain rate, $\dot{\varepsilon_0}$ the initial strain rate. m, k and n are the model parameters. Finally, the material input data used to perform the punching process simulation are summarized in Tab. III.2.

Tab. III.2 Input Material parameters

Elastic/General		**Plastic**		**Failure**	
Y (GPa)	198	k (MPa)	720	ε_f (%)	40
Poisson coef.	0.3	n, m	0.245, 0.0085	σ_m(MPa)	433
Mass density (Kg/m^3)	7850	$\dot{\varepsilon_0}$, $\dot{\varepsilon}$ (s^{-1})	10^{-5}, 5×10^{-3}	-	-

The material parameters given in Tab. III.2 which correspond to the different zones of the strain-stress curve are introduced separately in the software. The elastic zone is characterized by the Young modulus and the Poisson coefficient, the hardening zone is described by the equation (III.35). To introduce the failure conditions, the simplest shear criterion integrated in Abaqus software have been considered which requires the strain failure value, unlike the simulation carried out in [121] where a more elaborated failure model have been developed.

III.3.2 Parametric study of the punching of a steel sheet

In this section, the influence of the sheet thickness t and the punch-die clearance c on the rollover zone and the size of induced plastic strain area (DAZ: Deformation Affected Zone) is analyzed.

Since the thickness of the investigated steel sheet is small regarding its lateral (in-plane) dimensions, the punching process simulation is carried out in 2D. The plane stress hypothesis is

used; it considers that the out-of-plane normal stresses are equal to zero. The punching process parameters described in Fig. III.6-b are given in Tab. III.3.

Tab. III.3 Punching process parameters

Parameter	Value
r_d(mm)	0.02
r_p (mm)	0.02
ϑ_p (mm/s)	23

Figure III.9 gives the schematic of the simulated problem. The punch tool, the holder, and the die are modeled with analytical rigid surfaces. The mesh of the steel sheet is composed of 760 linear quadrilateral elements.

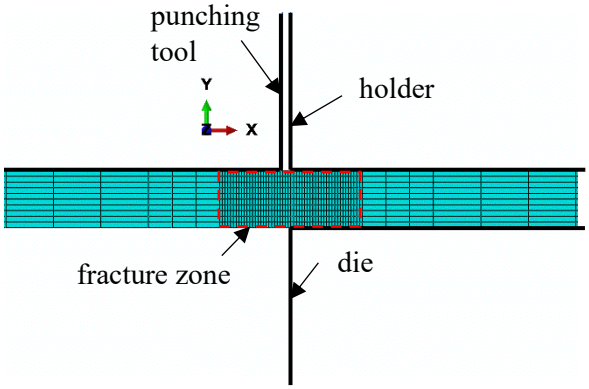

Fig. III.9 Schematic of the 2D simulated problem

First, by setting the punch-die clearance $c = 8\,\%$, the effect of the sheet thickness t is investigated. The simulation is conducted for $t = 0.35$ mm, $t = 0.5$ mm and $t = 0.65$ mm.

The punching simulation result is given in term of equivalent plastic strain ε, it is a scalar value estimated at each interaction point. The software Abaqus uses the following relation, where $\boldsymbol{\varepsilon}_{ij}$ is the strain tensor and, ':' represents the tensor double dot product.

$$\varepsilon = \sqrt{\frac{2}{3}\boldsymbol{\varepsilon}_{ij} : \boldsymbol{\varepsilon}_{ij}} \tag{III.36}$$

Thus, the Fig. III.10-a represents the equivalent plastic strain map in the useful part of the punched steel sheet. In Fig. III.10-b, to define the limits of the DAZ, the map is plotted for a strain less than 1%.

The result shows that the DAZ = 0.31 mm when the sheet thickness is 0.35 mm and 0.43 mm when the sheet thickness is 0.5 mm, while it reaches 0.6 mm when the sheet thickness is 0.65 mm. This behavior has been experimentally verified in [30] where it was shown that the impacted area is function of the sheet thickness.

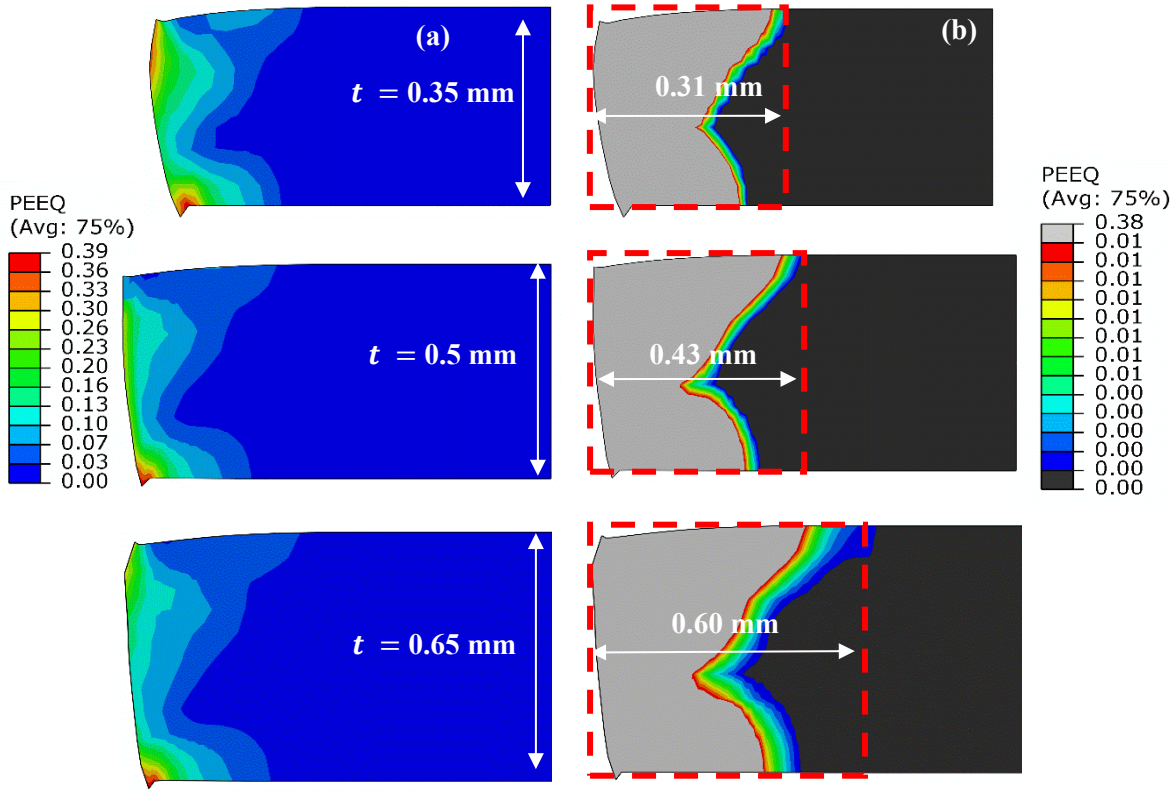

Fig. III.10 Plastic strain distribution – effect of sheet thickness (t =0.35 mm t =0.5 mm and t =0.65 mm)

In a second step, the steel thickness $t = 0.5$ mm is considered and the effect of the variation of the punch-die clearance is analyzed. The investigated values are given in Tab. III.4, they are chosen among the most studied in the literature [116][30].

Tab. III.4 Investigated clearances c

Clearance (%)	Clearance (mm)
4	0.02
8	0.04
15	0.075
20	0.1

Figure III.11 gives the distribution of the equivalent plastic strain. The result shows that the rollover zone and DAZ are both functions of the punch-die clearance. As expected, the mechanical state of the punching edge is better when the clearance is small and becomes degraded as it increases.

Figure III.12 shows the evolution of the rollover height as function of the punch-die clearance, and Fig III.12-b gives its relative value with respect to the sheet thickness. The clearance c =20% presents the most degrading value where the rollover height reaches about 10% of the sheet thickness.

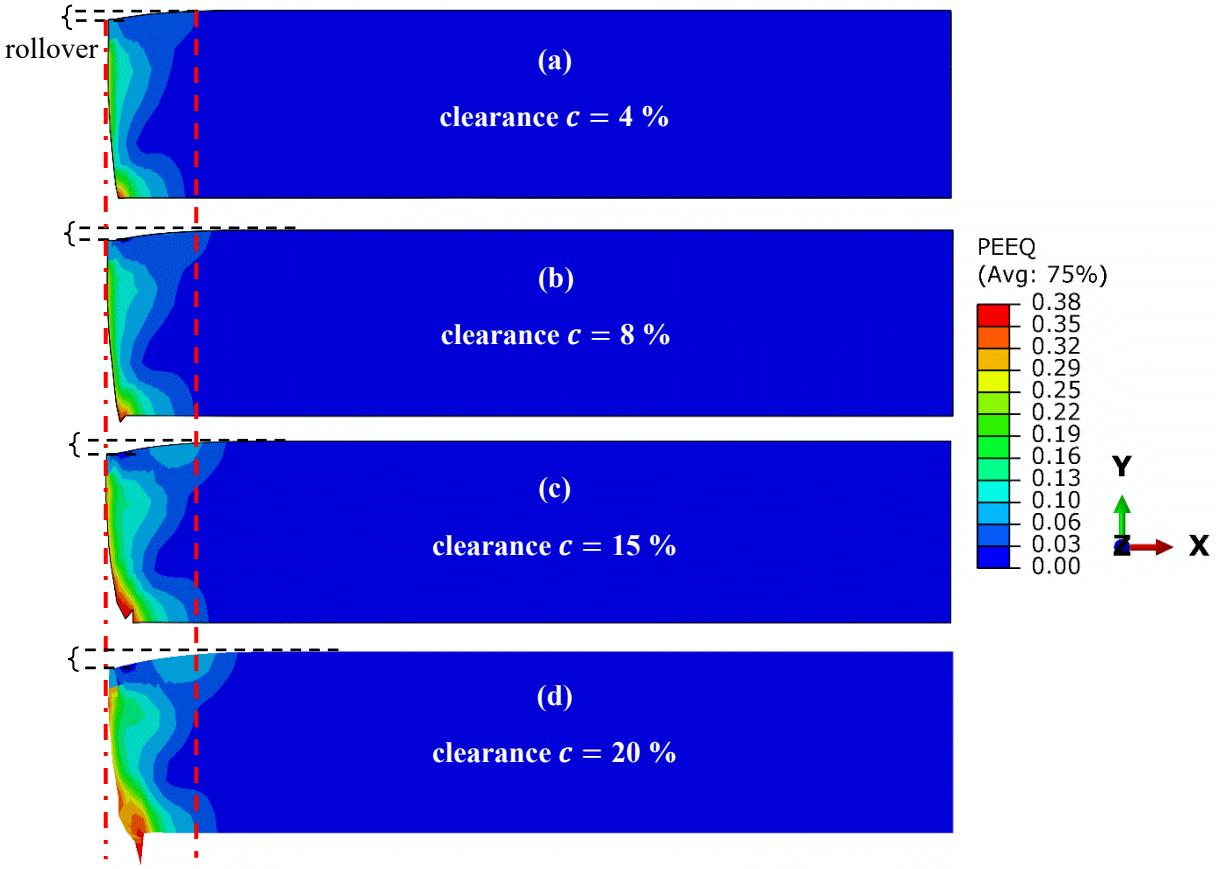

Fig. III.11 Distribution of the equivalent plastic strain in the steel sheet with t =0.5 mm for different punch-die clearance (a) c = 4 %, (b) c = 8 %, (c) c = 15 %, (d) c = 20 %

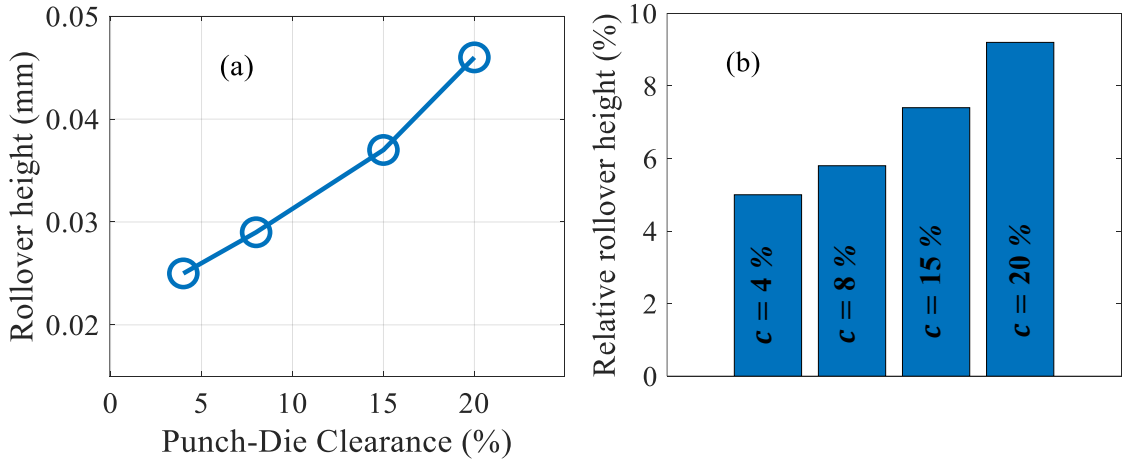

Fig. III.12 (a) Evolution of the rollover height versus punch-die clearance (b) relative rollover height

As for the study devoted for the effect of the sheet thickness, the equivalent plastic strain is plotted for values less than 1% to better define the DAZ. Fig. III.13 gives the evolution of its width for different punch-die clearances. It shows proportionality with the punch-die clearance, the widest DAZ is obtained for c =20%.

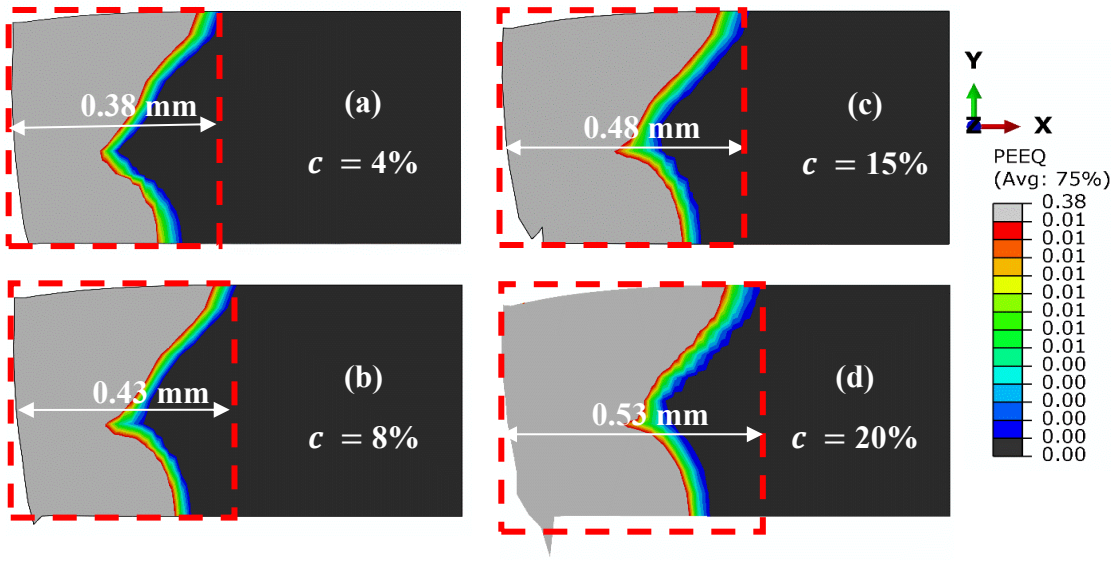

Fig. III.13 Distribution of the equivalent plastic strain in the steel sheet with t =0.5 mm for different punch-die clearance (a) c = 4 %, (b) c = 8 %, (c) c = 15 %, (d) c = 20 %

The parametric study carried out in this section showed that the quality of the lamination edge depends on the punching parameters. Furthermore, the width of the DAZ is proportional to both sheet thickness and punch-die clearance. This behavior is supported by different works published in the literature; it was shown that the size of the rollover zone is proportional to the clearance punch-die [122], and the smaller rollover and burr zones are obtained with a smaller clearance value. However, a small clearance increases the radius of the punch tool which leads to its deterioration and consequently leads to the deterioration of the quality of the punching edge [123]. Indeed, the definition of an optimal punching parameters is not obvious, although, it has been shown that the clearance 5-10 % is recommended [124]. Thus, to carry out the magneto-mechanical simulation the plastic strain distribution given with a clearance c =8 % will be considered.

III.4 Finite element implementation

This section investigates the effect of punching process on the magnetic properties of a 2D steel sheet. It combines the FE magnetostatic formulation, the inverse Sablik model and the result of the mechanical simulation.

III.4.1 Exploitation of the punching process simulation result

The punching process simulation gives the plastic strain distribution near the lamination edge. In this context, when one wants to perform a magneto-mechanical simulation using a finite element method (FEM), the nonlinear magnetic reluctivity is estimated by the inverse Sablik model in each element of the mesh. Thus, the ideal way would be to consider the spatial distribution of the plastic strain as given by the punching process simulation. However, in electromagnetic FE simulations, especially for electrical machines, the iron core made from laminations is often modeled as a whole stack, without accounting for its laminated structure. This assumption is justified when magnetic fields remain in the lamination plane (2D approximation) and the magnetic properties are

homogeneous along the lamination thickness. In the present case, to account for the cutting edges, one would prefer to model each lamination independently to account for the strong inhomogeneity of the material properties introduced by the punching process (see Fig. III.10, Fig. III.11 and Fig. III.13). But, modeling independently each lamination, with a sufficiently fine mesh to account for the stress along its thickness, is not achievable for applications such as electrical machines where the iron core is made from hundreds of stacked laminations. Besides, the ratio of dimensions in the lamination plane to their thickness often reaches several hundreds (and more) that would require a large mesh. Finally, in 2D magnetic approaches, it is intrinsically not possible to account for the properties along the thickness.

Therefore, the implementation in FEM of the degraded magnetic properties at cutting edges is often approximated by a "degradation profile". This profile is usually represented by an exponential function of the distance from the punching edge. Figure III.14 illustrates its calculation method.

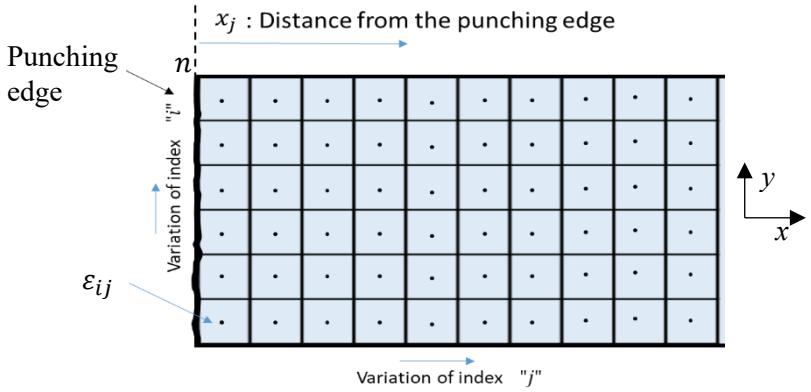

Fig III.14 Calculation method of the degradation profile

Depending on the distance from the punching edge x_j, the degradation profile is defined by taking the corresponding average ε_{v_j} value of the equivalent plastic strain ε_{ij} along the *y*-axis, as given in equation (III.37) where n represents the total number of elements along *y*-axis.

$$\varepsilon_{v_j} = \frac{1}{n}\left(\sum_{i=1}^{n} \varepsilon_{ij}\right) \tag{III.37}$$

Figure III.15 gives the degradation profile based on the punching simulation performed with the sheet thickness t =0.65 mm and clearance c = 8%. It is fitted with an exponential function (III.38), where γ and β are the parameters of the model and x represents the punching edge distance.

$$\varepsilon_v = \gamma e^{\beta x} \tag{III.38}$$

The obtained degradation profile is compared with the result of a punching simulation carried out in [35] under similar conditions. The comparison shows a reasonable agreement of the qualitative behavior. Indeed, the plastic deformation is maximum at the edge and decreases as the distance x increases, this behavior is also supported by micro-hardness measurement [16][35].

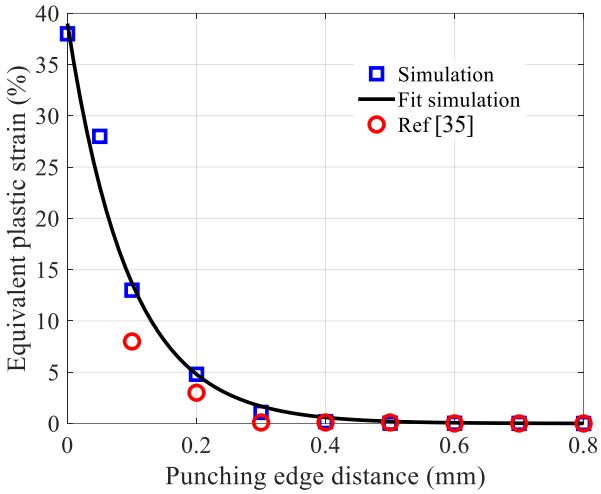

Fig. III.15 Degradation profile calculated with the simulation result obtained for t =0.65 mm and c =8%

Figure III.16 gives the degradation profiles calculated under the same punching process conditions (c =8%) for different sheet thicknesses: t =0.35 mm, t =0.50 mm and t =0.65 mm. As expected, since the steel sheet with t = 0.65 mm has a wider DAZ (cf. Fig. III.10), its degradation profile presents a higher magnitude compared to the sheet thicknesses t =0.35mm and t =0.5mm.

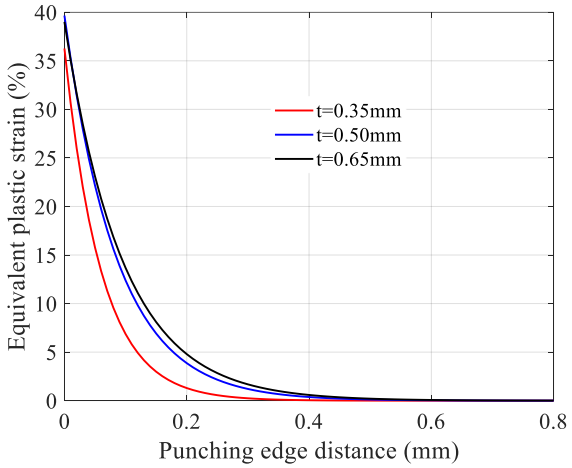

Fig. III.16 Degradation profile calculated for different sheet thickness t = 0.35 mm, t =0.50 mm and t =0.65 mm.

Table III.5 gives the parameters of the degradation profile model (III.38) fitted with the result of the punching process simulations.

Tab. III.5 Parameters of the degradation profile model

Parameter	t = 0.35mm	t = 0.50mm	t = 0.65mm
γ	36.27	39.66	39
β	-16.65	-11.64	-10.48

By considering the degradation profile to define the plastic strain, the reluctivity of each element which was function of the magnetic flux density and of the plastic strain, is henceforth function of the magnetic flux density and of the distance from the punching edge $\nu(B, x)$.
The definition of the distance from the punching edge x is performed for each integration point (Gauss point) of each element of the mesh. When the punched edge is straight, as in the steel sheet of Fig III.14, the distance x coincides with the x-coordinate of the Gauss point. However, when it is a curved line as illustrated in Fig. III.17, x is chosen as the shortest distance (the blue dotted line in Fig. III.17). To ensure the accuracy of the calculation, the number of the Gauss points of the mesh elements corresponding to the DAZ is increased.

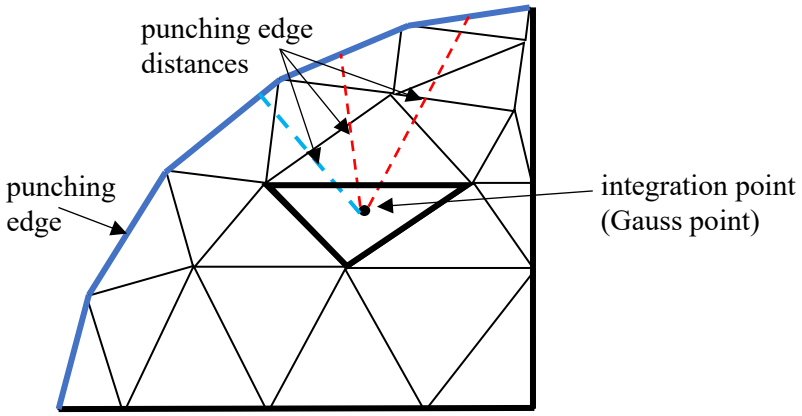

Fig. III.17 Estimation of the distance x from a curved punching edge.

III.4.2 Academic test – 2D problem

The inverse Sablik model is implemented in an academic 2D magnetostatic problem composed of a steel sheet sample 3×3 cm² punched at the bottom edge with an imposed magnetic flux ϕ=0.05 Wb (Fig. III.18) (the derived 2D magnetostatic formulation is given in Appendix A). A Matlab® based FE solver have been developed. The degradation profile calculated with sheet thickness t =0.5 mm (Fig. III.16) has been considered.

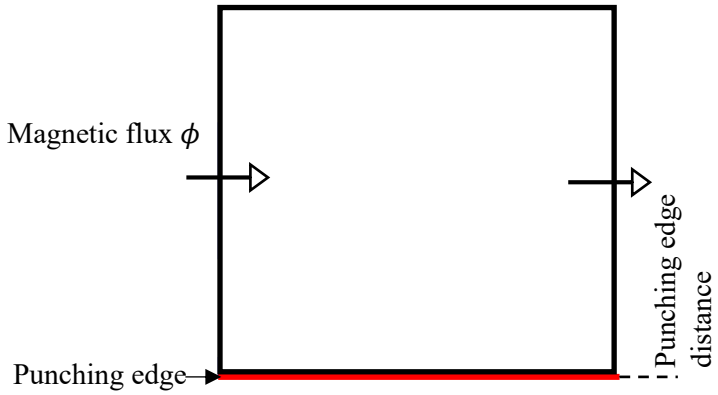

Fig. III.18 2D magnetostatic problem – a punched steel sheet

For different punching edge distances, Fig. III.19 gives the evolution of the modeled $B(H)$ curves and their corresponding relative permeability (Fig. III.19-b). Away from the punching edge the material is not impacted by the plastic strain, and the permeability is maximum, while it is strongly degraded at the punching edge.

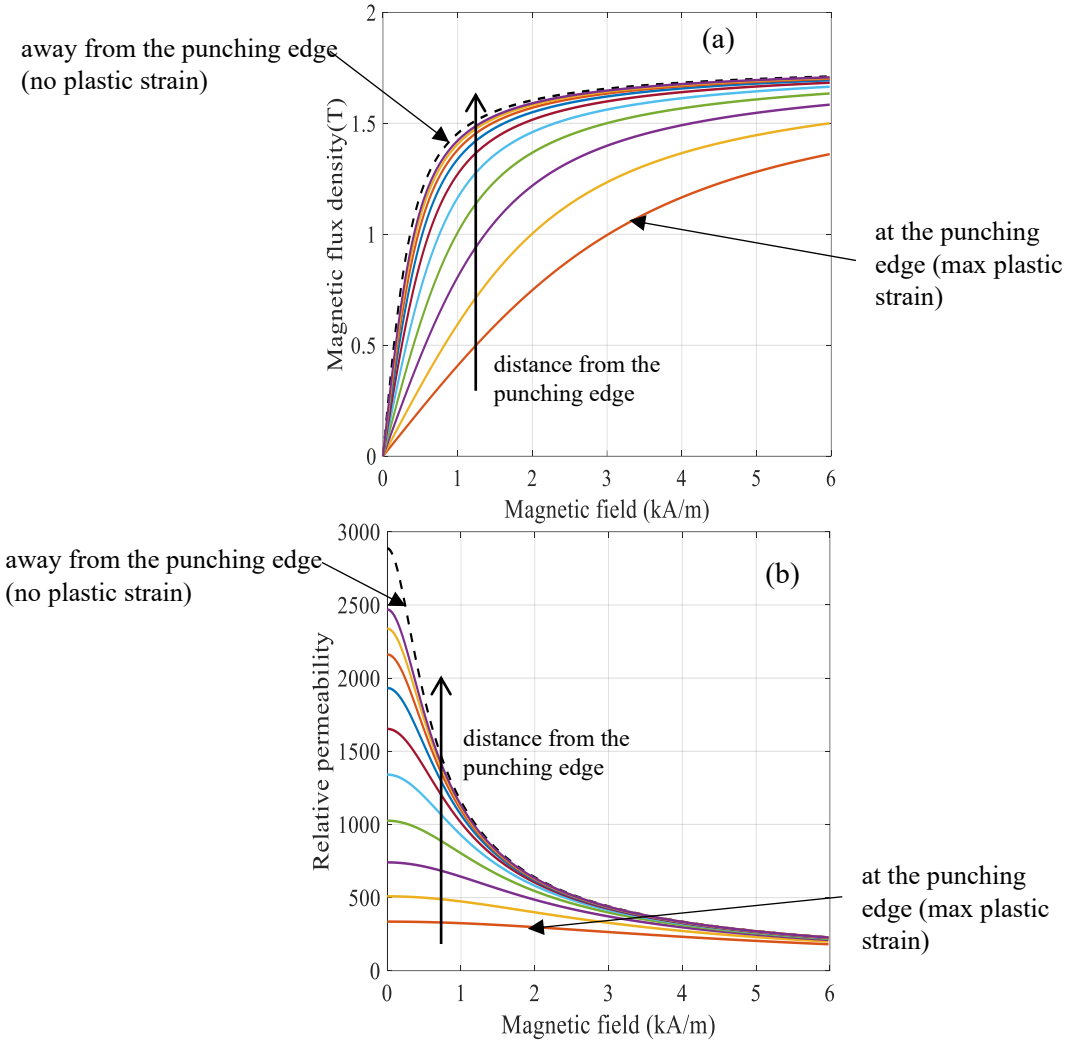

Fig. III.19 modeled BH curves and relative permeability for different punching edge distances.

Thus, based on the distance from the considered punching edge, a reluctivity is calculated for each element of the mesh. The result of the simulation is given in Fig. III.20, it shows that, as expected and due to the high degradation of the magnetic properties, the magnetic flux density is lower near the punching edge where the plastic strain is concentrated. This behavior is supported by various work in the literature [72][73].

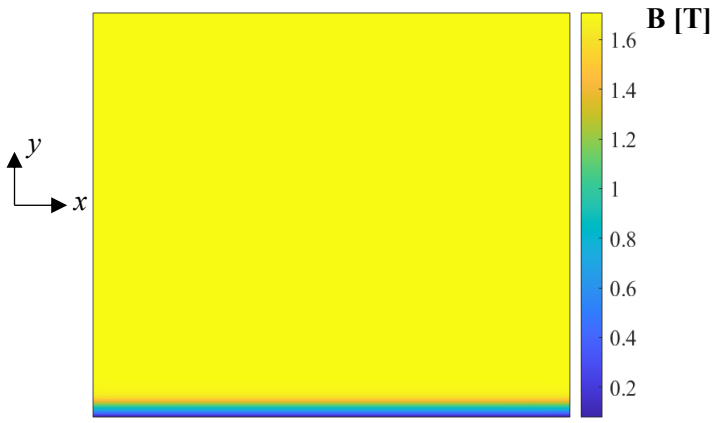

Fig. III.20 Distribution of the magnetic flux density in a steel sheet sample 3×3cm² punched at the bottom with an imposed magnetic flux ϕ=0.05 Wb.

For a given x coordinate of the steel sheet sample, the evolution of the magnitude of the magnetic flux density along y-axis is plotted in Fig III.21. At the punching edge the magnitude of $\boldsymbol{B}$ decreases until reaching about 0.1 T.

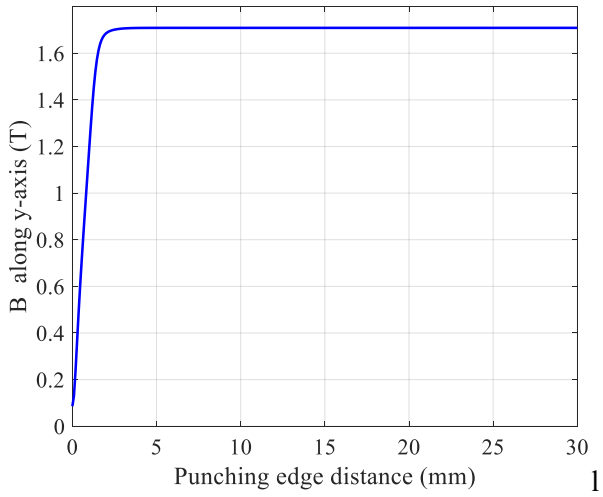

Fig. III.21 Magnitude of the magnetic flux density along y-axis

III.5 Conclusion

In this chapter, the FE magnetostatic problem considered to simulate the magneto-mechanical coupling has been presented. To interface both physics, the Padé approximation has been used to inverse the Sabilk that accounts for the plastic strain. Thus, to complete the modeling chain, a punching process simulation of a steel sheet has been carried. The effect of the punching parameter punch-die clearance and the sheet thickness on the quality of the lamination edge, especially the width of the DAZ have been investigated. Finally, the FE magnetostatic problem, the plastic strain distribution given by punching process simulation and the inverse Sablik model have been associated to simulate the magnetic behavior of an academic example (steel sheet), where a strong degradation of the magnetic flux density near the lamination edge has been shown.

Chapter IV

Applications

This chapter investigates the effect of punching process, by considering the degradation profile, on the magnetic behavior of an academic application represented by a single-phase inductance and of an industrial synchronous machine. Then, we will more closely consider the method used to account for the plastic strain at the punching edge, especially by comparing the magnetic behavior of punched specimens (steel sheet and tooth of an electrical machine) when the full plastic strain field is considered and when the degradation profile is used.

All magnetic simulation results presented in this chapter have been carried out with the 3D FEA software *code_Carmel* [125] where the required numerical tools (inverse Sablik model, distance calculation from the punching edge and degradation profile) have been implemented. Additional, developments have been realized to account for the full plastic strain field and will be more detailed in the adequate section.

IV.1 Application of the punching effect simulation

IV.1.1 Academic application – Single phase inductance

The academic application illustrated in Fig. IV.1-a, represents a single-phase inductance with an air gap. The dimensions and the considered punching edges are given in Fig. IV.1-b. The magnetic core is modelled as a whole stack, without accounting for its laminated structure, the plastic strain distribution at the punching edges is represented by the degradation profile calculated for sheet thickness t =0.5mm. The magnetostatic formulation in terms of magnetic vector potential is considered.

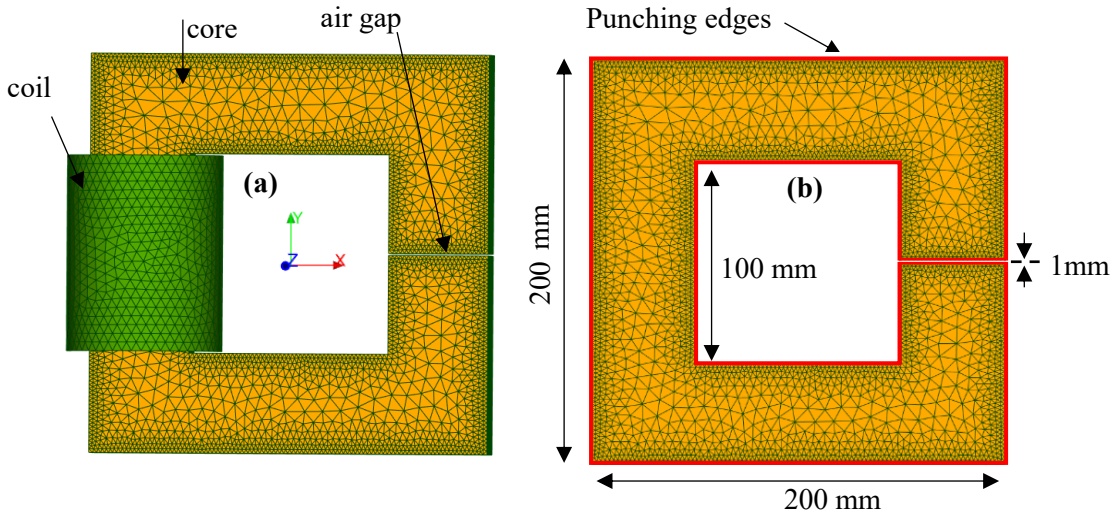

Fig. IV.1 Mesh and dimensions of the magnetic core

Figure IV.2 (a) and (b) give the magnetic flux density distribution in the magnetic core with and without considering the punching effect, respectively.

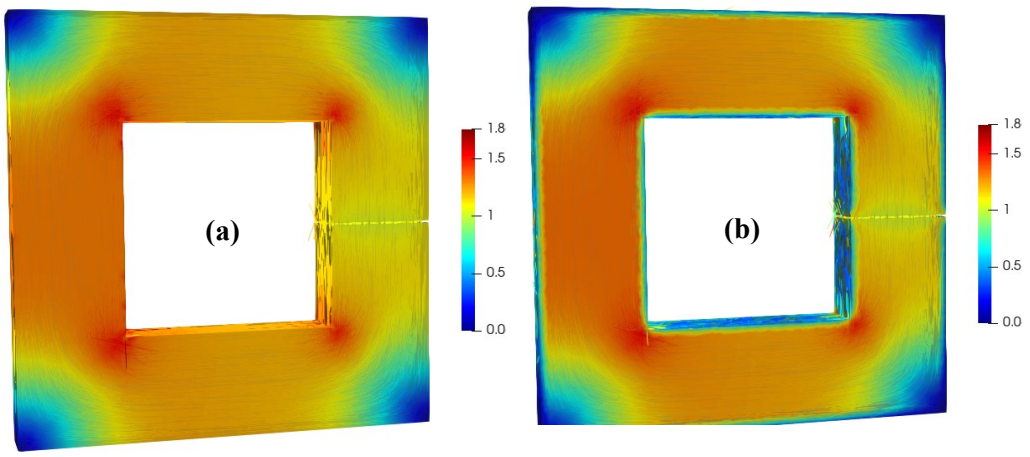

Fig. IV.2 Magnetic flux density map with (b) and without (a) considering the punching process effect.

As expected, due to the degradation of the permeability near the considered punching edges, the magnetic flux density is affected. Fig. IV.3 gives the difference of the magnetic flux density with and without considering the punching effect for a given value of the current fixed to 8A. We observe that, locally at the punching edges, the variation of magnetic flux density reaches up to 0.9 T.

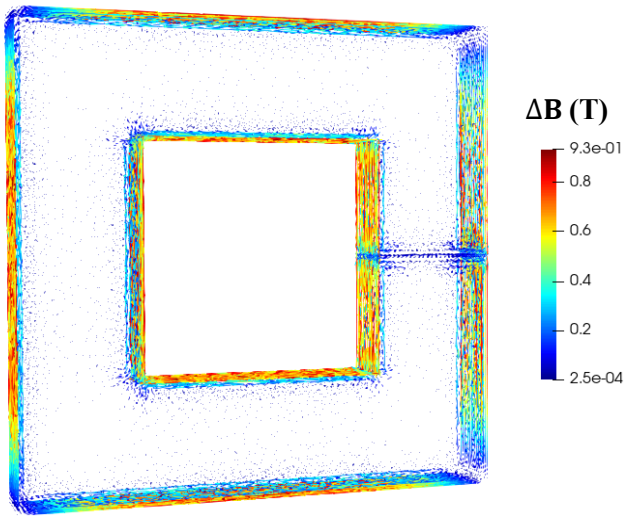

Fig. IV.3 Difference of magnetic flux density distribution between with and without the punching effect

To analyze the effect of punching on the magnetic flux distribution in the airgap, the coil is now supplied with different current values and the average magnetic flux that cross the air gap is analyzed. As illustrated in Fig. IV.4 the considered section is set fix, then the magnetic flux is calculated, with and without considering the effect of the punching process.

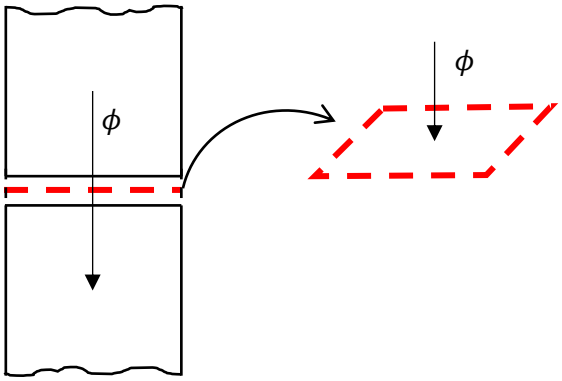

Fig. IV.4 Illustration of the magnetic flux crossing the air gap.

The relative decrease $\delta_\phi = \left(\delta_{\phi_0} - \delta_{\phi_{\text{deg}}}\right)/\delta_{\phi_0}$ is calculated for different supply currents in the excitation coil, where δ_{ϕ_0} and $\delta_{\phi_{\text{deg}}}$ represent, respectively, the average magnetic flux calculated without and with considering the punching effect. The evolution of δ_ϕ versus the average magnetic flux densities is given in Fig. IV.5 where a decrease of the average magnetic flux crossing the air gap is observed.

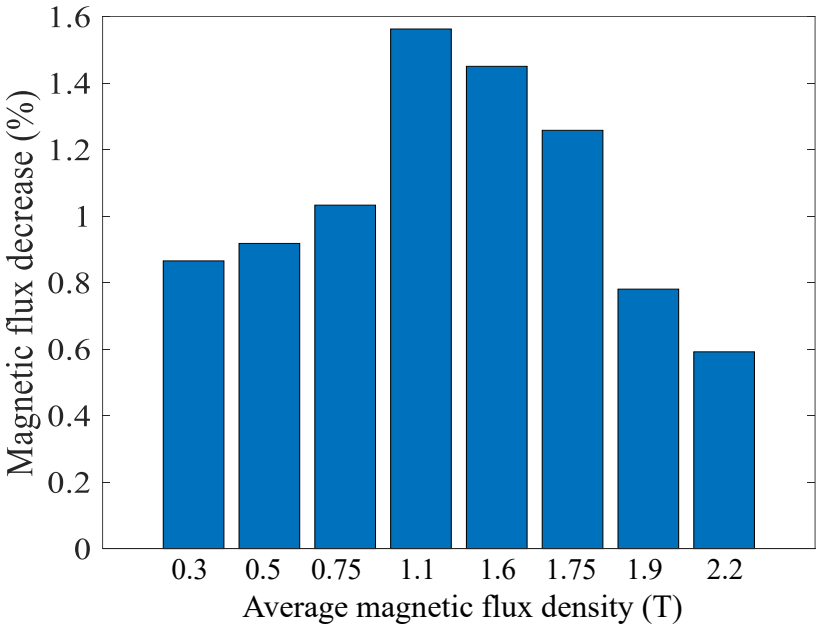

Fig. IV.5 Relative magnetic flux decrease δ_ϕ vs coil supply current.

The diminution of the magnetic flux through the air gap is obviously due to the degradation of the magnetic properties near the punching edges, which leads to increase virtually the air gap. Therefore, the magnetic flux expands outside the magnetic core. Furthermore, δ_ϕ is function of the coil supply current, consequently on the magnetic flux density crossing the magnetic core.

IV.1.2 Industrial application – Synchronous machine

As industrial application, a 5-phases permanent-magnet synchronous machine is considered. Its mesh and description are given in Fig. IV.6.

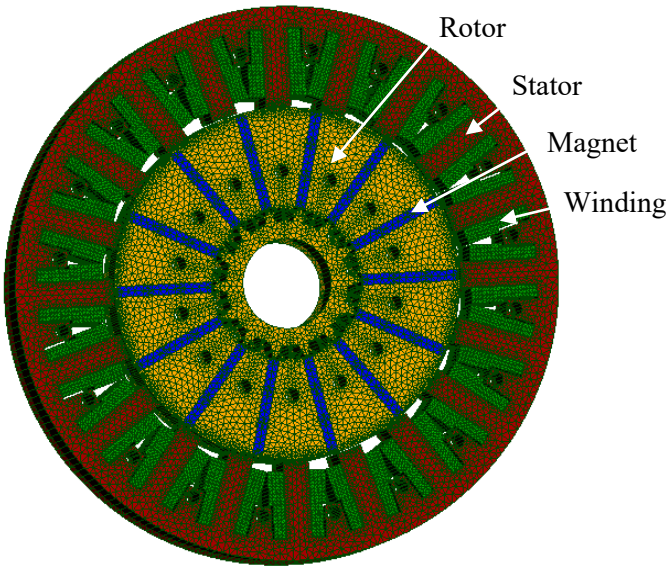

Fig. IV.6 Description of the simulated synchronous machine

The dimensions and the power of the synchronous machine are given in Tab.IV.1

Tab. IV.1 Characteristics of the simulated synchronous machine

Quantities	Value
Power (kW)	10
Outer diameter (mm)	152
Length (mm)	92
Tooth width (mm)	7

Due to the lack of magnetic symmetry, the whole cross section is modeled. A no-load simulation, at speed 750 rpm (corresponding to 87.5Hz stator frequency), has been carried out using the magnetic vector potential formulation. The punching effect is considered in the numerical model by using the calculated degradation profile for the sheet thickness t =0.5mm.
The punching effect is considered on the whole inner perimeter of the stator yoke, including the teeth and slot edges.

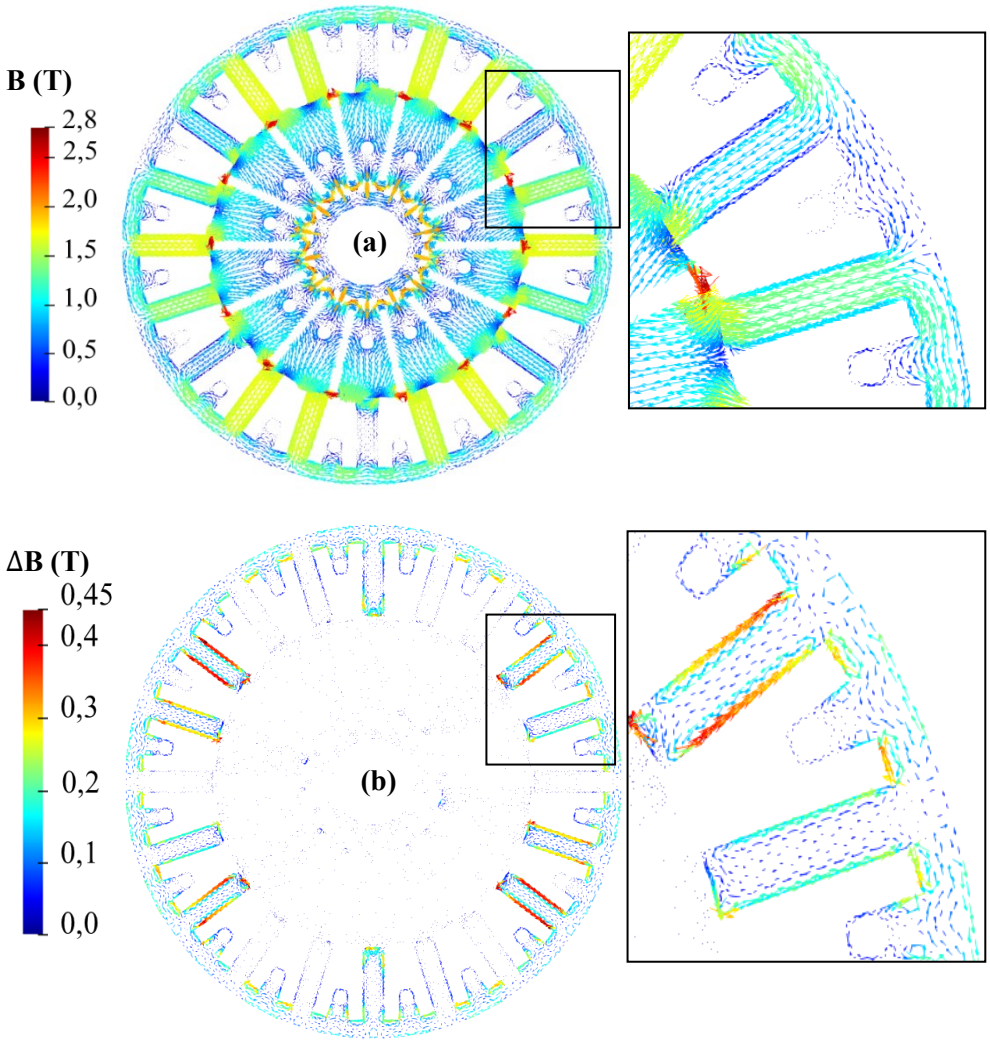

Fig. IV.7 (a) Magnetic flux density distribution considering punching effect (b) Difference between cases with and without the punching effect

In Fig. IV.7-a, the resulting magnetic flux density is given, and Fig. IV.7-b shows the difference in terms of magnetic flux density between simulations with and without consideration of the punching effect. The decrease of magnetic flux density at the punching edge can reach about 0.4 T, which is significant.

Figure IV.8 presents the linkage magnetic fluxes associated to the windings with and without punching effect. It shows a small decrease when the punching effect is considered.

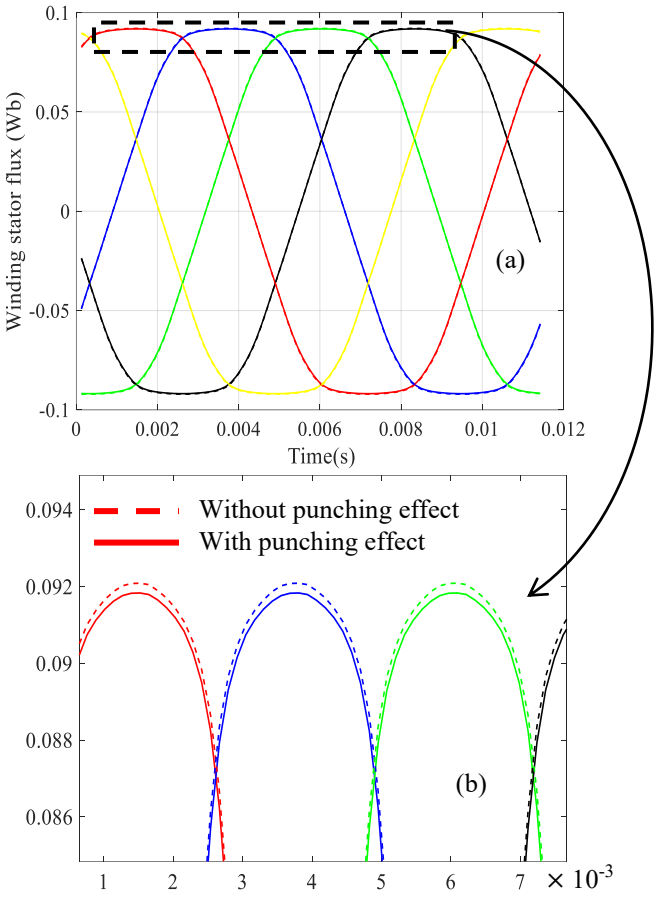

Fig. IV.8 Linkage magnetic fluxes.

Locally, especially in the teeth as observed in Fig. IV.7 (a), the degraded punching edges will lead to a modification of the magnetic flux density distribution and conseqeuntly an impact on the iron losses is inevitable. Therefore, the effect of punching process on the iron losses P in the electrical machine is now alaysed. As a first approach, to estimate the losses, the Jordan model given in (IV.1) is applied.

$$P = k_h(\varepsilon)\, f\, B^{\alpha(\varepsilon)} + k_{cl}\, f^{\,2} B^{\,2} \tag{IV.1}$$

As hypothesis, and based on the literature, we consider that mainly static losses are affected by the punching. Then, the hysteresis loss parameters k_h and α are considered depending on the plastic strain. The parameter k_{cl} is related to the classical eddy current losses (supposed to be unaffected by the cutting) and f is the frequency. Fig IV.9 gives steps of iron loss calculation.

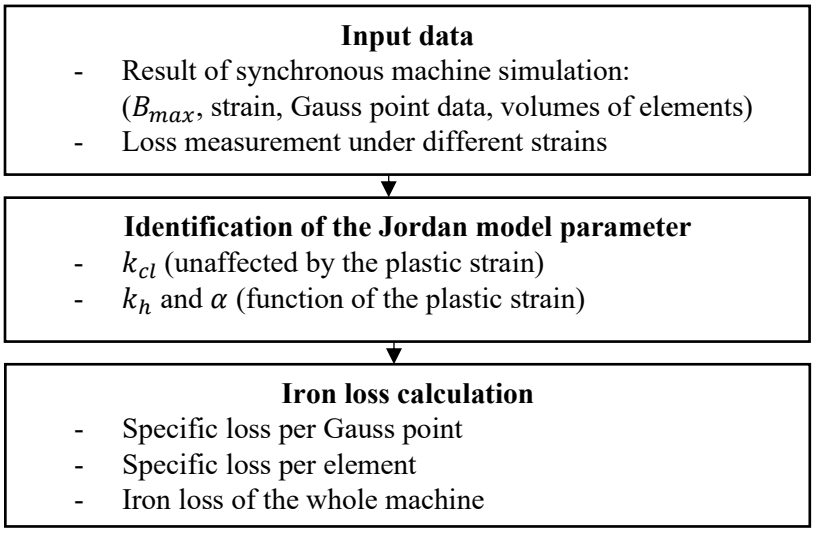

Fig. IV.9 Steps of the iron loss calculation

The evolutions of static parameters were identified using loss measurement under different plastic strains for the electrical steel grade M330-35A. The constant parameter k_{cl} is fixed to 7.90×10^{-5}, the relation (IV.2) gives the evolution of k_h with respect to the plastic strain ε.

$$k_h = exp\left(a_{k_h} + \frac{b_{k_h}}{\varepsilon + c_{k_h}}\right) \tag{IV.2}$$

where a_{k_h}, b_{k_h}, c_{k_h} are the parameters of the model. Their values are given in Tab. IV.2

Tab. IV.2 k_h model parameters

Parameters	Value
a_{k_h}	-2.67
b_{k_h}	7.46×10^{-3}
c_{k_h}	7.03×10^{-3}

The evolution of the Jordan model parameter α with respect to the plastic strain is given by the relation (IV.3). where b_α, a_α, c_α, d_α are the parameters of the model. Their values are given in Tab. IV.3.

$$\alpha = b_\alpha + \frac{(a_\alpha - b_\alpha)}{1 + \left(\frac{\varepsilon}{c_\alpha}\right)^{d_\alpha}} \tag{IV.3}$$

Tab. IV.3 α model parameters

Parameters	Value	Parameters	Value
a_α	1.99	c_α	0.0032
b_α	1.22	d_α	0.59

The evolution of the fitted and the identified parameters k_h and α with respect to the plastic strain are given by Fig. IV. 10.

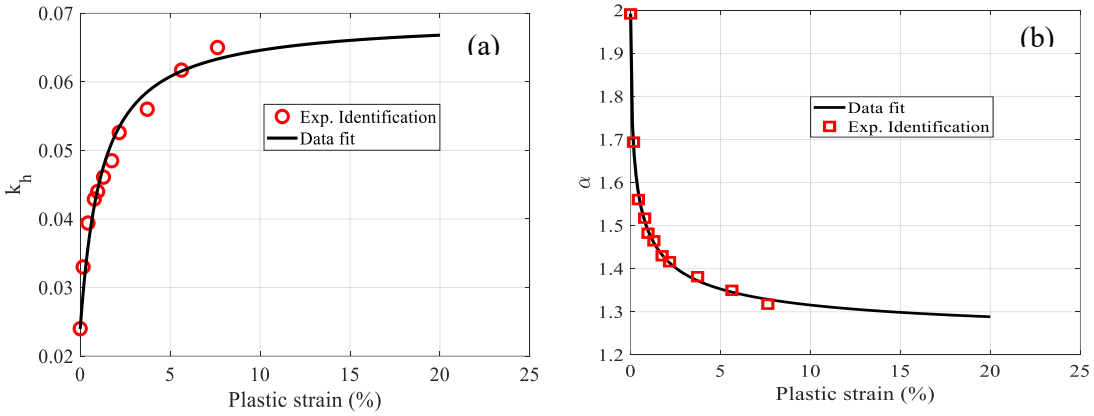

Fig. IV.10. Evolution of the loss model parameters (a) k_h and (b) α with respect to the strain

As illustration, Fig. IV.11 gives the comparison of the iron loss evolution between the experimental data and the identified Jordan model for 0.43 % and 7.63% plastic strains and for 50, 100 and 150 Hz frequencies.

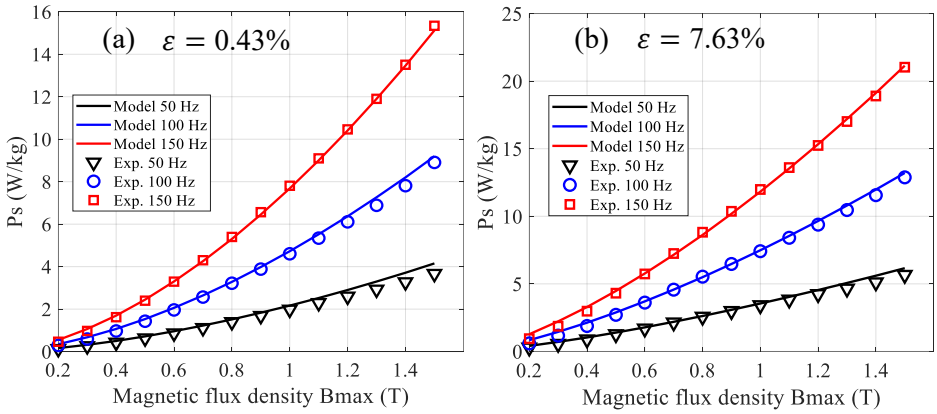

Fig. IV.11 Evolution of the modeled and measured iron loss for 50, 100 and 150 Hz (a) for plastic strain $\varepsilon = 0.43\%$ (b) for plastic strain $\varepsilon = 7.63\%$

Finally, Table IV.4 gives the core losses in the stator yoke calculated with and without considering the punching process effect, it is shown that it increased by about 38%.

Tab. IV.4 Simulated iron loss with and without punching effect

Core loss without punching	Core loss with punching
25.55 W	35.40 W

IV.1.3 Synthesis

The applications investigated in this section showed the impact of punching process on the magnetic behavior. Besides the degradation of the magnetic flux density at the punching edge, the

single-phase inductance example showed that the magnetic flux crossing the air gap is degraded. Furthermore, the simulation carried out on the synchronous machine allowed to estimate about 38 % increase of iron loss.

The estimation of the plastic strain distribution due to the punching process is a central step of the considered magneto-mechanical simulation strategy, which is based on the Sablik model. Thus, the method of its implementation in the numerical tool should be carefully considered. The following section propose to evaluate the ability of degradation profile to represent the full plastic strain from the magnetic point of view.

IV.2 Comparison of full plastic strain and degradation profile

The identification of the degradation profile with the average equivalent plastic strain (section III.4.1) is now compared with a 2D extruded mechanical simulation based on the full strain distribution along the sheet thickness. The analysis is conducted by comparing the distribution of the magnetic flux density and the total magnetic energy for two examples: a steel sheet sample and a tooth of an electrical machine. The magnetic simulations are carried out using the software *code_Carmel.*

IV.2.1 Finite element analysis – Steel sheet

The 2D model of the punched steel sheet is extruded to form a 3D model in order to be in the same condition as an electrical machine tooth. To perform this transformation, a function has been developed in MATLAB. First, it converts and adapts the files from Abaqus (mesh and plastic strain) to a format supported by *code_Carmel*. Then, from this result a steel sheet punched on two parallel sides is generated by mirroring. The width of the created sample can be controlled. The principle steps of the transformation operation are given in Fig. IV.12.

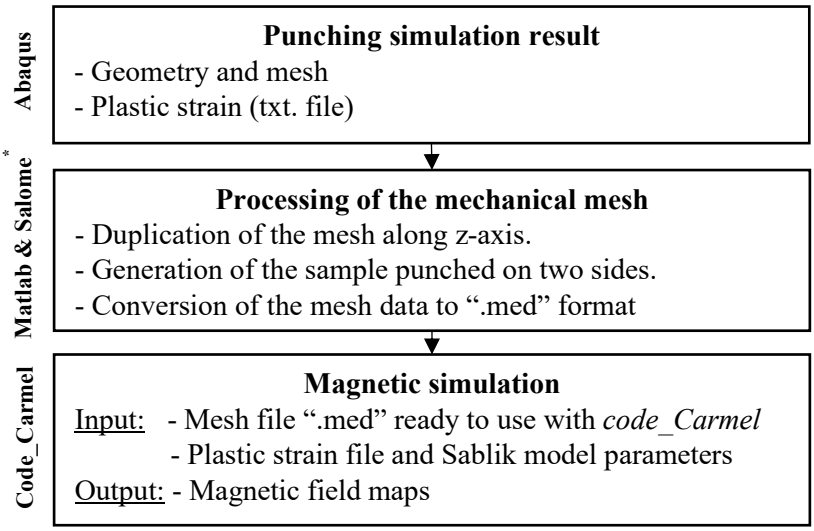

Figure IV.12 Principal steps of the mesh transformation operation.

*Salome is an open-source software that provides a generic pre- and post-processing platform for numerical simulation.

The FE analysis is first performed on the steel sheet punched on one side. Fig. IV.13 gives the 3D transformation. The FE magnetostatic problem, with an imposed magnetic flux along the z-axis (parallel to the cutting edges) is solved. The degradation profile calculated for the sheet thickness t =0.50 mm is considered. The sample dimensions are length = 5.4 mm and width = 3 mm.

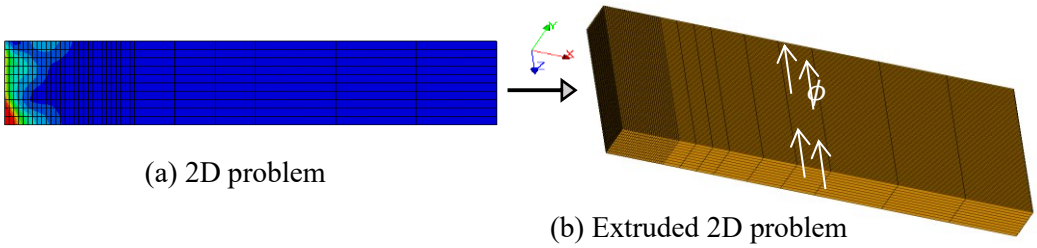

(a) 2D problem

(b) Extruded 2D problem

Fig. IV.13 Transformation of the 2D problem to an extruded 2D problem (3D)

Figure IV-14 presents the magnetic flux density in the steel sheet when the full plastic strain distribution is considered (Fig. IV.14-a) and when a degradation profile is used (Fig. IV.14-b). As in the 2D example, the magnetic flux density is lower near the punching edge. It can be noticed that the volume and morphology of the impacted areas are different.

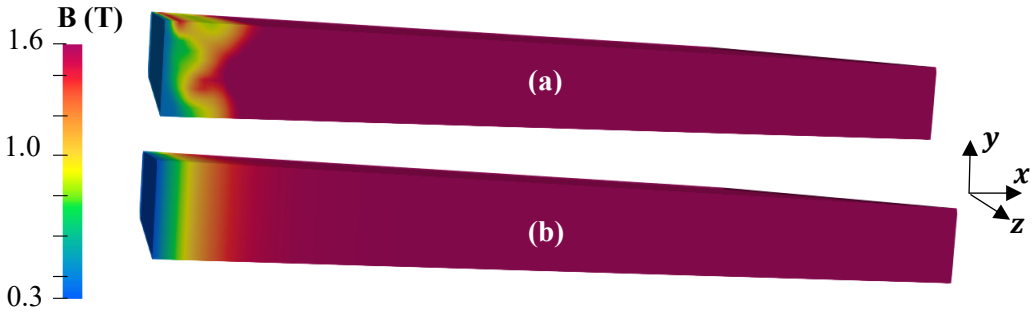

Fig. IV.14 Magnetic flux density distribution in the steel sheet considering (a) the full plastic strain distribution and (b) the degradation profile.

The difference in terms of magnetic flux density magnitudes between the two methods is plotted in Fig. IV.15 where the difference reaches 0.5 T in some regions.

Fig. IV.15 Difference between magnetic flux density distribution obtained with the full plastic strain distribution and the degradation profile.

To assess this difference from the modelling point of view, the magnetic energy is analyzed. The relative increase δ in the total magnetic energy for different imposed magnetic flux magnitudes is calculated as expressed in (IV.4).

$$\delta = (E_d - E_0)/E_0 \qquad \text{(IV.4)}$$

where E_d and E_0 represent the magnetic energy with and without considering the punching effect, respectively. Quantities δ_{FS} and δ_{DP} (Fig. IV.16) refer to the increase of the magnetic energy when the full strain (FS) distribution is considered, and when the degradation profile (DP) is used, respectively. Their evolution is presented with respect to the average magnetic flux density (imposed magnetic flux divided by the sample cross section).

Figure IV.16 gives the evolution of δ_{FS} and δ_{DP} for different imposed magnetic flux densities. As expected, because the magnetic flux is imposed, the magnetic energy increases when the material properties are degraded. The behavior of both δ_{FS} and δ_{DP} with respect to the magnetic flux density is explained by the plastic strain effect that is relatively lower for magnetic flux densities located in the linear zone of BH curves (cf. chapter II). A maximum is reached at intermediate flux densities and becomes negligible in the saturation zone.

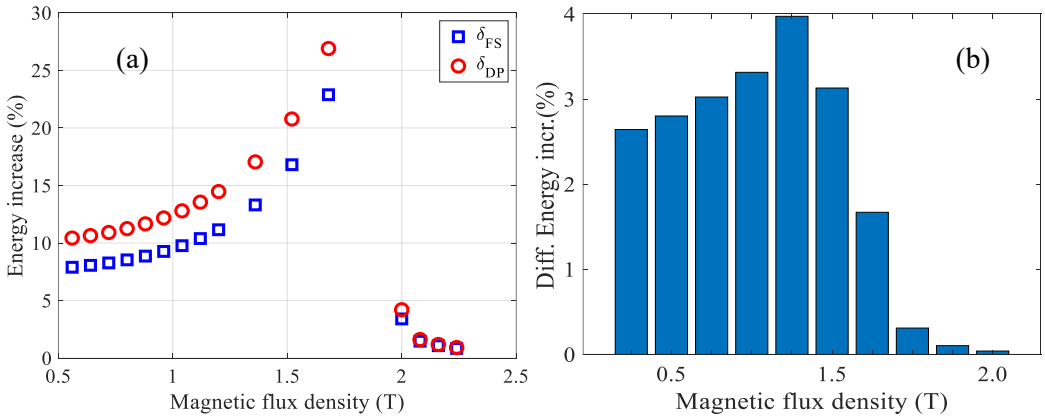

Fig. IV.16 Evolution of δ_{FS} and δ_{DP} for different imposed magnetic flux (b) Difference $\delta_{DP} - \delta_{FS}$

Although δ_{FS} and δ_{DP} show the same behavior, δ_{DP} has higher amplitude. The difference $(\delta_{DP} - \delta_{FS})$ given in Fig. IV.16-b is due to the difference in the magnetic flux density distribution (Fig. IV.15) where the volumes of the impacted areas are different for two methods. Thus, δ_{FS} and δ_{DP}, as well as their difference, are function of the magnetic flux density. Furthermore, the approximation of the "degradation profile" defined by the average value of the strain at each position from the edge does not reflect the real plastic strain distribution in the steel sheet depth.

Now, the effect of the distance between two parallel punched edges on the evolution of δ_{FS} and δ_{DP} is analyzed. Indeed, in practical applications, the impact of cutting edges on the global behavior of a device will be more or less significant depending on the distance between parallel cutting edges. Especially, for small electrical machines, the narrow dimensions of teeth and/or stator yokes require to assess such impact with accuracy. From the mechanical simulation results, the developed Matlab® function allows to generate steel sheets with different widths for the magnetic simulation. Fig IV.17 presents the mesh transformation.

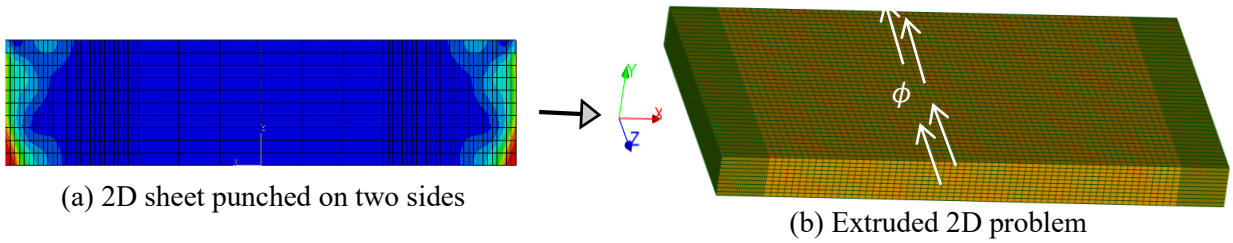

(a) 2D sheet punched on two sides

(b) Extruded 2D problem

Fig. IV.17 Transformation of the 2D sheet punched on two sides to an extruded 2D problem (3D)

The degradation profile corresponding to the sheet punched on two sides is given in Fig. IV.18. It is also calculated based on the results of the punching simulation for the sheet thickness t =0.5mm.

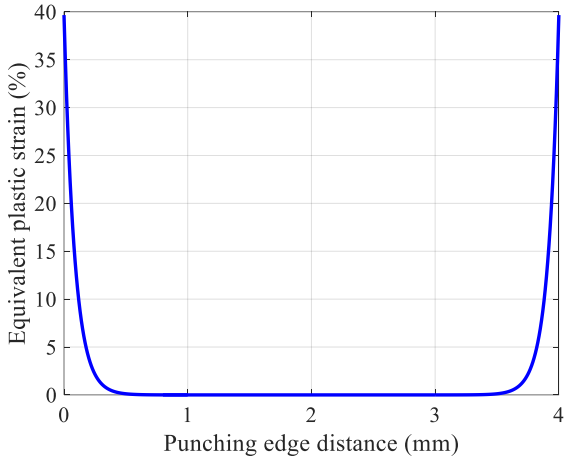

Fig. IV.18 Degradation profile for steel sheet punched on two sides, sheet thickness t =0.5mm

The magnetic flux density when the full plastic strain distribution is considered and when a degradation profile is used are given in Fig IV.19. The degradation is near the punching edges and the morphologies of the impacted areas are different.

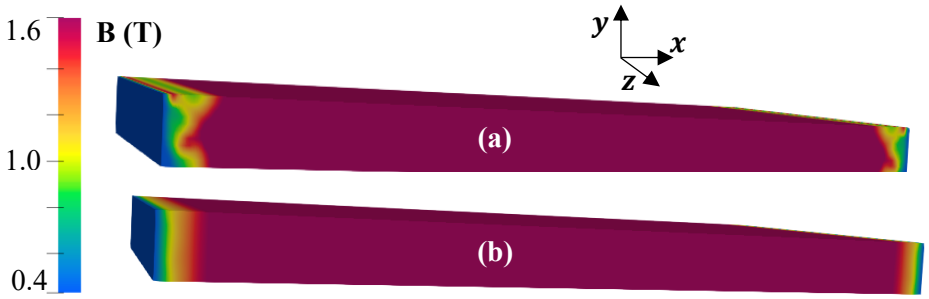

Fig. IV.19 Degradation profile for steel sheet punched on two sides, sheet thickness t = 0.5mm

The average magnetic flux density is kept fixed at around 1.4 T. Then the analysis is carried out for different sheet widths. The results given in Fig. IV.20 show that for small widths where the impacted area occupies a significant proportion of the total sheet volume, δ_{DP} is significantly higher than δ_{FS}. As expected, the difference between both methods becomes minor for large widths as the impacted region becomes smaller with regard to the sheet volume.

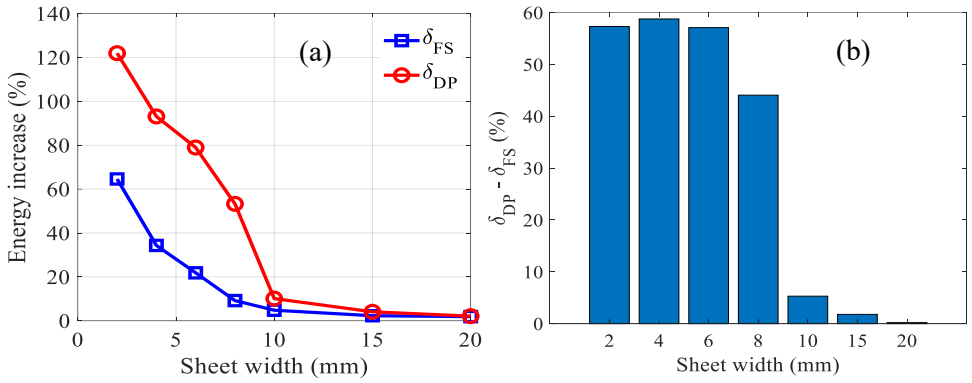

Fig. IV.20 (a) Evolution of the magnetic energy increase due to the punching effect for different sheet widths punched on two sides. (b) Difference in increase of magnetic energy $\delta_{DP} - \delta_{FS}$

This result shows the importance of the method considered to account for the plastic strain distribution in the magneto-mechanical simulations. Indeed, the degradation profile shows a height discrepancy compared to the full strain distribution for the small sheet widths. Thus, in the next section the analysis will be carried out on a concrete example, a small tooth of an electrical machine.

IV.2.2 Finite element analysis – Tooth of an electrical machine

To perform the analysis, a punching process simulation of the tooth of a small power electrical machine has been carried out.

- ***Punching simulation of a tooth of an electrical machine***

The punching simulation concerns a typical tooth of a small electrical machine. The dimensions correspond to a real industrial machine where the stator yoke thickness is $d_y = 5$ mm, the average tooth body width is $\tau = 2$ mm. In order to reduce the computational time, the simulation is performed on the half tooth as illustrated in Fig. IV.21, then the complete geometry is generated by symmetry.

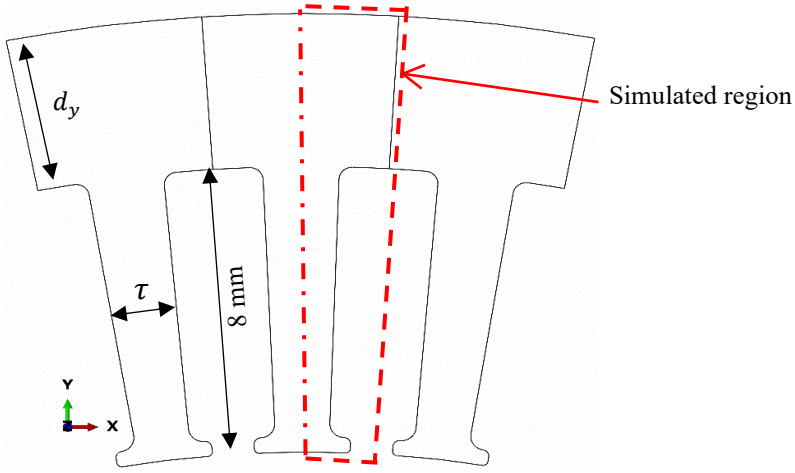

Fig. IV.21 Geometry of the simulated tooth

Unlike the punching simulation of the steel sheet, which was performed in 2D, the tooth of the electrical machine has a complex geometry, which contains both straight and curved edges, and requires a 3D simulation of the cutting. Fig IV.22 gives the geometry of the simulated mechanical problem.

The material characteristics and the punching process parameters are those used in chapter III section III.3.1.2 (Tab. III.2), and section III.3.2 (Tab. III.3). The sheet thickness and the punch-die clearance are $t = 0.35$ mm and $c = 8$ %, respectively. The punch tool, the holder and the die are designed to cut the shape of a half of the tooth. They are modeled with rigid parts. The punching of the straight part of the tooth tip is simulated separately using a straight punch tool.

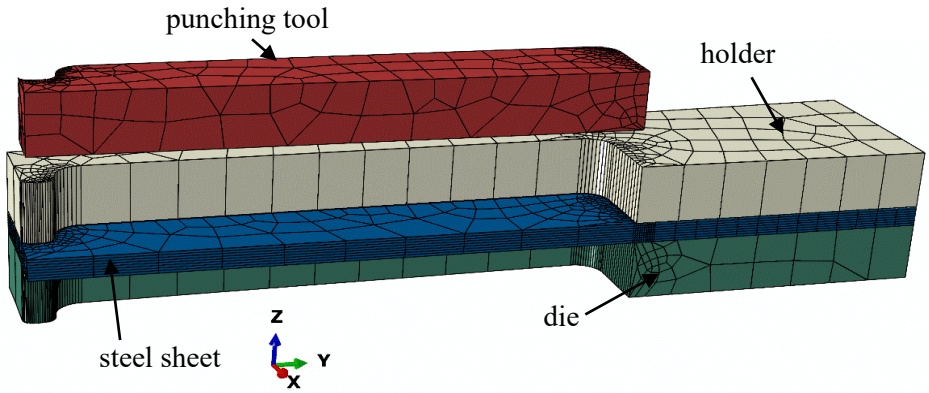

Fig. IV.22 Geometry of punching process simulation of the tooth

Fig. IV.23 gives the punching simulation result; it presents the distribution of the equivalent plastic strain in the simulated half tooth. We observe that the plastic strain is localized at the cutting edge with heterogeneous levels along the cutting edge.

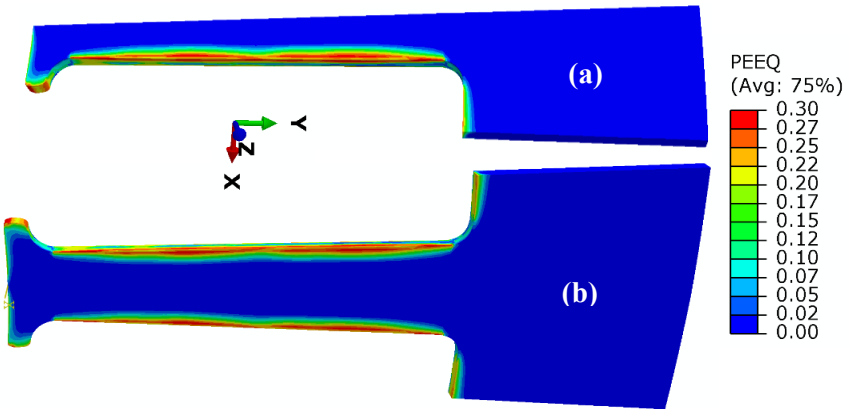

Fig. IV.23 Distribution of the equivalent plastic strain in (a) half tooth, (b) whole tooth

The magnetostatic problem is considered with the imposition of the magnetic flux between the tip (entry) of the tooth and the lateral sides (exit) of the yoke (Fig. IV.24). The imposed average magnetic flux density is about B=1.5 T.

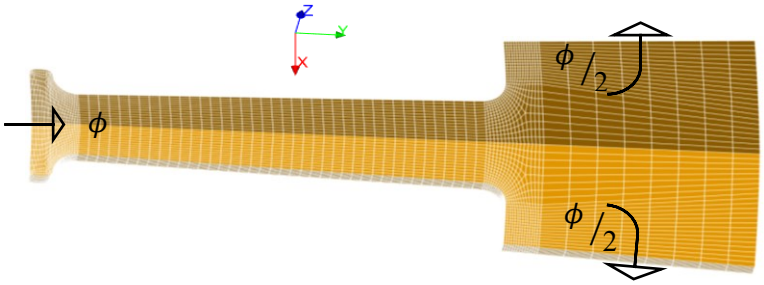

Fig. IV.24 Illustration of the imposed magnetic flux circulation in the tooth of electrical machine

Figure IV.25 gives the magnetic flux density distribution considering the full plastic strain distribution and the degradation profile. The difference between both distributions is not obvious to distinguish from one another. However, the analysis in terms of magnetic energy shows a great disparity with $\delta_{FS} = 87\%$ and $\delta_{DP} = 180$ %. This result confirms the behavior investigated in the steel sheet and shows that the way the degradation profile is determined should be carefully considered to have a realistic representation of the global magnetic behavior.

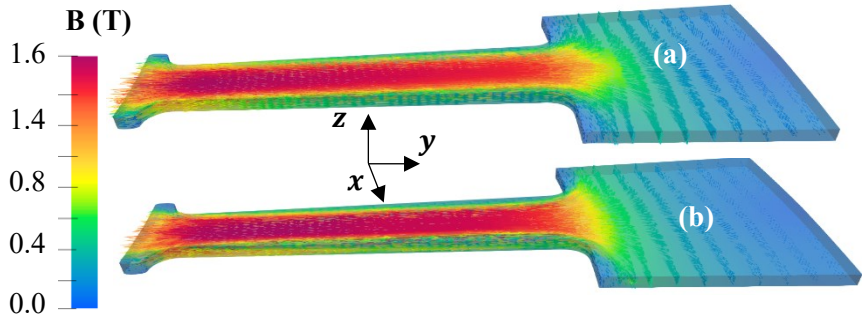

Fig. IV.25 Magnetic flux density in the tooth considering (a) the full plastic strain distribution (b) the

Indeed, depending on the magnetic flux density amplitude and the dimensions of the simulated problem, the magneto-mechanical behavior varies substantially. However, the use of the full plastic strain to simulate an electrical machine would lead to a significant computation time as it requires a fine mesh along the punching edges. In that context, a degradation profile is more practical, but improvements are still needed in order to be closer to the reference behavior (full plastic strain distribution).

IV.3 Analysis of the degradation profile choice

Based on the result obtained with the reference example (steel sheet), where it has been shown that the magneto-mechanical behavior is function of the magnetic flux density, we propose, as a first approach, the adjustment of the degradation profile. Instead of the average strain, the degradation profile is estimated by the weighted average strain ε_{ω_j} as follows: the calculation method has been explained in section III.4.1 (Fig III.14).

$$\varepsilon_{\omega_j} = \frac{\sum_{i=1}^{n} \omega_{i,j}\, \varepsilon_{i,j}}{\sum_{i=1}^{n} \omega_{i,j}} \tag{IV.5}$$

As a first approach to determine the weighting coefficients, we rely on the experimental observation associated to the attenuation of the degradation with increasing plastic strain level. Then, we chose to set the weighting coefficient (IV.6) as the relative permeability $\mu_r(\varepsilon, B_{imposed})$ calculated for each strain value for a given magnetic flux density $B_{imposed}$. In equation (IV.6) the quantity $H_{i,j}$ is the corresponding magnetic field calculated using the Sablik model.

$$\omega_{i,j} = \mu_r = \frac{B_{imposed}}{\mu_0 H_{i,j}} \tag{IV.6}$$

Figure IV.26 illustrates the estimation of the weighting coefficients where $B_{imposed}$ corresponds to the imposed magnetic flux during the analysis. It is noted that this weighting method considers $B_{imposed}$ in the linear zone of the BH curves.

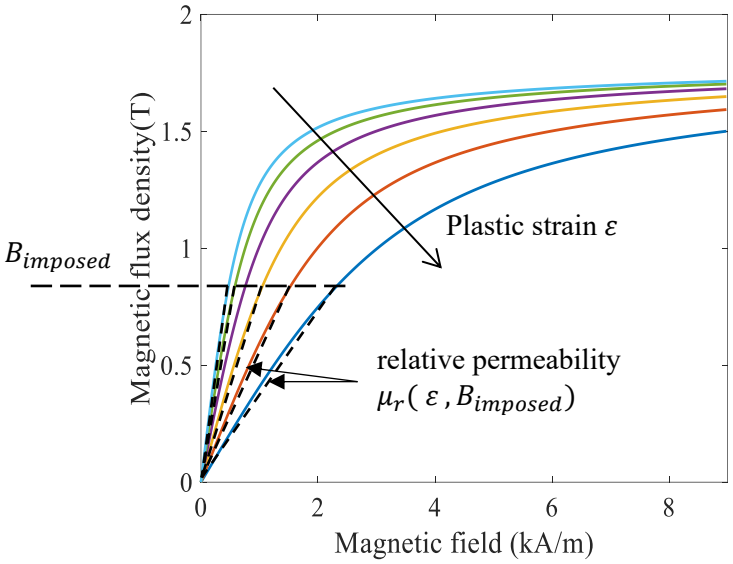

Fig. IV.26 Calculation method of the weighted degradation $\omega_{i,j}$

The weighted degradation profile (w.DP) is estimated using the punching simulation result of the sheet thickness t =0.5mm.

Figure IV.27 gives a comparison between the average degradation profile calculated using (III.36), and the proposed weighted degradation profile calculated with (IV.5). Besides the fact that the profiles present different amplitudes, the w.DP cannot be fitted with good accuracy using an exponential function as for the average degradation profile. Thus, the equation (IV.7) has been used to fit the calculated values.

$$\varepsilon_w = \sum_{i=1}^{3} a_{w_i} . \exp\left(-\left(\frac{x - b_{w_i}}{c_{w_i}}\right)^2\right) \tag{IV.7}$$

where a_{w_i}, b_{w_i}, and c_{w_i} are the fitting parameters, with $i = (1,2,3)$. Their values are given in Tab. IV.5.

Tab. IV.5 Fitted parameters of the weighted degradation profile

Parameter	$i = 1$	$i = 2$	$i = 3$
a_{w_i}	2242	-38.33	-2185
b_{w_i}	3.979×10^{-5}	3.237×10^{-5}	4.282×10^{-5}
c_{w_i}	0.000143	6.571×10^{-5}	0.0001414

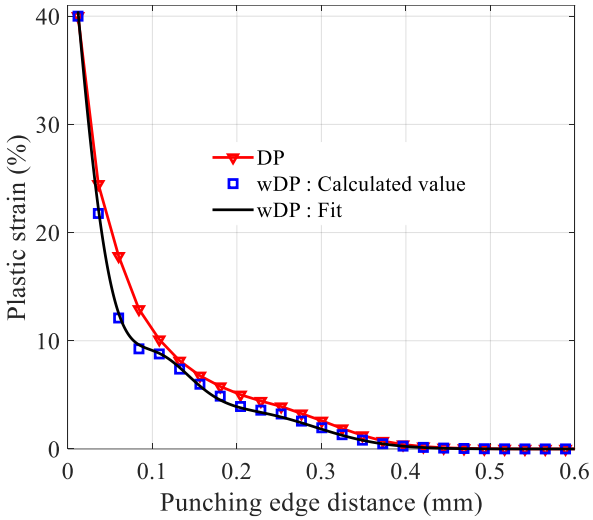

Fig. IV.27 Average degradation profile (DP) and weighted degradation profile (w.DP)

To evaluate the ability of the weighted degradation profile to approach the full plastic strain from the modeling point of view, the magnetic energy analysis carried out previously in section IV.2.1 is performed again. For different imposed magnetic flux magnitudes located in the linear zone of the BH curves, the energy increase is calculated using (IV.4). δ_{wDP} refers to the increase of the magnetic energy when the weighted degradation profile is considered.

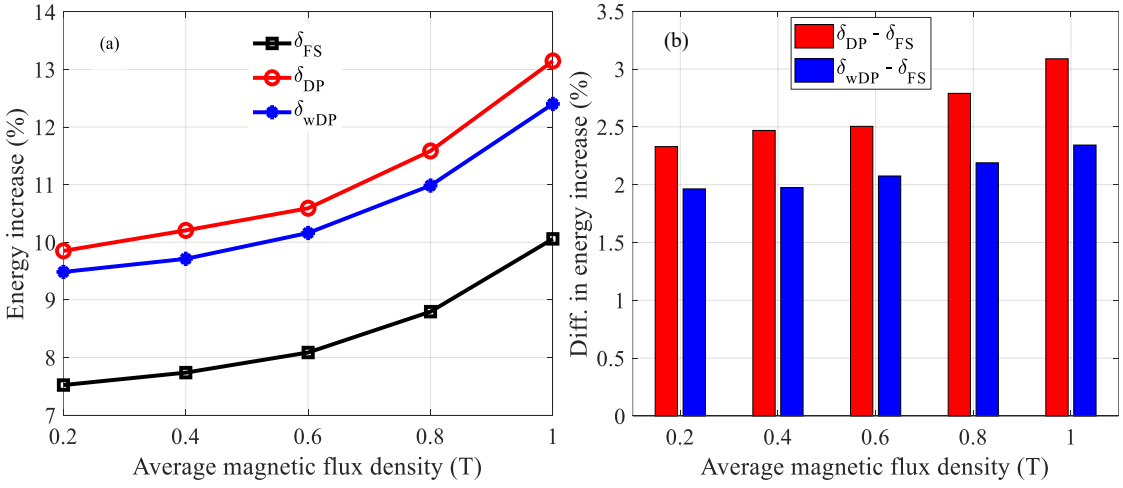

Fig. IV.28 (a) Evolution of δ_{FS}, δ_{DP} and δ_{wDP} for different imposed magnetic flux densities (b) difference in energy increase: $\delta_{DP} - \delta_{FS}$ and $\delta_{wDP} - \delta_{FS}$

Figure IV.28 gives the evolution of the magnetic energy increase for different imposed magnetic flux densities, the introduction of the weighted degradation profile allowed to better approach the full plastic strain behavior. Thus, Fig IV.28-b gives the difference in energy increase $\delta_{DP} - \delta_{FS}$ and $\delta_{wDP} - \delta_{FS}$. For example, when $B_{imposed} = 1$ T, the difference in energy increase between the degradation profile and the full plastic strain (reference) is 3.08%, while the difference is 2.34% when the weighted degradation profile is considered instead of the "classic" degradation profile.

IV.4 Conclusion

Using the magneto-mechanical Sablik model and strain-dependent loss parameters, the impact of the punching process on the magnetic properties has been investigated. Although the preliminary analysis of the synchronous machine was performed with the degradation profile for achieving some realistic computational time, it shows a significant increase of iron loss, about 38 %. If we consider the result of the analysis carried out in section IV.2, the value of iron loss is certainly overestimated. Indeed, it has been shown that the degradation profile defined by the average value of the strain at each position from the edge does not reflect the real plastic strain distribution in the steel sheet depth. Depending on the magnetic flux density amplitude and the dimensions of the simulated problem, the magneto-mechanical behavior varies substantially. However, the use of the full plastic strain to simulate an electrical machine would lead to a significant computation time as it requires a fine mesh along the punching edges. In that context, a degradation profile is more practical, but improvements are still needed in order to be closer to the reference behavior (full plastic strain distribution). As first approach, an adjustment of the degradation profile based on the experimental observations has been proposed and applied to the steel sheet case. For each plastic strain value, a weighting coefficient based on the relative permeability have been introduced. It allowed to reduce the difference between the degradation profile and the full strain distribution by 20%. However, this proposition should be improved since the ponderation coefficients have been calculated by considering an imposed magnetic flux density in the linear zone.

Conclusion and perspectives

1. Conclusion

In this thesis the analysis of the effect of manufacturing processes on magnetic properties of materials has been carried out. A particular attention has been given to the effect of the mechanical punching process.

In the first chapter, beside the presentation of theoretical background necessary to understand the subject of the thesis, the physical effects on the magnetic properties, due to the manufacturing processes, have been reviewed. We focused on the impact of mechanical punching on the magnetic behavior and iron losses. A distinction is made between magneto-elastic coupling which is related to the phenomenon of magnetostriction and magneto-plastic coupling which is characterized by the increase of the dislocation density as the plastic deformation increases, which considerably affects the magnetic properties. Different approaches of magneto-mechanical modeling have been presented. The Sablik model has been chosen to model the mechanical punching effect on the anhysteretic magnetic behavior. It presents the advantage to have a physical basis which allows its generalization. Also, the use of macroscopic quantities makes its identification as well as its implementation in numerical tools relatively acceptable.

In the second chapter, the modifications made to the Sablik model and its identification process have been presented. There are three distinct steps to follow during the identification of the Sablik model parameters. First, without considering the stress dependence, the initial parameters of the model are identified. Second, the elastic stress dependence is considered and the parameters of the magnetostriction function are identified. Finally, the plastic dependency is introduced, and its parameters identified. The D-H equivalent stress introduced to consider the multiaxial stress, has been validated. The introduction of the modified Brillouin function to model the anhysteretic magnetization instead of the Langevin function is interesting the magnetoelastic coupling. Indeed, it improves the accuracy fitting which allowed to have a better modeling of the magnetostrictive behavior. Furthermore, the identification method based only on macroscopic magnetization curves measured under compressive and tensile stress was quite simple and gives a good estimation of the magnetostriction. However, when the plastic dependence is introduced, the fitting accuracy of the modified Brillouin function seems less efficient.

In the third chapter, the complete simulation chain of the effect of punching process on magnetic properties has been performed. First, a FE magnetostatic problem has been presented, then a mechanical punching simulation of a steel sheet allowed to define plastic strain distribution near the punching edge. Finally, to interface both physics, the Padé approximation has been used to inverse the Sabilk model that accounts for the plastic strain. The magnetic behavior of a steel sheet, where a strong degradation of the magnetic flux density near the punching edge has been shown.

In the fourth chapter the impact of punching process on the magnetic properties has been investigated. The preliminary analysis of the synchronous machine performed with the degradation profile showed a significant increase of iron losses, about 38 %. However, this result is probably over-estimated as the analysis of the method used to account for the plastic strain in the magneto-

mechanical simulation showed that the degradation profile, defined by the average value of the strain at each position from the edge, is more detrimental than the consideration of the full plastic strain. Indeed, the degradation profile approach does not reflect the real plastic strain distribution in the steel sheet depth. We observed that, depending on the magnetic flux density magnitude and the dimensions of the studied device, the magneto-mechanical behavior varies substantially. As a first approach, an adjustment of the degradation profile based on the results obtained with the steel sheet case has been proposed. This approach allowed to reduce the difference between the degradation profile and the full strain distribution by about 20%.

2. Suggestion for future works

- The natural perspective of the proposed work concerns the method used to consider the plastic strain distribution in the magneto-mechanical simulation. As shown in chapter IV, the degradation profile must be adjusted to be closer to the full plastic strain distribution. The proposed correction is function of the plastic strain distribution given by the punching process and the magnetic flux density. Thus, the degradation profile must be evaluated during the FE calculation process.
- Also, the magnetostriction function will be impacted by the plastic strain as already observed in the literature. A proper modeling would be to account for the change in the magnetostriction function depending on the plastic strain. However, given the much more detrimental effect of plastic strain on the magnetic properties, this correction should not affect significantly the results.
- Compared to the Langevin function, the modified Brillouin function showed a good fitting accuracy in the elastic identification. Its integration in the hole Sablik model including the plastic identification should be improved.
- Finally, to complete the investigation of the effect of punching process on the iron loss in the synchronous machine, a validation should be carried out.

Annex A: 2D magnetostatic formulation

The magnetostatic formulation given in (III.16) can be derived for 2D problem, the following hypothesis are considered:

- The problem has a symmetrical plan (*x*O*y*).
- The current density $\boldsymbol{N}_i i$ is defined along z axis and the remanent magnetic flux density $\boldsymbol{B}_r$ and the imposed magnetic flux density $\boldsymbol{N}_\phi \phi$ are defined in the plan (*x*O*y*).
- The studied problem is invariant along z axis.

This allows to express the magnetic field density, the vector potential, and the source terms as

$$\boldsymbol{B} = \begin{pmatrix} B_x \\ B_y \\ 0 \end{pmatrix}, \boldsymbol{A} = \begin{pmatrix} 0 \\ 0 \\ A_z \end{pmatrix}, \boldsymbol{B}_r = \begin{pmatrix} B_{rx} \\ B_{ry} \\ 0 \end{pmatrix}, \boldsymbol{N}_i i = \begin{pmatrix} 0 \\ 0 \\ N_{iz} \end{pmatrix} i \text{ and } \boldsymbol{N}_\phi \phi = \begin{pmatrix} N_{\phi x} \\ N_{\phi y} \\ 0 \end{pmatrix} \phi \tag{A.1}$$

Then, the potential $\boldsymbol{A}$ is discretized by the nodal elements of the 2D mesh as

$$A_z = \sum_{n=1}^{N_n} a_n w_n^0 \tag{A.2}$$

and each function w_n^0 is taken as weighting function ψ in (III.16). By considering these assumptions, the rotational of $\boldsymbol{A}$ can be expressed as in (A.3)

$$\boldsymbol{curl}\, \boldsymbol{A} = \begin{pmatrix} \frac{\partial}{\partial x} \\ \frac{\partial}{\partial y} \\ \frac{\partial}{\partial z} \end{pmatrix} \wedge \begin{pmatrix} 0 \\ 0 \\ A_z \end{pmatrix} = \begin{pmatrix} \frac{\partial A_z}{\partial y} \\ -\frac{\partial A_z}{\partial x} \\ 0 \end{pmatrix} \tag{A.3}$$

Then, the rotational operator can be rewritten in 2D as

$$\boldsymbol{curl}_{2D} U = \begin{pmatrix} \frac{\partial U}{\partial y} \\ -\frac{\partial U}{\partial x} \end{pmatrix} \tag{A.4}$$

In these conditions, the terms of the matrix $[M]$ presented in (III.28) can be rewritten such as

$$\mathrm{M}_{ij} = \int_{D_e} \mathcal{F}^{-1}(\boldsymbol{B})\boldsymbol{curl}_{2D}\, w_i^0 \cdot \boldsymbol{curl}_{2D}\, w_j^0\, dv \quad = \int_{D_e} \mathcal{F}^{-1}(\boldsymbol{B})\boldsymbol{grad}_{2D}\, w_i^0 \cdot \boldsymbol{grad}_{2D}\, w_j^0\, dv$$

$$\forall\, (i,j) = \{1,..N_n\}^2 \tag{A.5}$$

with $\boldsymbol{grad}_{2D}$ the gradient operator defined in the plan (xOy).

To impose a magnetic flux ϕ flowing through boundaries Γ_{h1} and Γ_{h2} of the 2D studied domain, the source term $\boldsymbol{N}_\phi$ can be derived from a scalar function α_ϕ. This latter is equal to one on a boundary Γ_b connected to Γ_{h1} and Γ_{h2} and to zero elsewhere. Then, we have

$$\boldsymbol{N}_\phi = \boldsymbol{curl}_{2D}\alpha_\phi \tag{A.6}$$

Finally, the terms of the vector $[F]$ presented in (III.29) can be rewritten such as

$$\mathrm{F}_j = \int_{D_e} (N_{iz}\, i)\cdot w_j^0\, dv - \int_{D_e} \mathcal{F}^{-1}(\boldsymbol{B})\phi\, \boldsymbol{grad}_{2D}\alpha_\phi \cdot \boldsymbol{grad}_{2D}\, w_j^0\, dv$$

$$+ \int_{D_e} \mathcal{F}^{-1}(\boldsymbol{B})\boldsymbol{B}_r \cdot \boldsymbol{curl}_{2D}\, w_j^0\, dv \qquad \forall\, j = 1,..N_n \tag{A.7}$$

References

[1] Waide, P. and Brunner, "Energy-efficiency policy opportunities for electric motor-driven systems", *International Energy Agency,* 2011.

[2] N. Boubaker, *et al*, "Measurements of iron loss in pmsm stator cores based on cofe and sife lamination sheets and stemmed from different manufacturing processes," *IEEE Trans. Magn.*, vol. 55, no. 1, pp. 1–9, Jan 2019.

[3] Jiles D, "Introduction to Magnetism and Magnetic Materials", *Springer science*, First edition ISBN 978-0-412-38640-4, 1991.

[4] Cullity B. D., Graham C. D, "Introduction to Magnetic Materials", *Institute of Electrical and Electronics Engineers, Inc*, ISBN 978-0-471-47741-9, 2009, USA.

[5] A. Hubert and R. Schafer, "Magnetic domains", *ed. Springer*, 1998, Berlin.

[6] D. Singh, "Effect of Stress on Magnetic Properties of Electrical Steel Sheet and Core Losses in Electrical Machines," Phd thesis, Aalto University, 2016, Finland.

[7] M. Borsenberger, " Contribution à l'identification de l'interaction paramètres procédés – propriétés d'emploi des produits : Application au forgeage et aux propriétés électromagnétiques d'une roue polaire d'alternateur", PhD Thesis, École Nationale Supérieure d'Arts et Métiers, 2018, France.

[8] Lours P., "Au cœur des matériaux cristallins", *Presses des Mines Ed*., ISBN 978-2-35671-370-4, 2016, France.

[9] ISO 6892-1:2009(E), « Metallic materials – Tensile Testing-Part 1: Method of test at room temperature. », 2009.

[10] I. Farooq, "Difference between rockwell, brinell, vickers and knoop hardness test".

[11] Gong J., Miao H., Peng Z., "Analysis of the nanoindentation data measured with a Berkovich indenter for brittle materials: effect of the residual contact stress", *Acta Mater.,* 52 (3), 785-793, 2004.

[12] Kermouche G., Barthel E., Vandembroucq D., Dubujet Ph., "Mechanical modelling of indentation-induced densification in amorphous silica". *Acta Mater*., 56 (13), 3222-3228, 2008.

[13] O. Hubert and E. Hug. "Influence of plastic strain on magnetic behavior of nonoriented 3%Si-Fe and application to manufacturing test by punching". *Materials Science and Technology*, 11 :482-487, 1995.

[14] M. Takazewa, K. Kitajima, Y. Morimoto, J. Yamasaki, C. Kaido, "Effect of Strain by Mechanical Punching on Nonoriented Si-Fe Electrical Sheets for a None-Slot Motor Core", IEEE Trans. Magn., vol. 42, no. 10, pp. 2790 – 2792, 2006.

[15] H. Naumoski, A. Maucher, L. Vandenbossche, S. Jacobs, U. Herr, and X. Chassang, "Magneto-optical and field-metric evaluation of the punching effect on magnetic properties of electrical steels with varying alloying content and grain size," in *2014 4th International*

Electric Drives Production Conference (EDPC), Sep. 2014.

[16] F. Ossart, E. Hug, O. Hubert, C. Buvat, and R. Billardon, "Effect of punching on electrical steels: Experimental and numerical coupled analysis," *IEEE Transactions on Magnetics*, vol. 36, no. 5, pp. 3137–3140, Sep. 2000.

[17] X. Xiong, S. Hu, K. Hu, and S. Zeng, "Texture and magnetic property evolution of non-oriented Fe–Si steel due to mechanical cutting," *Journal of Magnetism and Magnetic Materials*, vol. 401, pp. 982–990, Mar. 2016.

[18] A. Saleem, N. Alatawneh, R. R. Chromik, and D. A. Lowther, "Effect of Shear Cutting on Microstructure and Magnetic Properties of Non-Oriented Electrical Steel," *IEEE Transactions on Magnetics*, vol. 52, no. 5, pp. 1–4, May 2016.

[19] K. H. Schmidt, "Influence of punching on the magnetic properties of electric steel with 1% silicon," *Journal of Magnetism and Magnetic Materials*, vol. 2, nos. 1–3, pp. 136–150, Dec. 1975.

[20] P. Baudouin, M. De Wulf, L. Kestens, and Y. Houbaert, "The effect of the guillotine clearance on the magnetic properties of electrical steels," *Journal of Magnetism and Magnetic Materials*, vol. 256, nos. 1–3, pp. 32–40, 2003.

[21] Schoppa, A., Schneider, J. and Roth, J.O., "Influence of the cutting process on the magnetic properties of non-oriented electrical steels", *Journal of Magnetism and Magnetic Materials* 215-216, 100 – 102, 2000.

[22] H. M. S. Harstick, M. Ritter, A. Plath, and W. Riehemann, "EBSD investigations on cutting edges of non-oriented electrical steel," *Metallogrgy. Microstruct. Anal.*, vol. 3, no. 4, pp. 244–251, 2014.

[23] R. Siebert, J. Schneider, and E. Beyer, "Laser cutting and mechanical cutting of electrical steels and its effect on the magnetic properties," *IEEE Transactions on Magnetics*, vol. 50, no. 4, Apr. 2014.

[24] H. Naumoski, B. Riedmüller, A. Minkow, and U. Herr, "Investigation of the influence of different cutting procedures on the global and local magnetic properties of non-oriented electrical steel," *Journal of Magnetism and Magnetic Materials*, vol. 392, pp. 126–133, 2015.

[25] H. Toda, Y. Zaizen, M. Namikawa, N. Shiga, Y. Oda, and S. Morimoto, "Iron loss deterioration by shearing process in non-oriented electrical steel with different thicknesses and its influence on estimation of motor iron loss," *IEEJ J. Ind. Appl.*, vol. 3, no. 1, pp. 55–61, Jan. 2014.

[26] T. Omura, Y. Zaizen, M. Fukumura, K. Senda, and H. Toda, "Effect of hardness and thickness of nonoriented electrical steel sheets on iron loss deterioration by shearing process," *IEEE Trans. Magn.*, vol. 51, no. 11, Nov. 2015, Art. no. 2005604.

[27] A. Schoppa, J. Schneider, and J.-O. Roth, "Influence of the cutting process on the magnetic properties of non-oriented electrical steels," *J. Magn. Magn. Mater.*, vols. 215–216, pp. 100–102, Jun. 2000.

[28] R. Rygal, A. J. Moses, N. Derebasi, J. Schneider, and A. Schoppa, "Influence of cutting stress on magnetic field and flux density distribution in non-oriented electrical steels," *J. Magn. Magn. Mater.*, vols. 215–216, pp. 687–689, Jun. 2000.

[29] S. Subramonian, T. Altan, B. Ciocirlan, and C. Campbell, “Optimum selection of variable punch-die clearance to improve tool life in blanking non-symmetric shapes,” *Int. J. Mach. Tools Manuf.*, vol. 75, pp. 63–71, Dec. 2013.

[30] Z. Wang, S. Li, R. Cui, X. Wang, and B. Wang, “Influence of Grain Size and Blanking Clearance on Magnetic Properties Deterioration of Non-Oriented Electrical Steel,” *IEEE Transactions on Magnetics*, vol. 54, no. 5, pp. 1–7, May 2018.

[31] V.-E. Iordache, “Suivi de l’état de contraintes, appliquées et internes, des alliages ferromagnétiques doux par mesure de leur propriétés magnétiques”, PhD thesis, UTC Compiègne University, 2003, France.

[32] R. Rygal, A.J. Moses, N. Derebasi, J. Schneider, A. Schoppa, “Influence of cutting stress on magnetic field and flux density distribution in non-oriented electrical steels,” *J. Magn. Magn. Mater*.687–689, 2000.

[33] T. Nakata, M. Nakano, K. Kawahara, Effects of stress due to cutting on magnetic characteristics of silicon steel, *IEEE Transl. J. Magn*. Jpn. 6,453–457, 1992

[34] H. Cao, L. Hao, J. Yi, X. Zhang, Z. Luo, S. Chen, R. Li, “The influence of punching process on residual stress and magnetic domain structure of non-oriented silicon steel,” *Journal of Magnetism and Magnetic Materials*, vol. 406, pp. 42–47, May 2016.

[35] A. Ben Ismail, M. Rachik, P.E. Mazeran, M. Fafard, and E. Hug, “Material characterization of blanked parts in the vicinity of the cut edge using nanoindentation technique and inverse analysis,” *International Journal of Mechanical Sciences*, vol. 51, no. 11–12, pp. 899–906, Nov. 2009.

[36] Casals O, Alcala J. “The duality in mechanical property extractions from Vickers and Berkovich instrumented indentation experiments”. *Acta Materialia*, 53:3545–61, 2005.

[37] Kucharski S, Mroz Z. “Identification of yield stress and plastic hardening parameters from a spherical indentation test”. *International Journal of Mechanical Sciences*, 49:1238:1250, 2007.

[38] H. A. Weiss *et al.*, “Influence of shear cutting parameters on the electromagnetic properties of non-oriented electrical steel sheets,” *Journal of Magnetism and Magnetic Materials*, vol. 421, pp. 250–259, Jan. 2017.

[39] Ali, K. *et al*, “Prediction of mechanical stress effects on the iron loss in electrical machines”, *Journal of applied physics,* 81(8), 4119–4121, 1997.

[40] Yamazaki, K. and Takeuchi, H., “Impact of mechanical stress on characteristics of interior permanent magnet synchronous motors”, *IEEE Transactions on Industry Applications* 53(2), 963–970, 2017.

[41] J.P. Joule, "On the effects of magnetism upon the dimensions of iron and steel bars", *Philosophical Magazine*, 30, p76, 1847.

[42] E. Du Trémolet de Lacheisserie, “Magnetism - Fundamentals, Materials and Applications”, *ed. Springer*, N.Y. 2002.

[43] M.Fall. “Mesure et modélisation multiéchelle du comportement thermo-magnéto-mécanique des alliages à mémoire de forme”. PhD thesis, Paris-Saclay University, 2017.

[44] O. Hubert, L. Daniel and R. Billardon, "Experimental analysis of the magnetoelastic anisotropy of a non-oriented silicon iron alloy", *Journal of Magnetism and Magnetic Materials*, 254-255, p352, 2003.

[45] O. Hubert, "Experimental analysis of the magnetoelastic anisotropy of a non-oriented silicon iron alloy", proceedings of the 15th Soft Magnetic Materials conference, Bilbao, 2003.

[46] D. Singh, F. Martin, P. Rasilo, and A. Belachen, "Magnetomechanical Model for Hysteresis in Electrical Steel Sheet," *IEEE Transactions on Magnetics*, vol. 52, no. 11, pp. 1–9, Nov. 2016.

[47] R.M. Bozorth, "Ferromagnetism", *ed. D. Van Norstand Company*, N.Y. 1951.

[48] Otmane Lahyaoui, "Contribution to the study of magnetostrictive energy conversion: from material to device. Electric power", PhD thesis, Université de Technologie de Compiègne, France, 2019.

[49] M. El Youssef, "Impact du procédé de fabrication des stators slinky sur les propriétés des matériaux", PhD thesis, Arts et Métiers ParisTech, France, 2017.

[50] R. Billardon, L. Hirsinger, and F. Ossart. "Magneto-elastic coupled finite element analyses", *Revue Européenne des Eléments Finis*, 8 n.5-6 :525-551, 1999.

[51] IEC: 60404-2, International Electrotechnical Commission, *Magnetic materials.* Geneva, 2008.

[52] IEC: 60404-3, Methods of measurement of the magnetic properties of electrical steel sheet and strip by means of a single sheet tester, Geneva, 2000.

[53] Sievert, J., 'Two-dimensional magnetic measurements-history and achievements of the workshop', *Przeglad Elektrotechniczny* R. 87(9b), 2–10, 2011.

[54] Zouzou, S., Kedous-Lebous, A. and Brissonneau, P., 'Magnetic properties under unidirectional and rotational field', J. *Magn. Magn. Mater*. 112(1-3), 106–108, 1992.

[55] Bottauscio, O., Chiampi, M., Fiorillo, F. and Manzini, A., "Space and time distribution of magnetic field in 2D magnetizers", *Przeglad Elektrotechniczny* R. 81(5), 8–12. 2005.

[56] U. Aydin, "Multiaxial Magneto-Mechanical Interactions in Electrical Steel Sheets," PhD thesis, Aalto University, 2018, Finland.

[57] N. Buiron, "Modélisation multiéchelle du comportement magnéto-élastique couplé des matériaux ferromagnétiques doux"., Phd thesis, Ecole Normale Supérieure de Cachan, 2000, France.

[58] L. Daniel, "Modélisation multi-échelle du comportement magnéto-mécanique des matériaux ferromagnétiques textures", Phd thesis, Ecole Normale Supérieure de Cachan, 2003.

[59] Vanoost, D., Steentjes, S., Peuteman, J., Gersem, H. D., Pissoort, D. and Hameyer, K., "Multiscale and macroscopic modeling of magneto-elastic behavior of soft magnetic steel sheets", *Int. J. Numer*. *Model*. 31(2), 1–9, 2017.

[60] Daniel, L., Rekik, M. and Hubert, O., "A multiscale model for magnetoelastic behaviour including hysteresis effects", *J. Arch. App. Mech*. 84(9- 11), 1307–1323, 2014.

[61] Bernard, L., Mininger, X., Daniel, L., Krebs, G., Bouillault, F. and Gabsi, M., "Effect of stress on switched reluctance motors: A magneto-elastic finite element approach based on multiscale constitutive laws", *IEEE Trans. Magn*. 47(9), 2171–2178, 2011.

[62] Bernard, L. and Daniel, L., “Effect of stress on magnetic hysteresis losses in a switched reluctance motor: application to stator and rotor shrink fitting”, *IEEE Trans. Magn*. 51(9), 7002513, 2015.

[63] Daniel, L., Hubert, O. and Rekik, M., “A simplified 3-D constitutive law for magnetomechanical behavior”, *IEEE Trans. Magn*. 51(3), 7300704. 2015.

[64] G Bertotti. “Dynamic generalisation of scalar preisach model of hysteresis”. *IEEE Transactions on Magnetics*, 28 :2599–2601, 1992.

[65] F. S. Mballa Mballa, “Modélisation du comportement magnéto-mécanique d’un acier Dual Phase à partir de sa description microstructurale”, Phd thesis, Ecole Normale Supérieure de Cachan, 2013, France.

[66] A. Sipeky and A. Ivanyi, “Preisach-type stress-dependent magnetic vector hysteresis model,” *Physica B: Condensed Matter*, vol. 403, no. 2, pp. 491–495, Feb. 2008.

[67] D. C. Jiles et D. L. Atherton, « Theory of ferromagnetic hysteresis », *Journal of Magnetism and Magnetic Materials*, vol. 61, n^{o} 1-2, p. 48-60, sept. 1986.

[68] D. C. Jiles, « Theory of the magnetomechanical effect », *Journal of Physics D : Applied Physics*, vol. 28, n^{o} 8, p. 1537-1546, 1993.

[69] D. C. Jiles et D. L. Atherton, « Theory of the magnetisation process in ferromagnets and its application to the magnetomechanical effect », *Journal of Physics D: Applied Physics*, vol 17, n^{o} 6, p. 1265-1281,1984.

[70] M. J. Sablik, T. Yonamine, et F. J. G. Landgraf, « Modeling plastic deformation effects in steel on hysteresis loops with the same maximum flux density », *IEEE Transactions on Magnetics*, vol. 40, n^{o} 5, p. 3219-3226, sept. 2004.

[71] J. Lemaitre, “SECTION 9.1 - Introduction to Coupled Behaviors,” in *Handbook of Materials Behavior Models*, J. Lemaitre, Ed. Burlington: Academic Press, pp. 795–796. 2001.

[72] M. Bali and A. Muetze, “Modeling the Effect of Cutting on the Magnetic Properties of Electrical Steel Sheets,” *IEEE Transactions on Industrial Electronics*, vol. 64, no. 3, pp. 2547–2556, Mar. 2017.

[73] A. Belahcen and A. Arkkio, “Locally coupled magneto-mechanical model of electrical steel,” *COMPEL - The international journal for computation and mathematics in electrical and electronic engineering*, vol. 27, no. 6, pp. 1451–1462, Jan. 2008.

[74] K. Yamazaki and H. Takeuchi, “Impact of mechanical stress on characteristics of interior permanent magnet synchronous motors,” in *2015 IEEE Energy Conversion Congress and Exposition (ECCE)*, pp. 4391–4396, Sep. 2015.

[75] F. Martin, U. Aydin, R. Sundaria, P. Rasilo, A. Belahcen, and A. Arkkio, “Effect of Punching the Electrical Sheets on Optimal Design of a Permanent Magnet Synchronous Motor,” *IEEE Transactions on Magnetics*, vol. 54, no. 3, pp. 1–4, Mar. 2018.

[76] R. Sundaria *et al*, “Effect of Laser Cutting on Core Losses in Electrical Machines Measurements and Modeling,” *IEEE Transactions on Industrial Electronics*, vol. 67, no. 9, pp. 7354–7363, Sep. 2020.

[77] B. Astie, J. Degauque, J. Porteseil, and R. Vergne, “Influence of the dislocation structures on the magnetic and magnetomechanical properties of high-purity iron,” IEEE Transactions on Magnetics, vol. 17, no. 6, pp. 2929–2931, Nov. 1981.

[78] J. Šternberk, E. Kratochvílová, J. Hřebík, and A. Gemperle, “Coercivity and Microstructure of Low-Alloy Steel,” *physica status solidi (a)*, vol. 79, no. 2, pp. 523–529, 1983.

[79] J. Šternberk, E. Kratochvílová, A. Gemperle, V. Faja, and V. Walder, “Dependence of characteristics of hysteresis loops on dislocation densities for low-alloy Cr-Mo steel,” *Czech J Phys*, vol. 35, no. 11, pp. 1259–1266, Nov. 1985.

[80] A. H. Qureshi and L. N. Chaudhary, “Influence of Plastic Deformation on Coercive Field and Initial Susceptibility of Fe-3.25% Si Alloys,” *Journal of Applied Physics*, vol. 41, no. 3, pp. 1042–1043, Mar. 1970.

[81] M. J. Sablik, “Modeling the effect of grain size and dislocation density on hysteretic magnetic properties in steels,” Journal of Applied Physics, vol. 89, no. 10, pp. 5610–5613, May 2001.

[82] M. J. Sablik, S. Rios, F. J. G. Landgraf, T. Yonamine, and M. F. de Campos, “Modeling of sharp change in magnetic hysteresis behavior of electrical steel at small plastic deformation,” *Journal of Applied Physics*, vol. 97, no. 10, p. 10E518, May 2005.

[83] E. Kokornaczyk and M. W. Gutowski, "Anhysteretic Functions for the Jiles–Atherton Model," in IEEE Transactions on Magnetics, vol. 51, no. 2, pp. 1-5, Feb. 2015, Art no. 7300305.

[84] S. Steentjes, M. Petrun, D. Dolinar and K. Hameyer, "Effect of Parameter Identification Procedure of the Static Hysteresis Model on Dynamic Hysteresis Loop Shapes," in IEEE Transactions on Magnetics, vol. 52, no. 5, pp. 1-4, May 2016, Art no. 7300804.

[85] S. Steentjes, M. Petrun, G. Glehn, D. Dolinar, and K. Hameyer, “Suitability of the double Langevin function for description of anhysteretic magnetization curves in NO and GO electrical steel grades,” *AIP Advances*, vol. 7, no. 5, p. 056013, May 2017.

[86] Z. Włodarski, “Analytical description of magnetization curves,” *Physica B: Condensed Matter*, vol. 373, no. 2, pp. 323–327, Mar. 2006.

[87] T. Yamasaki, S. Yamamoto, and M. Hirao, “Effect of applied stresses on magnetostriction of low carbon steel,” *NDT & E International*, vol. 29, no. 5, pp. 263–268, Oct. 1996.

[88] M. J. Sablik, H. Kwun, G. L. Burkhardt, and D. C. Jiles, “Model for the effect of tensile and compressive stress on ferromagnetic hysteresis,” *Journal of Applied Physics*, vol. 61, no. 8, pp. 3799–3801, Apr. 1987.

[89] M. J. Sablik and D. C. Jiles, “Coupled magnetoelastic theory of magnetic and magnetostrictive hysteresis,” IEEE Transactions on Magnetics, vol. 29, no. 4, pp. 2113–2123, Jul. 1993.

[90] M. J. Sablik, “A model for asymmetry in magnetic property behavior under tensile and compressive stress in steel,” IEEE Transactions on Magnetics, vol. 33, no. 5, pp. 3958–3960, Sep. 1997.

[91] D. Singh, F. Martin, P. Rasilo, and A. Belachen, “Magnetomechanical Model for Hysteresis in Electrical Steel Sheet,” *IEEE Trans. Magn.*, vol. 52, no. 11, pp. 1–9, Nov. 2016.

[92] L. Daniel and O. Hubert, “An equivalent stress for the influence of multiaxial stress on the magnetic behavior,” *Journal of Applied Physics*, vol. 105, no. 7, p. 07A313, Apr. 2009.
[93] K. Kashiwaya, “Fundamentals of Nondestructive Measurement of Biaxial Stress in Steel Utilizing Magnetoelastic Effect under Low Magnetic Field,” *Jpn. J. Appl. Phys.*, vol. 30, no. Part 1, No. 11A, pp. 2932–2942, Nov. 1991.
[94] C. S. Schneider and J. M. Richardson, “Biaxial magnetoelasticity in steels,” *Journal of Applied Physics*, vol. 53, no. 11, pp. 8136–8138, Nov. 1982.
[95] M. J. Sablik *et al.*, “Micromagnetic model for biaxial stress effects on magnetic properties,” *Journal of Magnetism and Magnetic Materials*, vol. 132, no. 1–3, pp. 131–148, Apr. 1994
[96] L. Daniel and O. Hubert, “Equivalent Stress Criteria for the Effect of Stress on Magnetic Behavior,” *IEEE Transactions on Magnetics*, vol. 46, no. 8, pp. 3089–3092, Aug. 2010.
[97] O. Hubert and L. Daniel, “Energetical and multiscale approaches for the definition of an equivalent stress for magneto-elastic couplings,” *Journal of Magnetism and Magnetic Materials*, vol. 323, no. 13, pp. 1766–1781, Jul. 2011.
[98] Olivier Hubert, Said Lazreg. “Two phase modeling of the influence of plastic strain on the magnetic and magnetostrictive behaviors of ferromagnetic materials”. *Journal of Magnetism and Magnetic Materials*, Elsevier, vol n° 424, pp.421 – 442, 2016.
[99] Z. D. Wang, B. Deng, and K. Yao, “Physical model of plastic deformation on magnetization in ferromagnetic materials,” *Journal of Applied Physics*, vol. 109, no. 8, p. 083928, Apr. 2011.
[100] J. Li, M. Xu, J. Leng, and M. Xu, “Modeling plastic deformation effect on magnetization in ferromagnetic materials,” *J. Appl. Phys.*, p. 5, 2012.
[101] Henneron, T, “Contribution à la prise en compte des Grandeurs Globales dansles Problèmes d’Electromagnétisme résolus avec la Méthode des Eléments Finis’’ , PhD thesis, Université Lille 1, 2004, France.
[102] G. Dhatt et G. Touzot, “Une présentation de la méthode des éléments finis”. *Presses Université* Laval, 1981.
[103] M. V. K. Chari et P. Silvester, “Analysis of Turboalternator Magnetic Fields by Finite Elements”, *IEEE Trans. Power Appar. Syst.*, vol. PAS-90, no2, p. 454-464, March 1971.
[104] Bastos, J. and Sadowski, N. “Electromagnetic modeling by finite elements methods”, Marcel Dekker, 2003.
[105] Johnson C. “Numerical solution of partial differential equations by the finite element method”, Cambridge University Press, 1987.
[106] Girault, V. and Raviart, “Finite Element Methods for Navier-Stokes Equations”: Theory and Algorithms. Springer-Verlag. 1986.
[107] A. Bossavit, «Whitney forms: a class of finite elements for three-dimensional computations in electromagnetism», IEE Proc. -Phys. Sci. Meas. Instrum. Manag. Educ. -Rev., vol. 135, no8, p. 493-500, nov. 1988.
[108] Whitney, H.” Geometric Integration Theory”. Princeton University Press, 1957.

[109] Y. Le Menach.”Contribution à la modélisation numérique tridimensionnelledes systèmes électrotechniques : Prise en compte des inducteurs”. Phd thesis, Université des sciences et technologies de Lille, 1999, France.
[110] C. A. J. Fletcher,’’Computational Galerkin methods’’, Springer, 1984
[111] P. Šolin, K. Segeth, and I. Doležel, “Higher-order finite element methods”. Boca Raton, FL: Chapman & Hall/CRC, 2004.
[112] Kuhn W, Grün F “Beziehungen zwischen elastischen Konstanten und Dehnungsdoppelbrechung hochelastischer Stoffe” Kolloid-Zeitschrift,1942
[113] Itskov M, Ehret A E, Dargazany R “A full-network rubber elasticity model based on analytical integration”, Math Mech Solids 15(6):655–671, 2010.
[114] Itskov M, Dargazany R, Hörnes K, “Taylor expansion of the inverse function with application to the Langevin function”, Math Mech Solids 17(7),2012.
[115] E. Darabi and M. Itskov, “A simple and accurate approximation of the inverse Langevin function,” *Rheol Acta*, vol. 54, no. 5, pp. 455–459, May 2015.
[116] A. Ben Ismail, “Modélisation de la découpe des tôles ferromagnétiques : corrélation entre l’état mécanique et les propriétés magnétiques,” Phd thesis, University of Compiègne, 2007. France.
[117] S. Fayolle, “Modélisation numérique de la mise en forme et de la tenue mécanique des assemblages par déformation plastique : application au rivetage auto-poinçonneur,” Phd thesis, École Nationale Supérieure des Mines de Paris, 2008. France.
[118] Baaijens.F.P.T. Brokken.D., Brekelmans.W.A.M. “Predicting the shape of blanked products: a finite element approach”. *Journal of Materials Processing Technology*,103(1) :51 56, 2000.
[119] Wu.W.t. Altan.T. Taupin.E., Breitling.J. “Material fracture and burr formation in blanking results of fem simulations and comparison with experiments”. *Journal of Materials Processing Technology*, 59(1-2) :68–78, 1996.
[120] E. Falconnet, J. Chambert, H. Makich, and G. Monteil, “Prediction of abrasive punch wear in copper alloy thin sheet blanking,” *Wear*, vol. 338–339, pp. 144–154, Sep. 2015.
[121] H. Marouani, A. B. Ismail, E. Hug, and M. Rachik, “Rate-dependent constitutive model for sheet metal blanking investigation,” *Materials Science and Engineering: A*, vol. 487, no. 1–2, pp. 162–170, Jul. 2008.
[122] Z. Tekiner, M. Nalbant, and H. Gürün, “An experimental study for the effect of different clearances on burr, smooth-sheared and blanking force on aluminum sheet metal,” *Materials & Design*, vol. 27, no. 10, pp. 1134–1138, Jan. 2006.
[123] Guerin.F. Hambli.R. Application of a neural network for optimum clearance prediction in sheet metal blanking processes. Finite Elements in Analysis and Design, 39(11) :1039–1052, 2003.
[124] J. A. Soares, M. L. Gipiela, S. F. Lajarin, and P. V. P. Marcondes, “Study of the punch–die clearance influence on the sheared edge quality of thick sheets,” *Int J Adv Manuf Technol*, vol. 65, no. 1, pp. 451–457, Mar. 2013.
[125] *Code_carmel* 3D FEA software “https://code-carmel.univ-lille.fr/”.